UNIVERSITA' DEGLI STUDI DI: TORINO

DIPARTIMENTO DI: FISICA GENERALE

DOTTORATO DI RICERCA IN:
SCIENZA E ALTA TECNOLOGIA - Indirizzo Fisica e Astrofisica

CICLO: XXII in Co-tutela con il Joint Institute for Nuclear Research di Dubna (Russia)

TITOLO DELLA TESI: Analysis of the charged pion polarizability measurement method at COMPASS experiment

TESI PRESENTATA DA: Guskov Alexey

TUTORS: Prof. Alexander Olshevskiy
Prof. Ferruccio Balestra

COORDINATORE DEL DOTTORATO: Prof. Guido Boffetta

ANNI ACCADEMICI: CICLO: XXII in Co-tutela con il Joint Institute for Nuclear Research di Dubna (Russia)

SETTORE SCIENTIFICO-DISCIPLINARE DI AFFERENZA*: FIS01

Università degli Studi di Torino
Scuola di Dottorato in Scienza ed Alta Tecnologia

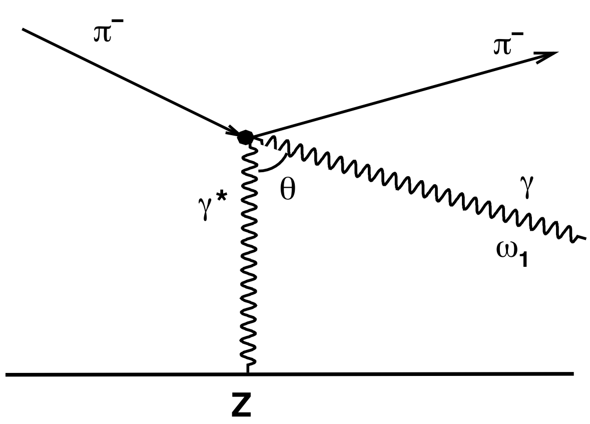

Analysis of the charged pion polarizability measurement method at COMPASS experiment

Alexey Guskov

Università degli Studi di Torino
Scuola di Dottorato in Scienza ed Alta Tecnologia

Indirizzo di Fisica ed Astrofisica

Analysis of the charged pion polarizability measurement method at COMPASS experiment

Alexey Guskov

Tutor: Prof. Alexander Olshevskiy
Prof. Ferruccio Balestra F. Balestra

Abstract

In fisica classica la polarizzabilità di un mezzo o di un sistema composito è quella ben nota caratteristica che lega la risposta del sistema alla presenza di un campo elettromagnetico esterno. Nel caso di un dipolo, la polarizzabilità elettrica α è la costante di propozionalità fra il campo elettrico ed il momento di dipolo elettrico, mentre β è connessa al campo magnetico ed al momento di dipolo magnetico.

Questo concetto puo' essere esteso anche al caso di particelle composite, quali protoni, pioni, kaoni ed altre. Nel caso del pione, nella diffusione Compton-like $\pi\gamma$, le polarizzabilità elettrica (α_π) e magnetica (β_π) caratterizzzano la risposta delle sottostrutture a quark alla presenza di un campo elettromagnetico esterno. Questi parametri sono fondamentali per ogni teoria che intenda descrivere la struttura del pione. Differenti modelli teorici predicono che la quantità $\alpha_\pi + \beta_\pi$ assuma valori prossimi a zero mentre i valori $\alpha_\pi - \beta_\pi$ siano compresi nell'intervallo $(6 - 14) \times 10^{-4}\ fm^3$.

Per misurare tali quantità sono già stati fatti diversi tentativi usando approcci differenti. I risultati ottenuti sono affetti da rilevanti incertezze sperimentali e non possono essere utilizati per verifiche, discriminanti tra le varie previsioni teoriche. A questo scopo sono necessarie nuove e più precise misure.

Il presente lavoro evidenzia le prospettive della misura della polarizzabilità del pione mediante l' esperimento COMPASS, attraverso lo studio della reazione di diffusione radiativa (detta reazione di Primakoff) $\pi^- + (A, Z) \rightarrow \pi^- + (A, Z) + \gamma$.

La potenzialità dell' apparato COMPASS per lo studio della reazione Primakoff è stata dimostrata dall' analisi dei dati raccolti nel 2004 durante il run pilota con fasci di pioni e muoni su bersagli di piombo, rame e carbonio.

I punti principali del presente lavoro sono: lo sviluppo e l' ottimizzazione dei criteri di selezione al fine di ottenere un campione puro di eventi Primakoff; lo studio dei differenti processi di fondo; lo sviluppo delle procedure per la sua soppressione; lo studio dell' accettanza dell' apparato COMPASS per la rivelazione di eventi Primakoff (mediante l'uso di simulazioni Monte Carlo); la stima delle possibili incertezze sia statistiche sia sistematiche legate alla misura delle polarizzabilità; le proposte di modifiche sia alla configurazione dell' apparato sia alla strategia della presa dati, in vista delle prossime misure a COMPASS.

La descrizione del lavoro di tesi consiste di 7 capitoli.

L' introduzione riporta una breve descrizione della problematica, presenta gli scopi del presente lavoro e le principali linee di attività.

Nel capitolo 2 sono riportate le previsioni di differenti modeli teorici quali: teoria chirale perturbativa, modello di Nambu-Jona-Lasinio, relazioni di dispersione, regole di somma QCD e modello di confinamento dei quark.

I risultati di precedenti misure sperimentali sulla polarizzabilità del pione sono discusse nel capitolo 3. Particolare attenzione è rivolta alle misure della reazione di Primakoff fatte a Serpukov.

Il capitolo 4 presenta l' esperimento COMPASS. Vengono discussi: il programma scientifico dell' esperimento, la disposizione sperimentale, le prestazioni dei rivelatori, gli strumenti di analisi dei dati e di simulazione Monte Carlo.

Nel capitolo 5 vengono discussi i risultati della presa-dati adronica pilota del 2004 e vengono presentati: le procedure di selezione degli eventi Primakoff, lo studio dei processi di fondo, le procedure di sottrazione del fondo e lo studio della reazione di Primakoff, utilizzando diversi bersagli esposti a fasci di pioni e di muoni.

Nel capitolo 6 vengono presentate raccomandazioni per le future misure di precisione delle polarizzabilità del pione mediante COMPASS. Esse sono state approvate dalla Collaborazione COMPASS per la presa dati del 2009. Esse riguardano miglioramenti del sistema di trigger, del sistema di bersaglio, del sistema di rivelazione dei muoni e della linea di fascio. Vengono inoltre presentate le stime dei possibili errori sistematici e statistici. In questo capitolo viene anche presentata la possibilità di eseguire per la prima volta l' osservazione della diffusione Primakoff di kaoni nonchè di misurare la polarizzabilità del kaone.

I risultati del presente lavoro sono riassunti nel capitolo conclusivo. In particolare è stato dimostrato che il numero di eventi Primakoff selezionati nel run adronico del 2004 e le distribuzioni fondamentali di tali eventi sono in accordo con le previsioni teoriche applicate all' apparato COMPASS. In secondo luogo è stato possibile progettare un' ottimizzazione dell' apparato COMPASS che permetterà di eseguire, nelle future prese-dati Primakoff, una misura della polarizzabilità α_π con un errore statistico di $0.35 \times 10^{-4}\ fm^3$ e un errore sistematico di $0.2 \times 10^{-4}\ fm^3$, valori inferiori a quelli ottenuti nei precedenti esperimenti.

Contents

Chapter 1

Introduction

In classical physics the polarizability of a medium or a composite system is the well known characteristic related the response of the system to the presence of an external electromagnetic field. If one consider a dipole, the electric polarizability α is the proportionality constant between the electric field and the electric dipole moment, while β is related to the magnetic field and the magnetic dipole moment.

This concept was extended to the case of composite particles, like protons, pions, kaons and others. In the case of pion the electric (α_π) and magnetic (β_π) polarizabilities characterize the response of the quark substructure to the presence of an external electromagnetic field in the $\pi\gamma$ Compton-like scattering. These parameters are fundamental ones for any theory describing the pion structure.

Significance of the problem. Different theoretical models predict that the value of $\alpha_\pi + \beta_\pi$ is close to zero while the values of $\alpha_\pi - \beta_\pi$ are significantly different and lie in a range $(6 - 14) \times 10^{-4}\ fm^3$.

Several attempts to measure these quantities were already done using different approaches. The obtained results are affected by large uncertainties and cannot be used for critical tests of theoretical predictions.

New more precise measurements are needed in order to make conclusions about validity of different theoretical models and test of their applicability ranges.

Goal of the work. The goal of this work is to study the possibility to measure pion polarizabilities at the COMPASS experiment at CERN via the reaction of radiative scattering (so called Primakoff reaction)

$$\pi^- + (A, Z) \rightarrow \pi^- + (A, Z) + \gamma. \tag{1.1}$$

The main points of the work are:

- development and optimization of selection criteria to obtain pure sample of Primakoff events;
- background processes study and development of background suppression procedure;
- estimation of the Primakoff cross section for different targets;
- study of the acceptance of the COMPASS setup for Primakoff events using Monte Carlo simulation;
- estimation of possible statistical and systematic uncertainties of polarizabilities measurement under assumption $\alpha_\pi + \beta_\pi = 0$;
- proposal for changes in setup configuration and in strategy of data taking for future measurements at COMPASS.

Scientific novelty:

- the first COMPASS results for observation of the Primakoff reaction are presented;
- estimation of possibility to perform precise measurement of pion polarizabilities at COMPASS is done basing on the results of pilot hadron run 2004;
- modifications of the setup and strategy of data taking are proposed in order to optimize them for future measurements of pion polarizabilities.

Practical importance. The obtained results demonstrate unique perspective to perform the most precise measurements of α_π and β_π in COMPASS experiment (possible accuracy is four times better than in the best previous measurement). They are already used for preparation for new data taking. These results can be also used for planning of new future polarizability measurements at different accelerators and different particles like pion, kaon etc.

The following results were obtained by the author:

- the algorithm of Primakoff events selection taking into account the specific COMPASS setup was developed and tested;
- the suppression algorithm against background processes having the same signature in the COMPASS setup as the Primakoff scattering was developed and tested ;
- the results of Monte Carlo simulation of Primakoff events reconstruction in the COMPASS setup were obtained;
- estimation of the Primakoff cross section for Pb, Cu and C targets was done;
- estimation of statistical and systematic errors of pion polarizabilities measurement under assumption $\alpha_\pi + \beta_\pi = 0$ was done;
- optimization of the setup and strategy of data taking proposed for future measurements was performed.

Approbation of the work. The results of the work have been reported by the author on behalf of the COMPASS collaboration at the following international conferences:

1. Advanced Study Institute on Symmetries and Spin (SPIN-Praha-2005), Prague, Czech Republic, 2005,
2. XXXIII International Conference on High Energy Physics (ICHEP'06), Moscow, Russia, 2006,
3. The Europhysics Conference HEP 2007, Manchester, England, 2007,
4. Hadron Structure (HS 07), Modra-Harmonia, Slovakia, 2007,
5. Hadron Structure (HS 09), Tatranska Štrba, Slovakia, 2009.

The results were published in the following papers:

1. A. Guskov [COMPASS Collaboration], Measurement of the pion poalrizabilities at COMPASS, *In *Moscow 2006, ICHEP* 655-658*;

2. P. Abbon , ... A. Guskov, ... et al., The Compass Experiment at CERN. NIM, **A577**, 455-518 (2007);
3. A. Guskov [COMPASS Collaboration], Pion polarizabilities measurement at COMPASS, Fizika, **B17**, 313 (2008);
4. A. Guskov, Pion polarizabilities measurement at COMPASS, J. Phys. Conf. Ser., **110**, 022016 (2008);
5. A. Guskov [COMPASS Collaboration], Plans for a measurement of pion polarizabilities at COMPASS, accepted for publication in Nucl. Phys. B;
6. Yu. M. Bystritskiy, A.V. Guskov, V.N. Pervushin, M.K. Volkov, Pion Polarizability in the NJL model and Possibilities of its Experimental Studies in Coulomb Nuclear Scattering, Phys. Rev. **D80**, 114001 (2009);
7. A. Guskov, The Primakoff reaction study for pion polarizability measurement at COMPASS, Phys. Part. Nucl. Lett., **3** 59 (2010).

Structure of thesis. The presented work consists of 7 chapters.

Introduction gives short overview of the problem, presents the goal of this work and tell about main directions of activity.

The predictions of different theoretical models such as chiral perturbation theory, Nambu-Jona-Lasinio model, dispersive relations, QCD sum rules and quark confinement model are described in Chapter 2 of this paper.

Previous experimental measurements of pion polarizabilities are discussed in Chapter 3. Particular attention is given to measurements via the Primakoff reaction done at Serpukhov.

Chapter 4 introduces the COMPASS experiment. The physical program of the experiment, the detector layout and performance, the data analysis and Monte Carlo simulation tools are discussed.

The COMPASS pilot hadron run 2004 is discussed in Chapter 5. The procedure of Primakoff events selection, background processes study, the background subtraction procedure, Primakoff reaction study with different targets and with pion and muon beam are presented.

Recommendations for coming measurement of pion polarizabilities at COMPASS are presented in Chapter 6. Possible improvements of the setup and the strategy of data taking are discussed. Estimation of possible statistical and systematic errors is presented. The possibility to perform the first observation of kaon Primakoff scattering and to measure kaon polarizabilities is also studied.

The results of the work are summarized in Conclusion.

Chapter 2

Pion polarizabilities in theoretical models

The concept of polarizability, well known in classical physics, was applied for the first time to hadrons in [1]-[3] (see also [4]). The translation of this concept into quantum physics involves Compton scattering on the corresponding particle. For an electrically charged system scattering at threshold is determined by the charge of the system. This is the Thompson limit. The electrical and magnetic polarizabilities give the corrections to Thompson scattering - corrections to the next order in the energy of the photons.

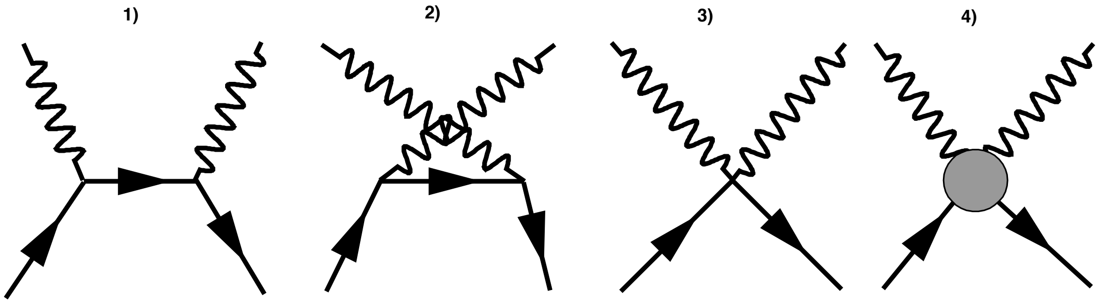

Figure 2.1: Diagrams 1-3 contributes to the Compton amplitude. Diagram 4 schematically represents polarization effects.

The kinematics of the Compton the scattering can be described by the Mandelstam invariant variables:

$$s = (p_1 + q_1)^2,\ t = (p_1 - p_2)^2,\ u = (p_1 - q_2)^2, \tag{2.1}$$

where p_1, p_2 and q_1, q_2 are the pion and photon 4-momenta. As far as it is difficult to study the Compton scattering on a pion directly, other processes with the Compton vertex are interesting. Examples of such processes are (see Figs. 2.2, 2.3):

- the pion scattering on the nuclear target with hard photon emission so called Primakoff scattering (t-channel)

$$\pi + Z \rightarrow \pi + Z + \gamma, \tag{2.2}$$

- the pion photoproduction (t-channel)

$$\gamma + p \rightarrow \gamma + \pi^+ + n, \tag{2.3}$$

- $\pi^+\pi^-$ pair production in e^+e^- collisions (s-channel)

$$e^+ + e^- \rightarrow \pi^+ + \pi^-. \tag{2.4}$$

The amplitude for Compton scattering on a pion can be expanded in powers of the energies of the photons near threshold:

$$T(\pi^-\gamma \rightarrow \pi^-\gamma) = (-\frac{\alpha}{m_\pi} + \alpha_\pi\omega_1\omega_2) \cdot \hat{\epsilon}_1\hat{\epsilon}_2 + \beta_\pi\omega_1\omega_2(\hat{\epsilon}_1 \times \hat{q}_1) \cdot (\hat{\epsilon}_2 \times \hat{q}_2) + \dots\,, \tag{2.5}$$

where α is the fine structure constant, $q_i = \omega_i(1, \hat{q}_i)$ for i=1, 2 and $\hat{\epsilon}_i$ is the polarization vector of the photon with momentum q_i. α_π and β_π are the electrical and magnetic polarizabilities of a pion. They characterize the response of pion as composite hadron system to two-photon interactions at low energies and are analogous to electromagnetic radius and magnetic moment which characterize the response of pion to its single-photon interaction at low energies.

In nonrelativistic approximation the corresponding part of hamiltonian looks like for the interaction of a medium with external electromagnetic field:

$$\mathbf{H} = -\frac{1}{2}(\alpha_\pi E^2 + \beta_\pi H^2). \tag{2.6}$$

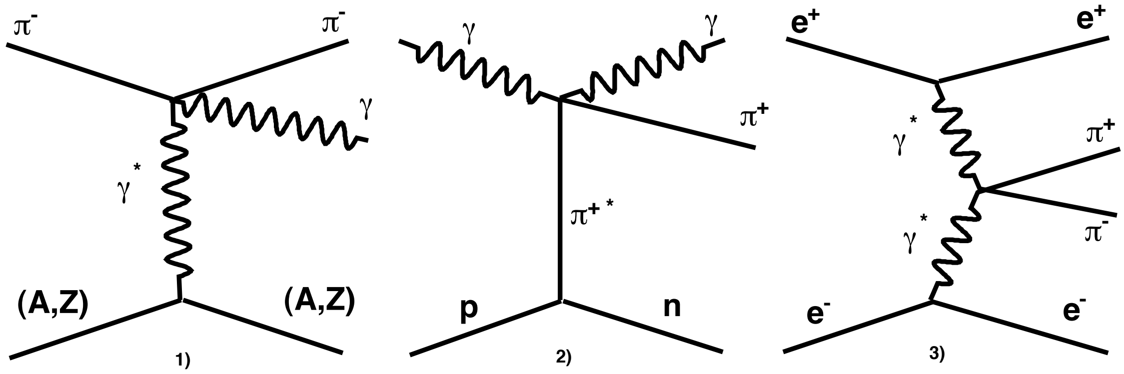

Figure 2.2: Processes with Compton vertex: 1) Primakoff scattering, 2) pion photoproduction, 3) $\pi^+\pi^-$ pair production.

2.1 Chiral perturbation theory (χPT)

The chiral expansion gives the next representation for pion polarizabilities:

$$\begin{array}{rl} & \qquad\quad tree \;\; 1-loop \quad 2-loops \quad 3-loops \\ \alpha_\pi \pm \beta_\pi = \dfrac{\alpha}{m_\pi^3} \times & (0 \quad + \quad A_\pm x \quad + \quad B_\pm x^2 \quad + \quad O(m_\pi^4)), \end{array} \tag{2.7}$$

$$x = \frac{m_\pi^2}{16\pi^2 F_\pi^2}, \tag{2.8}$$

where $F_\pi = 92.4$ MeV is the pion decay constant. The first line indicates the number of loops that are needed to calculate the coefficients $A_\pm, B_\pm$. To arrive at the expansion Eq. (2.7) the Compton amplitude in the framework of χPT was considered:

$$T_{\chi PT} = T_2 + T_4 + T_6 + ..., \tag{2.9}$$

where T_n is of the order $p^{(n-2)}$. This expansion is most conveniently performed in the framework of an effective lagrangian. The effective lagrangian can be expressed in terms of the pion field U , the quark mass matrix χ and the external vector field v_μ:

$$L_{eff} = L_2(U, \chi, v_{mu}) + \hbar L_4(U, \chi, v_{mu}) + \hbar^2 L_6(U, \chi, v_{mu}) + ..., \tag{2.10}$$

where L_n denotes a term of order p^n.

The leading order term in the polarizabilities is generated by one-loop

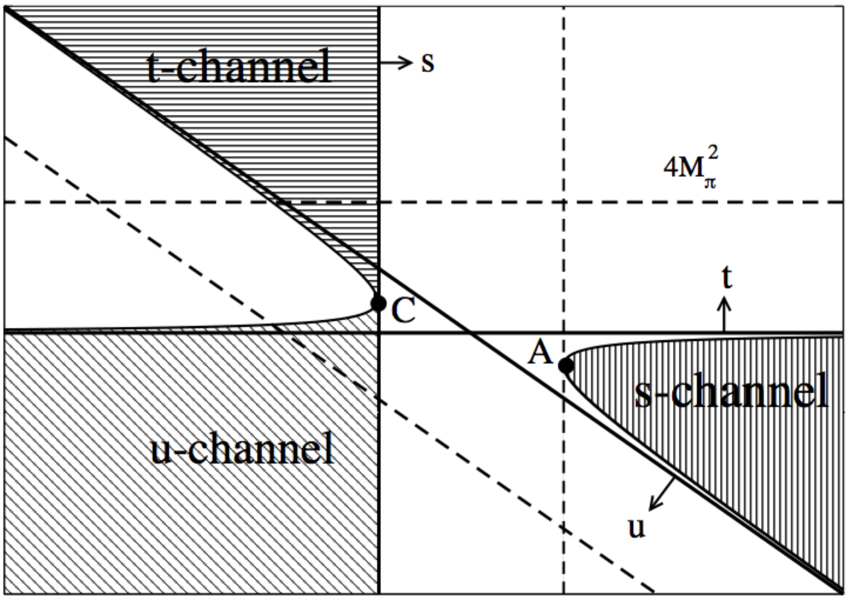

Figure 2.3: Mandelstam variables for different processes. C is the threshold of $\gamma\pi \to \gamma\pi$ process, A is the threshold of $\gamma\gamma \to \pi\pi$ process [5].

diagrams and the corresponding numerical values are ([12]-[14]):

$$\begin{aligned} \alpha_\pi + \beta_\pi &= 0, \\ \alpha_\pi - \beta_\pi &= (5.4 \pm 0.8) \times 10^{-4} fm^3. \end{aligned} \tag{2.11}$$

Taking into account the next-to-leading order term ([10],[11]) gives the result:

$$\begin{aligned} \alpha_\pi + \beta_\pi &= (0.16 \pm 0.1) \times 10^{-4} fm^3, \\ \alpha_\pi - \beta_\pi &= (5.72 \pm 0.4) \times 10^{-4} fm^3, \\ \alpha_\pi &= (2.93 \pm 0.5) \times 10^{-4} fm^3, \\ \beta_\pi &= (-2.77 \pm 0.5) \times 10^{-4} fm^3. \end{aligned} \tag{2.12}$$

2.2 Nambu-Jona-Lasinio model

The calculations of the pion polarizability α_π in the Nambu-Jona-Lasinio model were fulfilled in [15] (see also [16],[17]), where the quark loops and the meson loops were taken into account, under assumption $\alpha_\pi + \beta_\pi = 0$:

$$\alpha_\pi(t) = \frac{\alpha}{2\pi F_\pi^2 m_\pi}(\chi^{fermion}(t) + \chi^{pion}(t)), \tag{2.13}$$

where $\chi^{fermion}$ and χ^{pion} are the contributions of the fermion and pion loops. Assuming $m_u = m_d = 280\ MeV$ and $m_\sigma^2 = 4m_u^2 + m_\pi^2$, where m_u, m_d and m_σ are the masses of u-, d-quarks and σ-meson, NJL model predicts:

$$\alpha_\pi(t=0) = 4.9 \times 10^{-4} fm^3 \tag{2.14}$$

The model also predicts strong t-dependence of the polarizability. So, for $t = -4m_\pi^2$ the value of α_π decreases to $2.8 \times 10^{-4} fm^3$.

2.3 Quark confinement model

The QCM developed by Efimov et al. [26], [27] has also been employed to predict values for the pion polarizabilities. The basic characteristic of the model is a confinement ansatz that allows loop calculations to be made finite, avoiding the need for a regularization procedure.

Authors [27] consider the contribution to pion polarizabilities coming from pure loop terms and vector, axial vector and scalar resonances. The contribution given by the scalar resonances is dominating in this model. Obtained values for pion polarizabilities are:

$$\alpha_\pi = 3.64 \times 10^{-4} fm^3,$$
$$\beta_\pi = -3.41 \times 10^{-4} fm^3.$$

2.4 Dispersive relations

Pion polarizabilities can be estimated basing on the dispersion relations for the helicity amplitudes [18]-[20] of the process $\gamma\gamma \to \pi^+\pi^-$. The dispersion sum rules for the difference and sum of the polarizabilities are:

$$\begin{aligned}\alpha_\pi - \beta_\pi = \frac{1}{2\pi^2 m_\pi}\{\int_{4m_\pi^2}^{\infty} \frac{ImM_{++}(t', u = m_\pi^2)dt'}{t'} +\\ + \int_{4m_\pi^2}^{\infty} \frac{ImM_{++}(s', u = m_\pi^2)ds'}{s' - m_\pi^2}\},\end{aligned} \tag{2.15}$$

$$\begin{aligned}\alpha_\pi + \beta_\pi = \frac{m_\pi}{\pi^2}\int_{4m_\pi^2}^{\infty} \frac{ImM_{+-}(s', t = 0)ds'}{s' - m_\pi^2} =\\ \frac{1}{2\pi^2}\int_{\frac{3}{2}m_\pi}^{\infty} \frac{\sigma_T(E_\gamma)dE_\gamma}{E_\gamma},\end{aligned} \tag{2.16}$$

where σ_T is the total cross section of the $\pi\gamma$ interaction and E_γ is the photon energy in the laboratory system.

The dispersion sum rules for the charged pions are saturated by the contributions of the $\rho(770), b_1(1235), a_1(1270)$ and $a_2(1320)$ mesons in the s-channel and $\sigma, f_0(980), f_0^1(1370), f_2(1270)$ and $f_2^1(1525)$ in the t-channel. The obtained result for pion polarizabilities is:

$$\begin{aligned} \alpha_\pi + \beta_\pi &= (0.166 \pm 0.024) \times 10^{-4} fm^3, \\ \alpha_\pi - \beta_\pi &= (13.6 \pm 2.15) \times 10^{-4} fm^3. \end{aligned} \tag{2.17}$$

2.5 QCD sum rules

Current Algebra and PCAC (Partially Conserved Axial vector Current) relation demand that the polarizabilities of the charged pion be directly related to the axial (h_A) and vector (h_V) structure-dependent form factors of the radiative pion decay $\pi^+ \to e^+ + \nu_e + \gamma$ as [21],[22]

$$\alpha_\pi = \frac{\alpha}{8\pi^2 m_\pi F_\pi^2} \frac{h_A}{h_V}. \tag{2.18}$$

The calculation of the electric polarizability for the charged pion has been performed using QCD sum rules in [23] The authors take the current algebra sum rule of Das, Mathur and [24] Okubo:

$$\frac{\alpha}{8\pi^2 m_\pi F_\pi^2} \frac{h_A}{h_V} = \frac{\alpha}{3m_\pi} < r_\pi^2 > + \frac{\alpha}{2m_\pi F_\pi^2} \int_{4m_\pi^2}^{\infty} ds \frac{1}{s^2} [\rho^A(s) - \rho^V(s)], \tag{2.19}$$

where $\rho^V(s)$ and $\rho^A(s)$ are the spectral functions of vector and axial-vector mesons and $< r^2 >$ is the mean value of pion charge radius squared (for calculation the experimental value [25] $< r^2 >= (0.439 \pm 0.008)\ fm^2$ was taken.) For computation the integral of the vector and axial spectral functions QCD sum rule methods were used. The obtained value is

$$\alpha_\pi = (5.6 \pm 0.5) \times 10^{-4} fm^3. \tag{2.20}$$

More detailed review of pion polarizabilities concept in various theoretical models can be found in [6]-[9].

Table 2.1: Theoretical predictions for $(\alpha_\pi + \beta_\pi) and\ (\alpha_\pi - \beta_\pi)$

Model	Parameter	$[10^{-4} fm^3]$
χPT	$\alpha_\pi - \beta_\pi$	5.7 ± 1.0
	$\alpha_\pi + \beta_\pi$	0.16
NJL	$\alpha_\pi - \beta_\pi$	9.8
QCM	$\alpha_\pi - \beta_\pi$	7.05
	$\alpha_\pi + \beta_\pi$	0.23
QCD sum rules	$\alpha_\pi - \beta_\pi$	11.2 ± 1.0
Dispersion sum rules	$\alpha_\pi - \beta_\pi$	13.60 ± 2.15
	$\alpha_\pi + \beta_\pi$	0.166 ± 0.024

Chapter 3

Experimental data for pion polarizabilities

3.1 Pion polarizabilities measurement in previous experiments

All three processes mentioned in Chapter 2 (see Fig. 2.2) were used for determination of pion polarizabilities.

3.1.1 The pion scattering on the nuclear target with hard photon emission (SIGMA-AYAKS)

The idea to measure pion polarizabilities in a reaction 2.2 was proposed in [46]. The measurement was performed with the SIGMA-AYAKS spectrometer at Serpukhov with 40 GeV/c negative pion beam and a carbon target. The covered range of virtual photon energy in the pion at rest system is 100-600 MeV. Preliminary result

$$\alpha_\pi = (5 \pm 4) \times 10^{-4} fm^3 \tag{3.1}$$

was presented in [37]. It was the first experimental measurement of pion polarizability. In further analysis more precise results were obtained for α_π, measured under assumption $\alpha_\pi + \beta_\pi = 0$:

$$\alpha_\pi = -\beta_\pi = (6.8 \pm 1.4_{stat} \pm 1.2_{syst}) \times 10^{-4} fm^3 \tag{3.2}$$

and for independent measurement of the electric and magnetic polarizabilities:

$$\begin{aligned} \alpha_\pi + \beta_\pi &= (1.4 \pm 3.1_{stat} \pm 2.8_{syst}) \times 10^{-4} fm^3, \\ \beta_\pi &= (-7.1 \pm 2.8_{stat} \pm 1.8_{syst}) \times 10^{-4} fm^3. \end{aligned} \tag{3.3}$$

More detailed description of SIGMA-AYAKS experiment is given in Section 3.4.

3.1.2 $\gamma\gamma$ interaction in e^+e^- collisions (PLUTO, DM1, DM2, Mark II)

The first attempts to extract pion plarizabilities from the cross section of the process (2.4) have been done using the data of PLUTO [32], DM1 [33] and DM2 [34] experiments. The precision of these measurements was much lower than the precision of the values obtained by SIGMA-AYAKS collaboration:

$$\alpha_\pi = (19.1 \pm 4.8_{stat} \pm 5.7_{syst}) \times 10^{-4} fm^3 \ (PLUTO), \tag{3.4}$$

$$\alpha_\pi = (17.2 \pm 4.6) \times 10^{-4} fm^3 \ (DM1), \tag{3.5}$$

$$\alpha_\pi = (26.3 \pm 7.4) \times 10^{-4} fm^3 \ (DM2). \tag{3.6}$$

New high statistics measurement of this cross section was performed using 209 pb^{-1} of data taking with Mark II detector at the SLAC storage ring PEP at a center of mass energy of 29 GeV/c. The cross section was extracted over the range of invariant pion-pair masses $M_{\pi^+\pi^-}$ between 0.35 GeV and 1.6 GeV [35]. The data of the Mark II were fitted in [36]. The obtained result is

$$\alpha_\pi = (2.2 \pm 1.6_{stat+syst}) \times 10^{-4} fm^3. \tag{3.7}$$

At the moment it is the most precise measurement of pion polarizability.

There were attempts also to make combined fit of the data for $\gamma\gamma \to \pi^+\pi^-$ cross section collected in different experiments. Fit result based on the data of Mark II VENUS, ALEPH, TPC/2γ, CELLO and BELLE is [19]

$$\begin{aligned} \alpha_\pi + \beta_\pi &= (0.18^{+0.11}_{-0.02}) \times 10^{-4} fm^3, \\ \alpha_\pi - \beta_\pi &= (13.0^{+2.6}_{-1.9}) \times 10^{-4} fm^3. \end{aligned}$$

Fit result based on the data of Mark II and Crystal Ball is [41]

$$\alpha_\pi - \beta_\pi = (5.25 \pm 0.95) \times 10^{-4} fm^3. \tag{3.8}$$

3.1.3 Pion photoproduction (Lebedev, MAMI A2)

The cross section for the radiative photoproduction of π^+ on hydrogen in dependence on the momentum transfer has been measured at the 1.2 GeV electron synchrotron PACHRA in Lebedev institute [31]. Using extrapolation of the data to pion pole the differential cross section for the pion Compton scattering has been obtained and the electric polarizability of π^+ meson has been estimated under assumption $\alpha_\pi + \beta_\pi = 0$ to be

$$\alpha_\pi = (20 \pm 12) \times 10^{-4} fm^3. \tag{3.9}$$

New, more precise experiment on the radiative π^+-meson photoproduction from the proton ($\gamma + p \rightarrow \gamma + \pi^+ + n$) was carried out at the Mainz Microtron MAMI in the kinematic region 537 MeV $< E_\gamma <$ 817 MeV, $140^\circ \leq \theta^{cm}_{\gamma\gamma'} \leq 180^\circ$ [40]. The π^+-meson polarizabilities have been determined from a comparison of the data with the predictions of two different theoretical models, the first one being based on an effective pole model with pseudoscalar coupling while the second one is based on diagrams describing both resonant and nonresonant contributions. The validity of the models has been verified by comparing the predictions with the present experimental data in the kinematic region where the pion polarizability contribution is negligible ($s < 5m_\pi^2$) and where the difference between the predictions of the two models does not exceed 3%. In the region, where the pion polarizability contribution is substantial ($5 < s/m_\pi^2 < 15$, $-12 < t/m_\pi^2 < -2$), the difference $\alpha_\pi - \beta_\pi$ has been determined. It was found that

$$\alpha_\pi - \beta_\pi = (11.6 \pm 1.5_{stat} \pm 3.0_{syst} \pm 0.5_{mod}) \times 10^{-4} fm^3. \tag{3.10}$$

The experimental results mentioned above are joined in Tab. 3.1 and presented graphically in Fig. 3.1. More detailed review of performed and proposed experimental measurements can be found at [44], [45].

3.2 Primakoff reaction

The Primakoff reaction $\pi^- + (A, Z) \rightarrow \pi^- + (A, Z) + \gamma$ can be treated as Compton scattering of the pion off a virtual photon, provided by the nucleus,

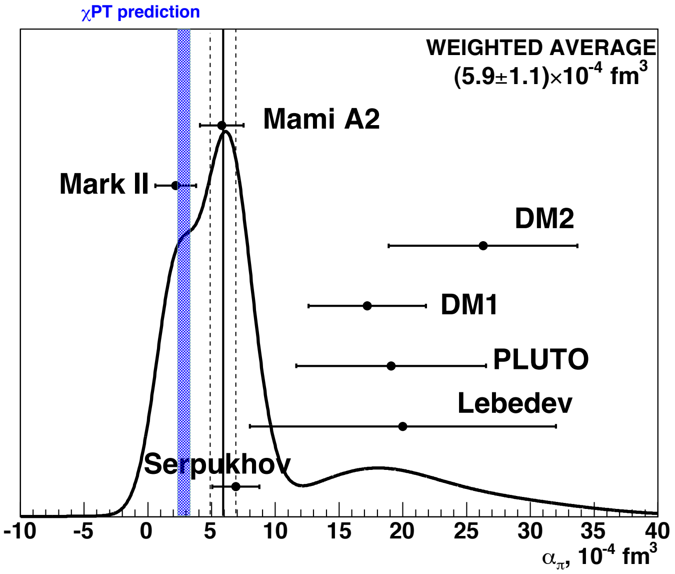

Figure 3.1: Experimental results for α_π under assumption $\alpha_\pi + \beta_\pi = 0$.

(see Fig. 3.2). Assuming that the mass of virtual photon is much smaller than the pion mass:

$$Q^2 \ll m_\pi^2, \tag{3.11}$$

one using the Weizsäcker-Williams approximation can relate the Primakoff cross section and the Compton cross section:

$$d\sigma_{Prim} = d\sigma_{Comp} n(\omega_1, q_1) d\omega_1 dq_1, \tag{3.12}$$

where ω_1, q_1 - energy and momentum of incoming photon in a anti-laboratory system and $n(\omega_1, q_1)$ is the equivalent photons density. The differential cross section is described by the formula:

$$\begin{aligned}\frac{d^3\sigma}{dQd\omega_1 d(cos\theta)} &= \frac{2\alpha^3 Z^2}{m_\pi^2 \omega_1} \times \frac{Q^2 - Q_{min}^2}{Q^4} |F_A(Q^2)|^2 \times \\ &\times \Big(F_{\pi\gamma}^{Pt} + \frac{m_\pi \omega_1^2}{\alpha} \cdot \frac{\alpha_\pi (1 + cos^2\,\theta) + 2\beta_\pi cos\;\theta}{(1 + \frac{\omega_1}{m_\pi}(1 - cos\;\theta))^3} \Big),\end{aligned} \tag{3.13}$$

where $Q_{min}^2 = (\frac{m_\pi \omega_1}{p_{beam}})^2$, θ is the angle between the real photon and the virtual photon directions , $F_A(Q^2)$ is the electromagnetic form factor of the nucleus ($F_A(Q^2) \approx 1$ for $Q \ll m_\pi$), α is the fine structure constant, $F_{\pi\gamma}^{Pt}$ [42] is the differential Compton cross section for the scattering of photons on a point-like

Table 3.1: Experimental values of $\alpha_\pi, \beta_\pi,\ (\alpha_\pi + \beta_\pi),\ (\alpha_\pi - \beta_\pi)$

Data	Reaction	Paramater	$[10^{-4} fm^3]$
Serpukhov ($\alpha_\pi + \beta_\pi = 0$)[38]	$\pi Z \rightarrow \pi Z \gamma$	α_π	6.8±1.4±1.2
Serpukhov ($\alpha_\pi + \beta_\pi \neq 0$)[39]		$\alpha_\pi + \beta_\pi$ β_π	1.4±3.1±2.8 $-7.1 \pm 2.8 \pm 1.8$
Lebedev [31]	$\gamma N \rightarrow \gamma N \pi$	α_π	20±12
Mami A2 [40]	$\gamma p \rightarrow \gamma \pi^+ n$	$\alpha_\pi - \beta_\pi$	11.6±1.5±3.0±0.5
PLUTO [32]	$\gamma\gamma \rightarrow \pi^+\pi^-$	α_π	19.1±4.8± 5.7
DM1 [33]	$\gamma\gamma \rightarrow \pi^+\pi^-$	α_π	17.2±4.6
DM2 [34]	$\gamma\gamma \rightarrow \pi^+\pi^-$	α_π	26.3±7.4
Mark II [36]	$\gamma\gamma \rightarrow \pi^+\pi^-$	α_π	2.2±1.6
Global fit: MARK II, VENUS, ALEPH, TPC/2γ, CELLO, BELLE (L. Fil'kov, V. Kashevarov)[19]	$\gamma\gamma \rightarrow \pi^+\pi^-$	$\alpha_\pi - \beta_\pi$ $\alpha_\pi + \beta_\pi$	$13.0^{+2.6}_{-1.9}$ $0.18^{+0.11}_{-0.02}$
Global fit: MARK II, Crystal Ball (A. Kaloshin, V. Serebryakov) [41]	$\gamma\gamma \rightarrow \pi^+\pi^-$	$\alpha_\pi - \beta_\pi$	5.25 ± 0.95

spin-0 particle. The cross section depends on $\alpha_\pi+\beta_\pi$ at forward angles and on $\alpha_\pi-\beta_\pi$ at backward angles. Polarization effects for $\alpha_\pi = -\beta_\pi = 3\times10^{-4}\ fm^3$ for different values of $cos\ \theta$ and Mandelstam variable s are shown in Fig. 3.3.

So, via measurements of the cross section (Eq. (3.13)) vs. the photon energy and (or) the scattering angle one can extract both α_π and β_π.

The variables ω_1, ω_2 (the energy of scattered photon in anti-laboratory system) and θ are related by expression :

$$\frac{1}{\omega_2} - \frac{1}{\omega_1} = \frac{1 - cos\ \theta}{m_\pi}. \tag{3.14}$$

All theoretical models, mentioned above, predict that

$$\alpha_\pi + \beta_\pi \ll \alpha_\pi - \beta_\pi \tag{3.15}$$

and performed experiments (see Table 3.1) confirm it. So, for the beginning, one can perform the measurement of the pion polarizabilities under assumption

$$\alpha_\pi + \beta_\pi = 0. \tag{3.16}$$

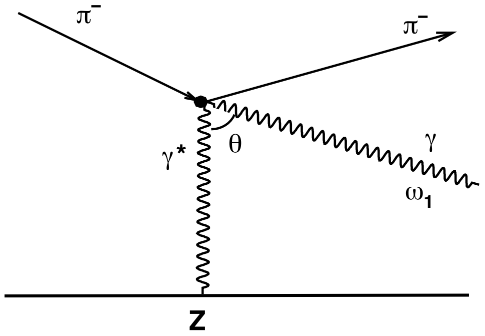

Figure 3.2: The diagram of the Compton scattering in inverse kinematics (Primakoff scattering).

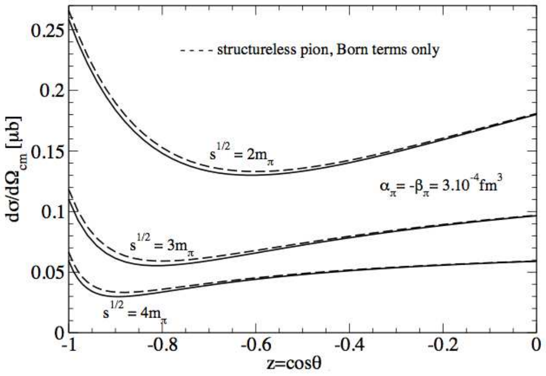

Figure 3.3: Primakoff cross section for point-like pion (solid line) and for $\alpha_\pi = -\beta_\pi = 3 \times 10^{-4}\ fm^3$ (dotted line) for different values of $cos\ \theta$ and s [43].

In this case to extract pion polarizability α_π it's enough to compare the measured differential cross section $d\sigma/d\omega_2$ or $d\sigma/d(cos\ \theta)$ and theoretically predicted for the point-like (unstructured) pion. Due to the small scattering angles in the laboratory system (typical angles are $\sim m_\pi/E_0$, where E_0 is the energy of incoming pion in laboratory system), the relative precision of angular measurements is much lower than the relative precision of photon energy measurement. Therefore the study of energy spectrum of scattered photons is preferable and the laboratory system is more convenient for such kind of studies. For designation of such kinematic variables in the laboratory system as energy of scattered photon, scattered pion energy and momentum, pion and photon scattering angles the variables E_γ, E_π, P_π, θ_π, θ_γ will be used. Relationship between kinematic variables in anti-laboratory and laboratory systems for energy of incoming pion 190 GeV is shown in Fig. 3.4.

In the laboratory system the cross section $d\sigma/dE_\gamma$ can be expressed by equation containing two terms: a term corresponding to point-like pion and polarization term

$$\frac{d\sigma}{dE_\gamma} = \left(\frac{d\sigma}{dE_\gamma}\right)_{point-like} + \left(\frac{d\sigma}{dE_\gamma}\right)_{pol.}, \tag{3.17}$$

where

$$\left(\frac{d\sigma}{dE_\gamma}\right)_{point-like} = \frac{4Z^2\alpha^3}{m_\pi^2} \times \frac{E_\pi}{E_0 E_\gamma} \times \left(\frac{2}{3} ln \frac{Q^2_{max}}{Q^2_{min}} - \frac{19}{9} + 4\sqrt{\frac{Q^2_{min}}{Q^2_{max}}}\right) \tag{3.18}$$

and

$$\left(\frac{d\sigma}{dE_\gamma}\right)_{pol} = -\frac{4Z^2\alpha^3}{m_\pi^2} \times \frac{E_\gamma}{E_0^2} \times \frac{\alpha_\pi m_\pi^3}{\alpha} \left(ln\frac{Q^2_{max}}{Q^2_{min}} - 3 + 4\sqrt{\frac{Q^2_{min}}{Q^2_{max}}} \right). \quad (3.19)$$

The value of Q^2_{min} in the laboratory system is

$$Q^2_{min} = (\frac{E_\gamma m_\pi^2}{2E_0(E_0 - E_\gamma)})^2 \quad (3.20)$$

and the value of Q^2_{max} can be chosen basing on the conditions of particular experiment.

Using the ω variable, which is the relative energy of emitted photon in lab. system:

$$\omega = E_\gamma / E_0, \quad (3.21)$$

the ratio R of the differential cross section $d\sigma/d\omega$ for pion with polarizability α_π to the corresponding differential cross section for the point-like pion (Born cross section, see Fig. 3.5) can be approximately expressed as [48]:

$$R(\omega) = 1 - \frac{3}{2} \cdot \frac{\omega^2}{1-\omega} \cdot \frac{m_\pi^3}{\alpha} \cdot \alpha_\pi. \quad (3.22)$$

The ratios R for the different values of α_π are presented in Fig. 3.6, from which one can see that the most visible effects of the polarization correspond to large values of ω.

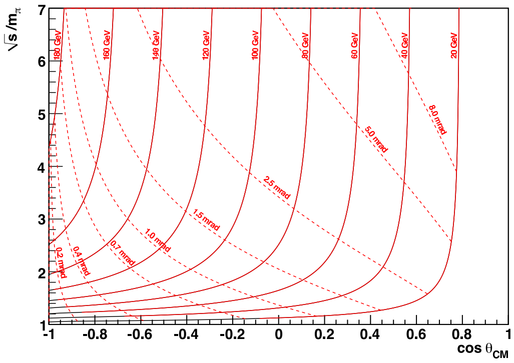

Figure 3.4: Relationship between kinematic variables in anti-laboratory and laboratory systems for energy of incoming pion 190 GeV.

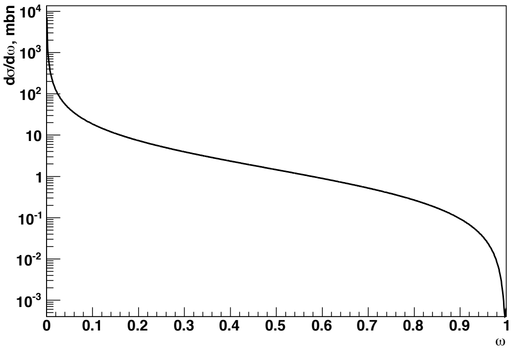

Figure 3.5: The Primakoff differential cross section $d\sigma/d\omega$ of point-like pion scattering off the lead nucleus.

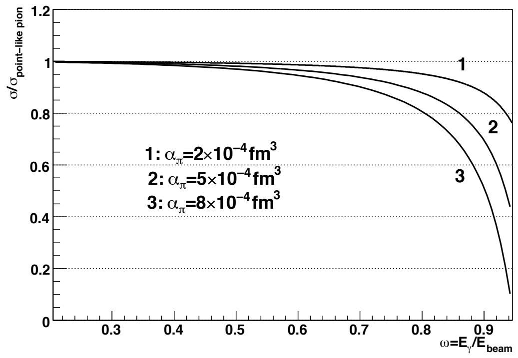

Figure 3.6: The ratio $R(\omega)$ for different values of pion polarizability α_π

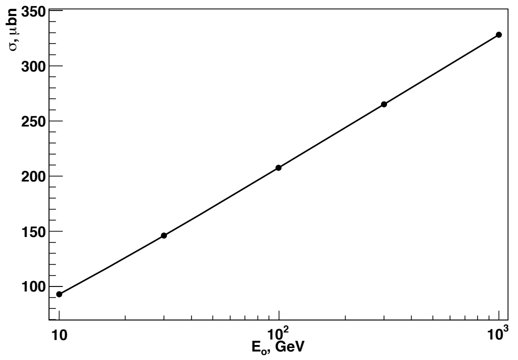

Figure 3.7: The Primakoff cross section for $0.5 < \omega < 0.9$ (point-like pion, Pb).

3.3 The general requirements to the experimental setup for Primakoff reaction studies

Peculiarities of the Primakoff reaction put the general requirements for the experimental setup, strategy of data taking and analysis.

3.3.1 Target

In addition to the scattering of pions in the electromagnetic field of nucleus, there is a nuclear diffractive scattering with the same signature but for which the momentum transfer is much larger. The diffractive scattering produces a significant contribution to a counting rate in the region of large Q^2, while the Primakoff events are peaked at $Q^2 \simeq 0$, but some contribution from the diffractive scattering is even under the Primakoff peak. To separate Primakoff and diffractive scattering, the experimental setup must have a good resolution in Q^2. Multiple scattering in a target material is one of the main sources of uncertainties in Q^2 measurement and it limits the thickness of the target. One should also take into account the probability of Primakoff photon lost due to its conversion into e^+e^- pair within the target, that decreases the acceptance. So, the thickness of the target should be much less than one radiation length.

To optimize the ratio of Primakoff signal, which is proportional to Z^2, to diffractive background, the material with large Z is preferable for the target. But Z should not be too large to minimize radiative corrections to the

Born cross section [52]-[56]. These corrections and corresponding systematic shifts of α_π are shown in Fig. 3.8 and 3.9. Corrections for Compton vertex, multiple photon exchange, vacuum polarization , electromagnetic form factor of nucleus and nuclear charge screening by electrons are taken into account.

3.3.2 Beam

The cross section of Primakoff scattering just logarithmically depends on the energy of incoming pion (see Eq. 3.17-3.19 and Fig. 3.7) up to the energies about 10^4 GeV for which Landau-Pomeranchuk-Migdal effect [50], [51] becomes significant. So, variation of the beam energy doesn't change significantly the cross section and therefore the statistics. But the scale of energies of incoming and outgoing particles determines the quality of collected data. For instance, for small energies the multiple scattering in the target material makes a significant problem, while for high energies small scattering angle of Primakoff photon makes worse the resolution in Q^2. So the beam energy should be optimized in each particular case with respect to such parameters of a setup as the spatial resolution of tracking detectors, the spatial and energetic resolution of the electromagnetic calorimeter, the amount of the material in the beam line (including target) etc.

As for the sign of the beam pions, the positive and negative pions are equivalent. But in practice it is simpler to form the beam of negative pions, where the admixture of other particles is small enough. Positive beams are usually contaminated by protons.

3.3.3 Detector

The configuration of Primakoff events requires the precise tracking up- and downstream of the target to measure the pion scattering angle, an electromagnetic calorimeter to measure energy and position of the photon cluster and a magnetic spectrometer for scattered pion momentum measurement. Taking into account that it is difficult to form pure pion beam the setup should have possibilities to identify incoming and outgoing particles.

3.3.4 Trigger

A hard photon in the final state is the most important signature of Primakoff reaction. So, the significant energy deposition in the electromagnetic calorimeter can be the main requirement for the Primakoff trigger.

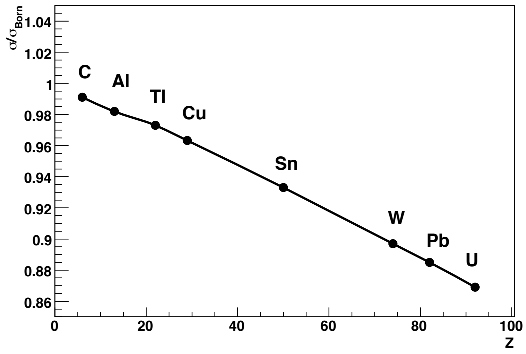

Figure 3.8: Radiative corrections to the Primakoff cross section as a function of Z.

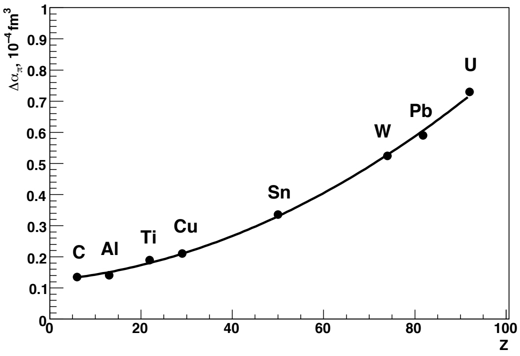

Figure 3.9: Systematic shifts of α_π due to radiative corrections for different Z.

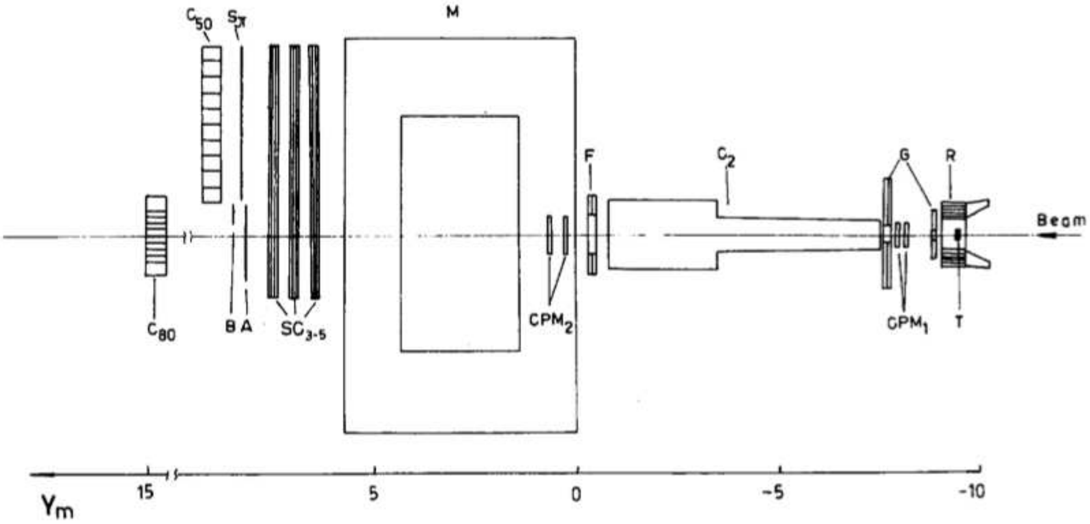

Figure 3.10: Layout of the SIGMA-AYAKS spectrometer.

3.4 Pion polarizabilities measurement in Serpukhov

The first measurement of pion polarizabilities via the Primakoff reaction was proposed in [46] and performed with the SIGMA-AYAKS spectrometer

(Fig. 3.13) in Serpukhov in the 40 GeV/c negative beam ([38],[39],[47],[48],[49]). Beam particles were identified by the differential and threshold gas Cherenkov counters and their tracks were measured by hodoscopes and proportional chambers. The main statistics was collected with $0.25X_0$ carbon target (T), but Be, Al, Fe, Cu and Pb targets were also used. The scattered pions were detected by the magnetic spectrometer. The gas Cherenkov counter C_2 was used to set the upper limit on scattered π^- momenta (P_{max}=18 GeV/c). The energy and the position of the photons were measured by 80 lead glass Cherenkov counters (C_{80}). Guard counters (R,G,F) were used to identify the events with large scattering angle. A system of 50 lead glass Cherenkov counters C_{50} was used to suppress possible beam electron bremstrahlung. The trigger required the energy deposition in the lead glass counters above 5 GeV, no signals from guard counters, and a signal produced by scattered pion in the hodoscope.

The following criteria were used for offline selection of Primakoff events:

- only one negative particle with the momentum (4-18) GeV/c detected in the spectrometer;
- the pion scattering angle greater than 1.5 mrad;
- the tracks of incident and scattered pions crossing in the target;
- only one photon detected in C_{80};
- $35\ GeV < E_\gamma + E_\pi < 45\ GeV$ (exclusivity requirement);
- $Q^2 < 6 \times 10^{-4} (GeV/c)^2$.

The main parameters of the spectrometer are presented in Table 4.5. Figures 3.11 and 3.12 show the exclusivity peak and Q^2-distributions for different target materials. The total Primakoff statistics collected with all targets was about 6 000 events that allowed to measure pion polarizability α_π under assumption $\alpha_\pi + \beta_\pi = 0$ with the statistical error $1.4 \times 10^{-4}\ fm^3$ and systematic error $1.2 \times 10^{-4}\ fm^3$. Independent estimation of α_π and β_π was performed with the statistical accuracy $2.8 \times 10^{-4}\ fm^3$ and systematic accuracy $1.8 \times 10^{-4}\ fm^3$. The contribution to the result from the radiative correction was estimated to be about $0.2 \times 10^{-4}\ fm^3$ [54].

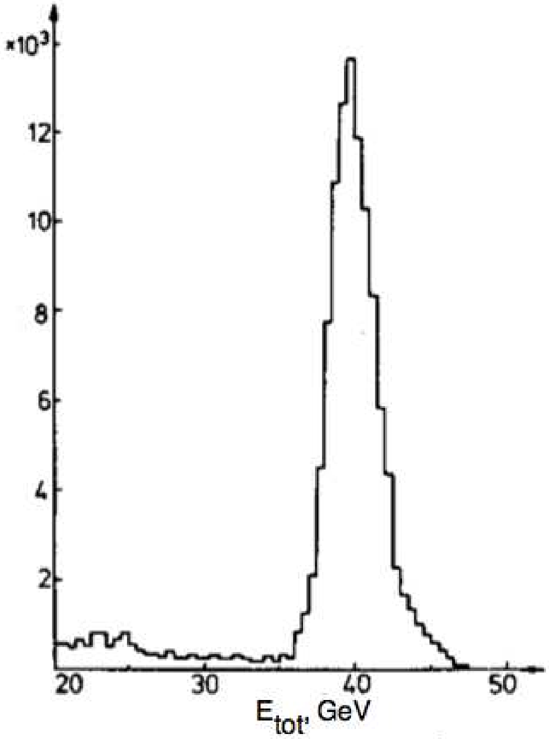

Figure 3.11: The distribution for $E_{tot} = E_\gamma + E_\pi$ in the experiment SIGMA-AYAKS [38].

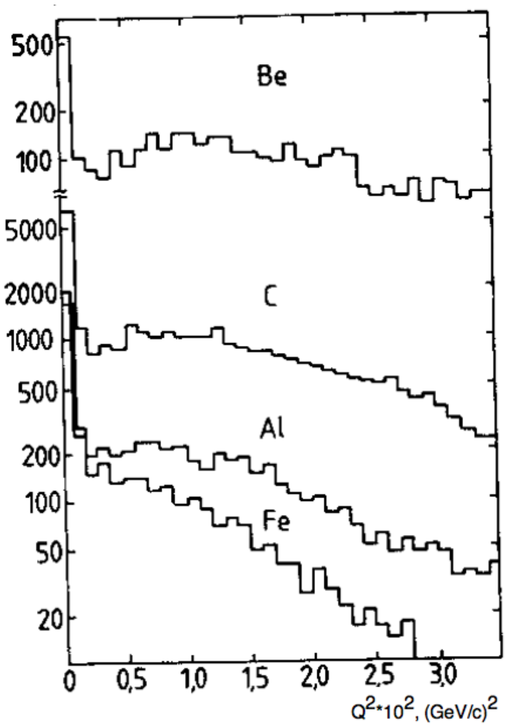

Figure 3.12: The Q^2-distributions for different targets in the experiment SIGMA-AYAKS [38].

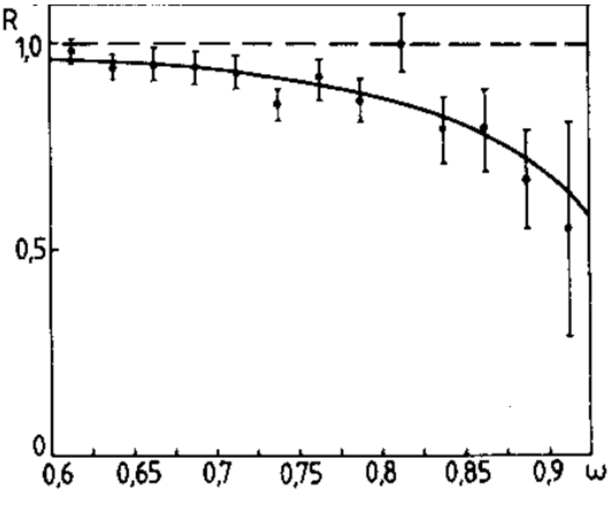

Figure 3.13: $R(\omega)$ obtained in Serpukhov experiment [48].

Chapter 4

The COMPASS experiment

4.1 The COMPASS physics program

COMPASS (COmmon Muon and Proton Apparatus for Structure and Spectroscopy) is an experiment at the secondary beam of Super Proton Synchrotron (SPS) at CERN. The purpose of this experiment is the study of hadron structure and hadron spectroscopy with high intensity muon and hadron beams [57]. The COMPASS physics program consists of two parts: program with muon beam and program with hadron beam. Muon program includes:

- study of the longitudinal spin structure of the nucleon. COMPASS investigates the polarization of quarks and gluons inside nucleons from the analysis of deep inelastic scattering. In particular the gluon contribution $\Delta G/G$ to the total nucleon spin is directly measured. Three approaches make possible to extract $\Delta G/G$ by analyzing events with either D mesons (open-charm), hadron pairs with large transverse momenta (high-pT) or single high-pT hadrons being produced;
- study of the transverse spin distributions. They are accessible via Collins and Sivers asymmetries, which have been measured by COMPASS with a transversely polarized target;
- study of Λ polarization. In addition to the valence quark distributions also the polarization of sea quarks is subject of ongoing investigations. In case of a polarized target, the virtual photon exchanged during the deep inelastic scattering process can transfer the polarization to a detectable

Λ baryon. If the target is unpolarized, also the spontaneous polarization of the latter is examined.

At the moment the most part of muon program is completed and results are published.

In COMPASS hadron program [58] the strong interaction is approached from various sides in order to learn more about its fundamental properties. Glueballs and hybrids are searched for, chiral perturbation theory is tested in central production, diffractive dissociation, and Primakoff reactions. Physics program with hadron beam includes the following points:

- precise measurement of pion polarizabilities to clarify present uncertain situation;
- first observation of Compton scattering with kaons and first estimation of kaon polarizabilities;
- study of chiral anomaly. The process $\pi^- + \gamma \rightarrow \pi^- + \pi^0$ involves anomalous vertex, which can be treated in the framework of χ PT. This vertex is also accessible via the Primakoff scattering $\pi^- + Z \rightarrow \pi^- + \pi^0 + Z$;
- observation of hybrid mesons production via the Primakoff reaction. Hybrid mesons can be produced via the reactions $\pi^- + \gamma \rightarrow \rho + \pi, \eta + \pi, \eta' + \pi, \pi + b_1, \pi + f_1$ and similar reactions with kaon beam;
- searching for glueballs, exotic and hybrid mesons. COMPASS has possibility to use of different production mechanisms: peripheral hadron scattering, diffractive dissociation and central production. Such data should provide significant input for gaining a better understanding of non-perturbative QCD.

Short pilot run with hadron beam was performed in 2004. Then hadron program was renewed only in 2008.

Such points of future COMPASS physics program like deeply virtual Compton scattering (DVCS) study and Drell-Yan process study with polarized target to access the generalized parton distributions (GPD) are under discussion.

4.2 Short history of COMPASS

Shortly the history of COMPASS experiment can be presented in the following chronological sequence:

- March 1996: The Hadron-Muon Collaboration (HMC) and the CHarm Experiment with Omni Purpose Setup (CHEOPS) experimental groups submitted a joint COMPASS proposal;
- February 1997: The experiment was approved conditionally by CERN;
- September 1998: The final Memorandum of Understanding was signed;
- 1999 - 2000: Installation of the experimental setup;
- 2001: Technical run, and commissioning of the setup;
- 2002: COMPASS started data taking with muon beam;
- October - November 2004: Pilot hadron run;
- 2005: One year of shutdown;
- 2008 - till now: Data taking with hadron beam.

4.3 Possibility to measure pion polarizabilities at COMPASS

The COMPASS setup basically meet the requirements, formulated in Sec. 3.3 and needed for pion polarizabilities measurement ([59]-[62]). It has silicon detectors (Sec. 4.4.4) up- and downstream of the target for the precise vertex position reconstruction and for the measurement of the pion scattering angle, an electromagnetic calorimeter (Sec. 4.4.6) for the photon 4-momentum reconstruction, two magnetic spectrometers (Sec. 4.4.2, 4.4.3) for determination of the scattered pion momentum. Hadron calorimeters (Sec. 4.4.6) and a muon identification system (Sec. 4.4.5) are used for identification of secondary particles.

In COMPASS there is an unique possibility to study the reaction with a μ^- beam:

$$\mu^- + (A, Z) \to \mu^- + (A, Z) + \gamma. \tag{4.1}$$

Since the muon is a point-like particle, the ratio of the measured differential cross section to the calculated cross section (taking into account that spin of muon is $\frac{1}{2}$) have to be equal to unity. This is the best way to estimate and eliminate systematic uncertainties.

Taking into account the experience of SIGMA-AYAKS experiment, using the power of the modern technologies, methods of high energy physics and computing facilities, COMPASS can perform the measurement of pion polarizabilities via the Primakoff reaction with higher precision, compared to previous experiments.

High beam intensity and the possibility to identify beam particles permit to perform the measurements also with K-meson.

The comparison of the SIGMA-AYAKS and COMPASS spectrometers for the Primakoff reaction studies is given in Table 4.5.

4.4 Layout of the COMPASS spectrometer

So long as the COMPASS spectrometer is all-purpose detector intended for effective registration of different physics processes, not all subdetectors are involved into the registration of Primakoff reaction. This section describes the general layout of the spectrometer as it was used in muon run 2004, modifications applied before the pilot hadron run 2004, Primakoff trigger and subdetectors, the most important for Primakoff studies like silicones and electromagnetic calorimeter. The beams (pion and muon) and targets used during pilot hadron run are also described here. Information about cryogenic polarized target, triggers used in muon program and also the detailed information about other subdetectors can be found in [59].

The basic layout of the COMPASS spectrometer is shown in Fig. 4.1. Three parts can be distinguished. The first part includes the detectors upstream of the target, which measures the incoming beam particles. The second and the third part of the setup are located downstream of the target, and extend over a total length of 50 m. These are the large angle spectrometer and the small angle spectrometer, respectively. The use of two spectrometers for the outgoing particles is a consequence of the large momentum range and the large angular acceptance requirements. Each of the two spectrometers is built around an analyzing magnet, preceded and followed by telescopes of trackers and completed by a hadron calorimeter and by a muon filter station for high energy muon identification. A RICH detector for secondary hadron identification is part of the large angle spectrometer.

The flexibility required by the broad spectrum of the COMPASS physics program has been implemented by mounting huge setup elements on rails, allowing them to be positioned at variable distances from the experimental target: the RICH, the first hadron calorimeter, the first muon filter, the second analyzing magnet and the trackers fixed to it can move longitudinally on rails.

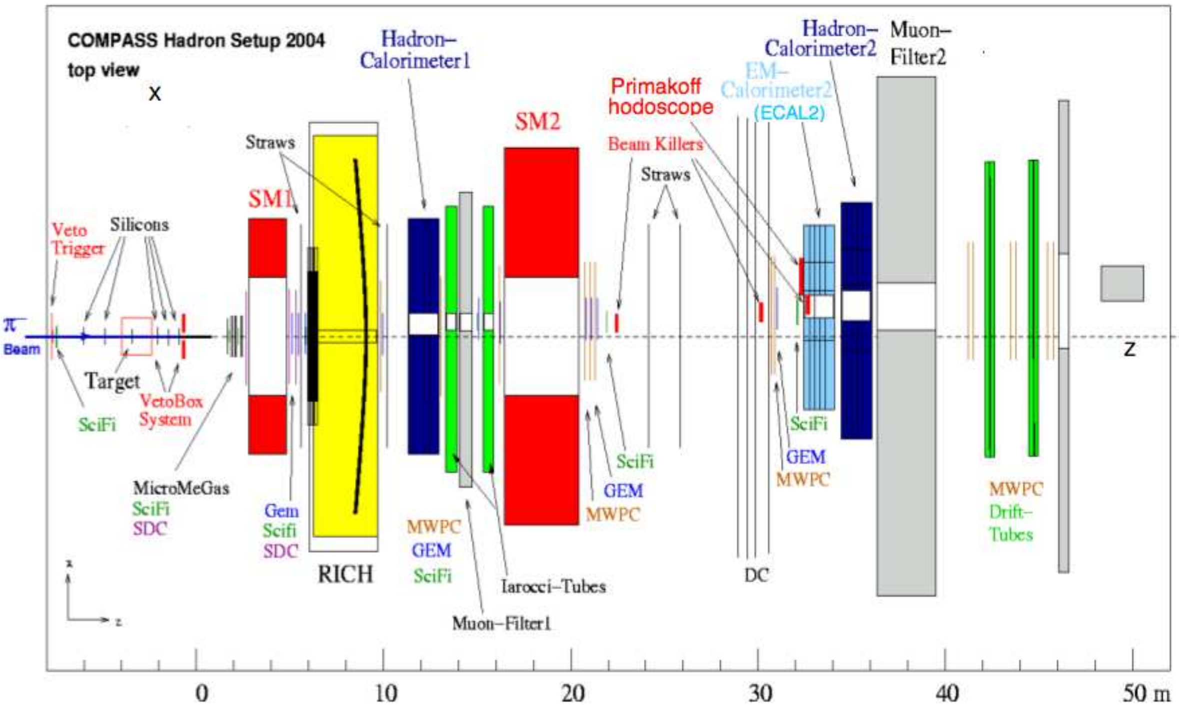

Figure 4.1: Layout of the COMPASS setup 2004.

Table 4.1 provides an overview of the different detectors used in COMPASS and their main parameters. The detectors are grouped according to their positions and functions in the spectrometer.

Table 4.1: Overview of detectors used in COMPASS, together with their respective main parameters, grouped according to their geometrical positions along the beam line (stations) and functions in the spectrometer. The first column shows the naming convention for the respective stations. The second column gives the number of detectors making up these stations, while the third column specifies the coordinates measured by the detectors. Here, e.g. XY means that both projections are measured by each detector, while X/Y means that only one of two coordinates X or Y is measured by one of the detectors. Typical values for resolutions of one detector at standard COMPASS muon beam conditions are given, where appropriate, in the sixth column. Here, σ_s denotes the r.m.s. spatial resolution along one coordinate, σ_t the r.m.s. time resolution, σ_ph the single photon resolution, σ_ring the ring resolution.

Station	# of dets.	Planes per det.	# of ch. per det.	Active area $X \times Y$ (cm^2)	Resolution
			Beam detectors		
BM01-04	4	Y	64	$6-12 \times 9-23$	$\sigma_\mathrm{s} = 1.3-2.5\ mm$, $\sigma_t = 0.3\ ns$
BM05	2	Y	64	12×16	$\sigma_\mathrm{s} = 0.7\,\mathrm{mm}$, $\sigma_t = 0.5\ ns$
BM06	2	Y	128	12×16	$\sigma_\mathrm{s} = 0.4\,\mathrm{mm}$, $\sigma_t = 0.5\,\mathrm{ns}$
SciFi 1,2	2	XY	192	3.9×3.9	$\sigma_\mathrm{s} = 130\,\mu\mathrm{m}$, $\sigma_t = 0.4\,\mathrm{ns}$
Silicon	2	$XYUV$	2304	5×7	$\sigma_\mathrm{s} = 8-11\,\mu\mathrm{m}$, $\sigma_t = 2.5\,\mathrm{ns}$
			Large angle spectrometer		
SciFi 3,4	2	XYU	384	5.3×5.3	$\sigma_\mathrm{s} = 130\,\mu\mathrm{m}$, $\sigma_t = 0.4\,\mathrm{ns}$
Micromegas	12	$X/Y/U/V$	1024	40×40	$\sigma_\mathrm{s} = 90\,\mu\mathrm{m}$, $\sigma_t = 9\,\mathrm{ns}$
DC	3	$XYUV$	1408	180×127	$\sigma_\mathrm{s} = 190\,\mu\mathrm{m}$
Straw	9	$X/Y/U/V$	892	323×280	$\sigma_\mathrm{s} = 190\,\mu\mathrm{m}$ [a]
GEM 1-4	8	XY/UV	1536	31×31	$\sigma_\mathrm{s} = 70\,\mu\mathrm{m}$, $\sigma_t = 12\,\mathrm{ns}$
SciFi 5	1	XY	320	8.4×8.4	$\sigma_\mathrm{s} = 170\,\mu\mathrm{m}$, $\sigma_t = 0.4\,\mathrm{ns}$
RICH-1	8	1 (pads)	10368	60×120	$\sigma_\mathrm{ph} = 1.2\,\mathrm{mrad}$ $\sigma_\mathrm{ring} = 0.55\,\mathrm{mrad}$ (for $\beta = 1$)
MWPC A*	1	$XUVY$	2768	178×120	$\sigma_\mathrm{s} = 1.6\,\mathrm{mm}$
HCAL1	1	1	480	420×300	$\Delta E/E = 0.59/\sqrt{E/\mathrm{GeV}} \oplus 0.08$
MW1	8	X/Y	1184/928	473×405	$\sigma_\mathrm{s} = 3\,\mathrm{mm}$
			Small angle spectrometer		
GEM 5-11	14	XY/UV	1536	31×31	$\sigma_\mathrm{s} = 70\,\mu\mathrm{m}$, $\sigma_t = 12\,\mathrm{ns}$
MWPC A	7	XUV	2256	178×120	$\sigma_\mathrm{s} = 1.6\,\mathrm{mm}$
SciFi 6	1	XYU	462	10×10	$\sigma_\mathrm{s} = 210\,\mu\mathrm{m}$, $\sigma_t = 0.4\,\mathrm{ns}$
SciFi 7	1	XY	286	10×10	$\sigma_\mathrm{s} = 210\,\mu\mathrm{m}$, $\sigma_t = 0.4\,\mathrm{ns}$
SciFi 8	1	XY	352	12.3×12.3	$\sigma_\mathrm{s} = 210\,\mu\mathrm{m}$, $\sigma_t = 0.4\,\mathrm{ns}$
Straw	6	$X/Y/U/V$	892	323×280	$\sigma_\mathrm{s} = 190\,\mu\mathrm{m}$ [a]
Large area DC	6	$XY/XU/XV$	500	500×250	$\sigma_\mathrm{s} = 0.5\,\mathrm{mm}$
ECAL2	1	1	2972	245×184	$\Delta E/E = 0.06/\sqrt{E/\mathrm{GeV}} \oplus 0.02$
HCAL2	1	1	216	440×200	$\Delta E/E = 0.66/\sqrt{E/\mathrm{GeV}} \oplus 0.05$
MWPC B	6	XU/XV	1504	178×90	$\sigma_\mathrm{s} = 1.6\,\mathrm{mm}$
MW2	2	XYV	840	447×202	$\sigma_\mathrm{s} = 0.6-0.9\,\mathrm{mm}$

---

[a] Resolution measured for 6 mm straw tubes only, corresponding to an active area of $110 \times 350\,\mathrm{cm}^2$

4.4.1 Beam telescope and beam spectrometer

The first part of the setup includes the Beam Momentum Station (BMS), located along the beam line about 100 m upstream of the experimental hall. This beam spectrometer measures the momentum of the incoming muon on an event by event base; it includes an analysing magnet and two telescopes of tracking stations formed by scintillator hodoscopes and scintillating fibre (SciFi) detectors.

A precise track reconstruction of the incident particle is provided by fast trackers located upstream of the target. There are two stations of scintillating fibres and three stations of silicon microstrip detectors. Scintillator veto counters define the beam spot size and separate the beam from the beam halo.

4.4.2 Large angle spectrometer

The second part, i.e. the Large Angle Spectrometer (LAS), has been designed to ensure 180 mrad polar acceptance. It is built around the SM1 magnet, which is preceded and followed by telescopes of trackers.

SM1 is a dipole magnet located 4 m downstream of the target centre. It is 110 cm long, has a horizontal gap of 229 cm and a vertical gap of 152 cm in the middle. The pole tips of the magnet are wedge-shaped with the apex of the edge facing the target, so that the tracks pointing to the target are orthogonal to the field lines. The SM1 vertical size matches the required angular acceptance of ±180 mrad. The main component of the field goes from top to bottom. Its field integral was measured to be $1.0\ T \times m$ and corresponds to a deflection of 300 mrad for particles with a momentum of 1 GeV/c. Due to the bending power of SM1, the LAS detectors located downstream of SM1 need to have an angular acceptance of ±250 mrad in the horizontal plane.

The SM1 magnet is followed by a RICH detector with large transverse dimensions to match the LAS acceptance requirement, which is used to identify charged hadrons with momenta ranging from a few GeV/c to 43 GeV/c. The LAS is completed by a large hadron calorimeter (HCAL1) with a central hole matching the second spectrometer acceptance. The calorimeter detects outgoing hadrons and is used in the trigger formation. The LAS is completed by a muon filter.

4.4.3 Small angle spectrometer

The third part of the COMPASS setup, the Small Angle Spectrometer (SAS), detects particles at small angles (±30 mrad) and large momenta of 5 GeV/c and higher. Its central element is the 4 m long SM2 magnet, located 18 m downstream of the target centre and preceded and followed by telescopes of trackers.

SM2 is a rectangular shape dipole magnet with a gap of $2 \times 1\,\mathrm{m}^2$ and a total field integral of $4.4\ T \times m$ for its nominal current of 4000 A. As for SM1, its main field component is in the vertical direction. The SM2 magnet was used in several experiments prior to COMPASS; its magnetic field is known from previous measurements. The downstream part of the SAS part includes electromagnetic and hadron calorimeters and a muon filter. Each of these elements has a hole matching the acceptance of the quasi-real photon trigger. The electromagnetic calorimeter (ECAL2) is used to detect gammas and neutral pions. The SAS hadron calorimeter (HCAL2), as well as HCAL1, is used in the trigger formation. A second muon filter is positioned at the downstream end of the spectrometer.

4.4.4 Tracking detectors

The particle flux per unit transverse surface varies by more than five orders of magnitude in the different regions included in the overall spectrometer acceptance. Along the beam, or close to the target, the detectors must combine a high particle rate capability (up to a few MHz/channel) with an excellent space resolution (100 μm and better). The amount of material along the beam path has to remain at a minimum in order to minimize multiple scattering and secondary interactions. These requests are particularly severe upstream of the SM1 magnet where the incident flux is further increased because of the large number of low energy secondary particles coming from the target region. Far from the beam, the resolution constraint can be relaxed, but larger areas need to be covered. Different tracking techniques, including novel ones, are employed in regions at different distance from the beam axis, in order to match the requirements concerning rate capability, space and time resolution as well as the size of the surface to be instrumented. Different varieties of large gaseous detectors based on wire amplification are used for the regions further away from the beam, with their central regions deactivated in order not to exceed their rate capability. The near-beam and beam regions are covered by fast scintillating, gaseous and silicon tracking detectors, respectively, with active areas overlapping the dead zones of the larger detectors to guarantee efficient track reconstruction and good relative alignment.

The tracking detectors are grouped as (see also Table 4.1):

- Very Small Area Trackers (VSAT) - These detectors, small in size, must combine high flux capabilities and excellent space or time resolutions. The area in and around the beam is covered by eight scintillating fibres stations, and, upstream of the target, by three stations of double-sided silicon microstrip detectors. Their lateral sizes vary from 4 cm to 12 cm, to take into account the beam divergence depending on the position along the beam axis.

- Small Area Trackers (SAT) - For distances from the beam larger than 2.5 cm medium size detectors, featuring high space resolution and minimum material budget are required. COMPASS uses three Micromegas (Micromesh Gaseous Structure) stations, and 11 GEM (Gas Electron Multiplier) stations. Each Micromegas station is composed of four planes and has an active area of $40 \times 40\,\mathrm{cm}^2$. All three stations are located between the target and the SM1 magnet. Each GEM station consists of two detectors with an active area of $31 \times 31\,\mathrm{cm}^2$, each measuring two coordinates. The 11 GEM stations cover the region from the downstream side of SM1 to the far end of the COMPASS setup. Both Micromegas and GEM detectors have central dead zones with 5 cm diameter.

- Large Area Trackers (LAT) - At large angles the trackers provide good spatial resolution and cover the large areas defined by the experimental setup acceptance. In the LAS, particles emerging at large angles are tracked by three Drift Chambers (DC), one located upstream of SM1 and two immediately downstream of it. All DC have an active area of $1.8 \times 1.3\,\mathrm{m}^2$ with a central dead zone of 30 cm diameter. They are followed by three stations of straw drift tubes, two upstream and one downstream of the RICH counter. Each straw station consists of two planes of size $323 \times 280\,\mathrm{cm}^2$ and one plane of size $325 \times 243\,\mathrm{cm}^2$, all of which have a central dead zone of $20 \times 20\,\mathrm{cm}^2$. From downstream of the RICH counter to the far end of the setup the particles scattered at relatively small angles are detected by 14 multi-wire proportional chamber (MWPC) stations with active areas of $1.8 \times 0.9 - 1.2\,\mathrm{m}^2$ and the diameters of their insensitive central zones increasing along the beam line from 16 to 22 cm. The outer region downstream of SM2 is covered by two additional straw stations of the same sizes as above, and by six large area drift chambers of $5.0 \times 2.5\,\mathrm{m}^2$ active surface and 50 cm or 100 cm diameter central dead zone.

Silicon microstrip detectors

The COMPASS silicon microstrip detectors are used for the detection of the incoming muon beam track and for the hadron program for vertex and track reconstruction downstream of the target.

The high beam intensity in COMPASS requires a radiation hard detector design and an excellent spatial and time resolution.

The silicon wafer, optimized for high fluence, was originally designed and developed for the HERA-B experiment. The $300\,\mu\mathrm{m}$ thick n-type wafer has an active area of $5 \times 7\,\mathrm{cm}^2$. The 1280 readout strips on the n-side ($54.6\,\mu\mathrm{m}$ pitch) are perpendicular to the 1024 readout strips on the p-side ($51.7\,\mu\mathrm{m}$ pitch), so that with one wafer two-dimensional position information can be obtained. This reduces the material budget by a factor of two as compared to a single-sided readout.

The silicon wafer is glued with silicone glue onto a frame consisting of two L-shaped Printed Circuit Boards (L-board) forming a detector. The readout strips, which are tilted by 2.5° with respect to the wafer edge, are connected via $25\,\mu\mathrm{m}$ aluminium wire bonds and a glass pitch adapter to the front-end chips. Along two wafer edges a capillary is soldered onto the back side of the L-board and is electrically insulated by a connector of epoxy material. The capillary is flushed with gaseous nitrogen (400 l/h) to cool the front-end chips. The setup of a COMPASS silicon detector is shown in Fig. 4.2.

The analogue signals induced on the microstrips are read out using the APV25 front-end chip, a 128-channel preamplifier/shaper ASIC with analogue pipeline, originally developed for the CMS silicon microstrip tracker [63]. Each channel of the APV25 consists of an inverter stage with unit amplification to allow signals of both polarity to be processed, and a CR-RC type shaping amplifier with a time constant of 50 ns. The amplifier output amplitudes are sampled at a frequency of 38.88 MHz, using the reference clock of the trigger control system (TCS) of the experiment, and stored in a 192 cell analogue pipeline. Upon arrival of an external trigger at the chip, the cells corresponding to the known trigger latency (up to $4\,\mu$s) are flagged for readout. The analogue levels of the flagged cells for 128 channels are then multiplexed at 20 MHz onto a single differential output. In order to obtain time information from the signal shape, not only the sample corresponding to the peak of an in-time signal is transferred, but in addition two samples on the rising edge of such a signal are read out. While the sampling in the APV25 as well as the trigger signal are synchronized to the reference clock of the TCS, the passage of a particle is not. The resulting shift between the TCS clock phase and the actual time of particle passage, being randomly distributed in the 25.7 ns window for each event, is corrected during the reconstruction. It is determined by the difference of the rising edge of the TCS clock and the trigger time, and is measured via a TDC event by event. The multiplexed analogue data stream from each APV25 chip is digitized by a 10 bit flash ADC.

Two detectors make up one silicon station. They are mounted back-to-back on a fibre-glass frame such that one detector measures the horizontal (X) and vertical (Y) coordinates of a particle trajectory, while the other is rotated around the beam axis by 5°, providing two additional projections (U, V). [64]. The wafers are oriented such that the X and U planes constitute the n-side, and the Y and V planes the p-side of the wafer, respectively.

The residuals were calculated for standard muon run conditions using silicon detectors only, so that the track error ($< 3\,\mu$m) could be easily deconvoluted. The spatial resolution strongly depends on the cluster size (number of neighbouring hit strips combined to one cluster) since for more than one hit strip the spatial information can be refined by calculating the mean of strip coordinates of one cluster, weighted by the corresponding amplitude and taking into account the strip response function. The ratio of hits with cluster size 2 to hits with cluster size 1 is 1.0 for the p-side (Y-, V-planes) and 0.4 for the n-side (X-, U-planes), and is mainly given by the design of the wafer. The charge sharing is improved on the p-side by additional capacitive coupling due to intermediate strips. The results for an improved spatial resolution for the Y- and V-planes compared to the X- and U-planes, can be seen from the residual distributions shown in Fig. 4.5 for a Y-plane, and Fig. 4.4 for an X-plane, respectively. The average spatial resolution of the COMPASS silicon detectors is $8\,\mu$m for the p-side, and $11\,\mu$m for the n-side.

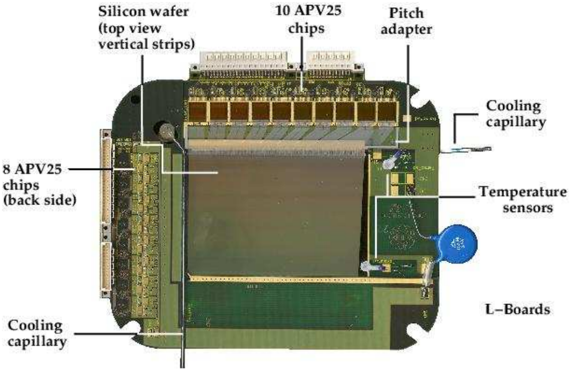

Figure 4.2: Front view of a COMPASS silicon detector.

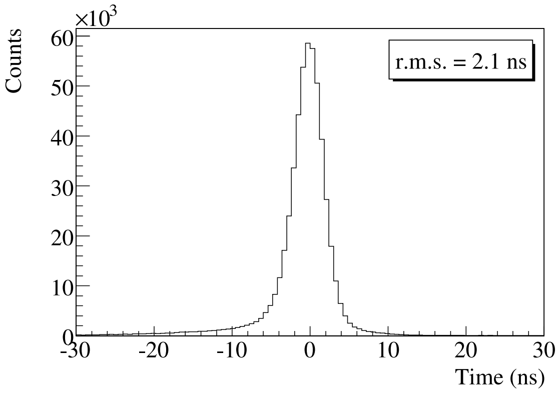

Figure 4.3: Signal time distribution of a single projection of a silicon detector.

Figure 4.3 shows the signal time distribution for one plane of a silicon detector. The average time resolution was found to be $\langle\sigma_t\rangle = 2.5\,$ns.

For the COMPASS hadron pilot run in 2004, two silicon stations were installed upstream of the target for the detection of beam tracks and three downstream of the target for vertex and track reconstruction. During this period the central regions of the detectors were irradiated by $8 \cdot 10^{11}$ pions/cm^2. For the future COMPASS data taking periods with high intensity hadron beams a fluence of about 10^{13} hadrons/cm^2 will be reached in the central beam area, requiring advanced methods to increase the radiation hardness

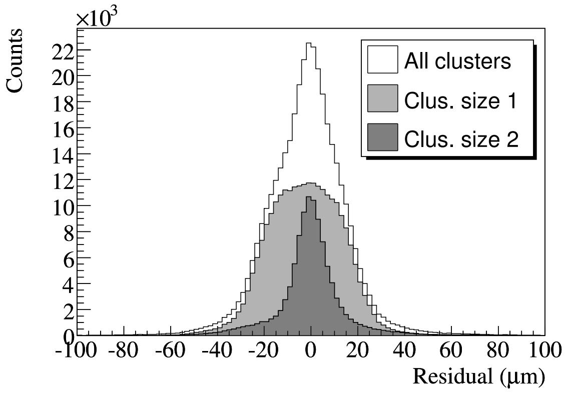

Figure 4.4: Residual distribution for one silicon X-plane. In light grey the distribution for cluster size 1 and in dark grey for cluster size 2 are shown.

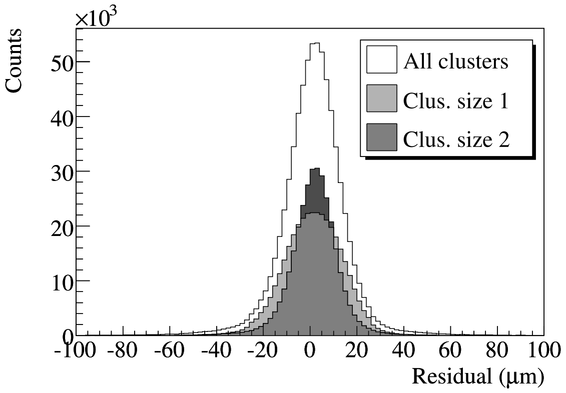

Figure 4.5: Residual distribution for one silicon Y-plane. In light grey the distribution for cluster size 1 and in dark grey for cluster size 2 are shown.

of silicon detectors. In COMPASS this will be achieved by exploiting the Lazarus effect [65], which results in a recovery of the charge collection efficiency (CCE) for irradiated detectors when operated at cryogenic temperatures. It has been shown experimentally, that the CCE recovery is greatest for operation temperatures around 130 K. The silicon detector system used at present has already been designed for such cryogenic operation [64]. To this end the silicon detectors are housed in vacuum tight cryostats with low mass and light tight detector windows. The detectors will be cooled by flushing the capillary along the wafer edge (see Fig. 4.2) with liquid nitrogen instead of gaseous nitrogen.

4.4.5 Muon filters

Identification of the scattered muons is performed by two dedicated muon filters. The design principle of a muon filter includes an absorber layer, preceded and followed by tracker stations (Muon Walls) with moderate space resolution. The absorber is thick enough to stop incoming hadrons. Muons are positively identified when a track can be reconstructed in both sets of trackers placed upstream and downstream of the absorber.

The first Muon Wall (MW1) is located at the downstream end of LAS, in front of SM2. It consists of two stations of squared drift tubes, each with an active area of $4.8 \times 4.1\,\mathrm{m}^2$ and a central hole of $1.4 \times 0.9\,\mathrm{m}^2$. An iron wall, 60 cm thick, is placed between the two stations.

The second Muon Wall (MW2) is installed at the very end of the SAS. The absorber is a 2.4 m thick concrete wall. The portion of the trajectory upstream of the concrete wall is reconstructed by the SAS trackers, while downstream of it there are two dedicated stations of steel drift tubes with an active surface of $4.5 \times 2.0\,\mathrm{m}^2$ each.

Muon wall 2

Muon wall 2 (MW2) consists of two identical stations of layers of drift tubes. Each of the two stations consists of 6 layers with an active area of $447 \times 202\,\mathrm{cm}^2$ grouped into double layers, each mounted to a separate steel frame. The three double layers have vertical, horizontal and inclined (at -15° with respect to the vertical) tubes, respectively.

The stainless steel drift tubes with an inner diameter of 29 mm and a wall thickness 0.5 mm were originally designed for the muon system of the DØ experiment. The layout of the tubes in a double layer is shown in Fig. 4.6. The pitch of the wires in a layer is 33.5 mm. Each tube is inserted into precise guide holes in the frame and fixed with a clamp. The removable fixation allows a replacement of damaged or malfunctioning tubes. The total numbers of tubes in the two stations is 1680.

A rectangular hole in each plane of the detector with a size of $1 \times 0.8\,\mathrm{m}^2$ around the beam is realised using properly shortened tubes. The hole is covered by the MWPC-B stations, which partly overlap with the sensitive area of MW2.

One end of each tube hosts a high voltage filter with a $1\,\mathrm{M}\Omega$ resistor connected with the gold-plated tungsten anode wire of $50\,\mu$m in diameter. The high voltage is delivered to a group of filters through a distribution board mounted on the layer frame. The other end of the tube is equipped with a separate capacitively coupled amplifier-discriminator (AD) connected directly to the signal (anode) and grounding pins of the tube, the latter being soldered to the tube body. The effective threshold of the AD is set to 9 fC. The LVDS outputs of a group of up to 64 ADs are collected with a short (up to 0.5 m) flat cable on a printed circuit which is fixed to the plane frame.

This PCB hosts the F1-TDC board operating in the "standard resolution" mode, and also supplies the low voltage including threshold offset to the ADs.

The gas mixture used, Ar/CH$_4$ (75/25), is known for a saturated and rather fast drift of electrons, a wide working plateau and stable performance against radiation ageing. The full drift time of ~ 240 ns at the working high voltage of $+3$ kV determines the two-track resolution.

The space resolution of the tracking through MW2 includes the intrinsic resolution of the detector itself and the track fitting error, so it is worse for the Y planes, as the corresponding projection measurement is generally less redundant, particularly in this zone of the spectrometer. Fig. 4.7(a) shows the residuals for a single MW2 layer. The shape of the distribution is approximated with two gaussians with a common mean: a narrow "core" with a σ of 0.53 up to 0.94 mm (for Y planes) which amounts to 79% to 91% of the entries, and the wide "halo" with a width between 2.0 and 4.8 mm. The spread is mostly due to the irregular spacing of the tubes.

Figure 4.7(b) shows the two dimensional distribution of the measured time of the hit with respect to the trigger time versus the distance of the reconstructed track to the wire. The correlation is fitted with a linear $R(t)$ relation giving an effective drift velocity of between 5.8 and 6.2 cm/μs.

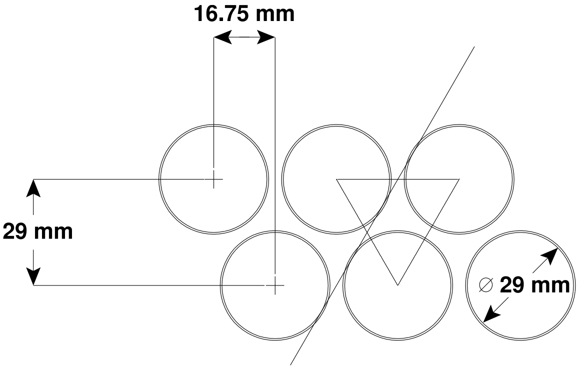

Figure 4.6: The layout of the tubes in a double layer of MW2 planes. Dimensions in mm. An imaginary equilateral triangle formed by centres of three adjacent tubes and a common tangent to their interior are shown.

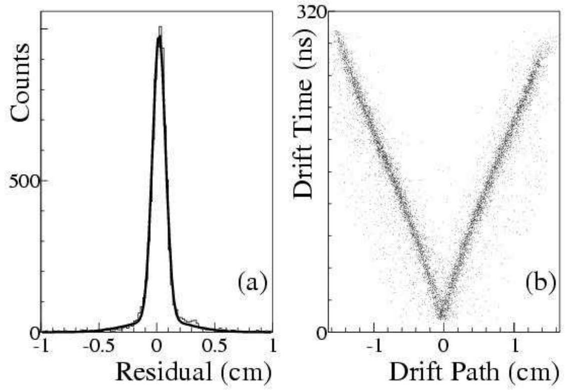

Figure 4.7: (a) Histogram (thin line) of coordinate residuals for a single MW2 plane with the two gaussian fit superimposed (thick line). (b) Reconstructed track position with respect to the nominal wire position vs. time for a single plane.

The tracking efficiency for a single plane averaged both over all wires and the wires length is varying between 81% and 84%. It is determined as the ratio of the number of reconstructed tracks having a (registered) hit in the layer not farther than 5 mm apart from the track crossing, to the total number of reconstructed tracks passing the plane within its acceptance. So, accounting for the ratio of the inner diameter (29 mm) of the tube to the pitch (33.5 mm), a value of 83 % corresponds to 96% drift tube efficiency.

4.4.6 Calorimetry

Two hadron calorimeters and one electromagnetic calorimeter are used in COMPASS setup (see Fig. 4.1) in 2004. One electromagnetic calorimeter was added later. Both hadron calorimeters are sampling calorimeters using stacks of iron and scintillator plates. They are located before the muon filters. Both hadron calorimeters serve a double purpose in the experiment. They measure the energy of hadrons produced in the target and participate in triggering. ECAL2 is a homogeneous calorimeter consisting of lead glass blocks located before HCAL2. It serves to measure the energy of electromagnetic showers. In addition it was used in the trigger for the measurement of Primakoff reactions with the pion beam.

Electromagnetic Calorimeter ECAL2

The electromagnetic calorimeter ECAL2 in the SAS part of the COMPASS spectrometer consists of 2972 (a matrix of 64×48) lead glass modules with $38 \times 38 \times 450\,\mathrm{mm}^3$ dimensions amounting to 16 radiation lengths that were previously used in the GAMS-4000 spectrometer [66, 67]. A high energy photon (or electron) coming to the ECAL2 produces an electromagnetic shower inside the lead glass. The electrons and positrons from a shower emit Cherenkov light on their way through the glass. The amount of Cherenkov light is proportional to the energy deposited in each counter. Each lead glass block is viewed at one end by a PMT which measures the intensity of the light emitted at that counter.

The modules are installed inside a frame, which can be moved vertically and horizontally by 2.5 m for calibration and maintenance. The ECAL2 platform can be moved on rails along beam axis. A hole of 10×10 modules in the centre allows passage of the beam particles. For pilot hadron run the hole size was reduced to 2×2 modules. Two types of lead glasses, TF1 (SF2 class) and TF101 (radiation-hardened by adding 0.2% of cerium), are used in the detector. The radiation-hardened modules (approximately 800) are placed around the central hole. They can tolerate a dose of a few krad [68] (see Fig.4.8).

A lead glass module is shown in Fig. 4.9. The accuracy of the transverse dimension is 0.05 mm. A plastic cylinder enclosing the PMT is glued with epoxy to one end of the glass prism. The PMT is wrapped into three layers of permalloy of 0.1 mm thickness. It is pressed to the glass by an elastic plate. The optical contact with the radiator is made through silicon grease. The lead glass radiator is wrapped in aluminized mylar. The aluminized side of the mylar is protected with special varnish, which prevents destruction of the reflecting layer and diffusion of aluminium atoms into the glass. The FEU-84-3 PMT with a trialkaline photocathode of S-20 type, 34 mm in diameter, has been chosen for the counters. About 1000 photoelectrons per GeV energy deposit are obtained.

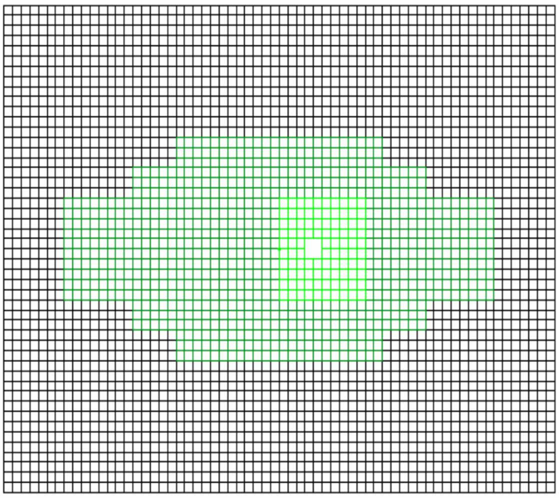

Figure 4.8: ECAL2 layout. TF101 modules are shown in dark green. TF101 modules added to reduce size of the beam hole fore pilot hadron run are shown in light green.

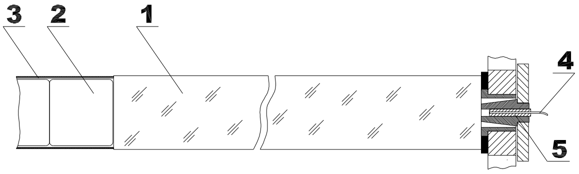

Figure 4.9: A modul of the ECAL2 calorimeter: 1) TF1-000 lead glass radiator, 2) FEU-84-3 PMT, 3) permalloy magnetic screen, 4) quartz fibre to distribute the light pulse of the monitoring system, 5) light guide connector.

Special high voltage dividers have been designed in order to obtain a maximum range of linearity. The divider and the electronics of the computer controlled high voltage supply are described in [69]. For gain monitoring purposes, light pulses produced by a group of LEDs are delivered by a 2 m quartz fibre to the front of each counter. The anode signals of all counters are measured by two types of analogue-to-digital converters, FIADC and SADC. The calibration of ECAL2 is carried out at the COMPASS experiment with the 40 GeV electron beam and repeated for each data taking period. The whole calorimeter is moved to expose all modules to the beam and a few thousand events for each module are collected.

The resolutions and linearity were measured previously [66, 67, 70]. Obtained energy and space resolution are:

$$\sigma(E)/E = 5.5\%/\sqrt{E} \oplus 1.5\%, \tag{4.2}$$

$$\sigma(x) = 6\,\mathrm{mm}/\sqrt{E} \oplus 0.5\,\mathrm{mm}, \tag{4.3}$$

where E is the energy in units of GeV. For the central part of ECAL2 consisting of the radiation-hardened modules energy and space resolution is rather worse. The linearity was better than 1% in the energy range from 0.5 to 40 GeV.

Hadron calorimeter HCAL2

The hadron calorimeter HCAL2 is a matrix of 22 × 10 modules, arranged on a mobile platform. The basic modules are sandwich counters with $20 \times 20\,\mathrm{cm}^2$ transverse dimensions. The calorimeter has a beam hole with the dimensions of 2 × 2 Two types of modules are used in the detector. Most of them consist of thirty six 25 mm thick steel plates, interleaved with 5 mm thick scintillator sheets. The modules were previously used in the NA12 experiment, but the method of light collection from the scintillators and the HV bases for the PMs were modified. The overall thickness of the counters is 5 nuclear interaction lengths (λ_I) for pions and 7 for protons. The central 8 × 6 cells are filled with thicker modules consisting of 40 layers.

The principle of the light collection from the scintillator sheets is presented in Fig. 4.10. The readout of the scintillation light is done using wavelength shifting fibres of 1 mm diameter placed in a circular groove in each scintillator sheet. The bundle of fibres from all sheets collects the light onto the S-20 type photocathode of a FEU-84-3 PMT. All scintillator fibre pairs were tested with a radioactive source and sorted to equalize the module light output. A silicon compound provides the optical contact between the bundle of fibres and the PMT. The computer controlled HV divider is of Cockcroft-Walton type. The PMT signals are measured with the specially designed 12-bit fast analogue-to-digital converters. Small fraction of the signals is fed into the fast summation system for trigger purposes. The timing spread of the signals from different PMTs is compensated with pieces of coaxial cables.

The calorimeter has a light monitoring system common for all modules using a light pulse from a group of light emitting diodes fed to the PMs through fibre light guides. The monitoring system is used for amplification adjustment and control.

As for the characteristics of the HCAL2 modules were determined at the test beam using a matrix of 5×5 modules. HCAL2 has good linearity in the range from 10 to 100 GeV, the energy resolution is

$$\sigma(E)/E = (66/\sqrt{E} \oplus 5)\,\%, \tag{4.4}$$

where energy E is in units of GeV (see Fig. 4.11). The uniformity of the calorimeter response was checked by scanning the test beam across the surface of the test setup. It was found to be better than 2%.

4.4.7 Setup for measurements with hadron beam in 2004

Several modifications were applied in order to adapt the setup to the measurements with hadron beam. The large polarized target system was removed and replaced by a solid target holder, surrounded by a barrel shaped detector designed to measure low energy target fragments. This detector consists of scintillating counters inside an electromagnetic calorimeter. Two sandwiches of scintillating counters and lead foils were used to veto on photons and charged particles emitted at large angles. Two silicon microstrip telescopes were installed, with two and three stations upstream and downstream of the target, respectively, providing high angular resolution. The multiplicity information from the second telescope was used online at the event filter level. Scattering off materials along the beam path was minimized by removing the

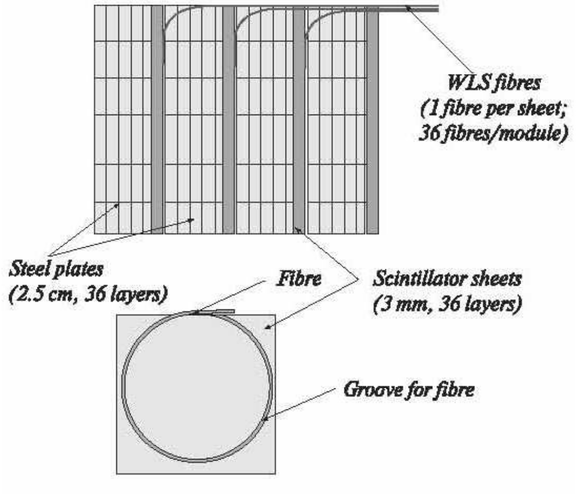

Figure 4.10: Principle of the fibre light readout of HCAL2, top: side view of part of a module, bottom: front view of a scintillator plate with the fibre readout.

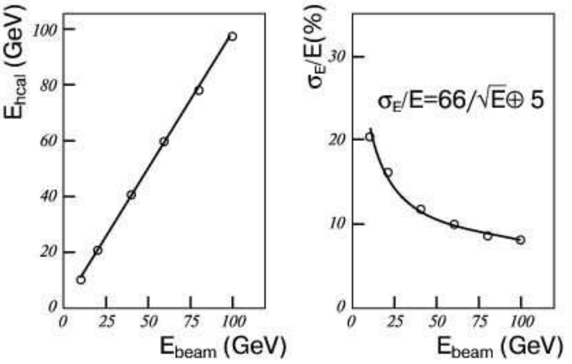

Figure 4.11: Energy deposition in HCAL2 (left) and energy resolution (right) as a function of the beam energy.

BMS and one of the scintillating fibre stations upstream of the target. For the same reason, three out of the six scintillating fibre stations downstream of the target were also removed. The size of the electromagnetic calorimeter central hole was reduced in order to fit the hadron beam size. Finally, the trigger on scattered pions was provided by a dedicated scintillator hodoscope.

4.4.8 Beams

The CERN SPS beam line M2 can be tuned for either high-intensity positive muon beams up to 190 GeV/c or high-intensity hadron (mainly proton or mainly pion, positive or negative) beams up to 280 GeV/c. Negative muon beams are also available, although with lower intensities. On request a low-energy, low-intensity tertiary electron beam can be used for test and calibration purposes.

The muon beam is derived from a very intense primary proton beam, extracted from the CERN SPS at 400 GeV/c momentum, that impinges on a beryllium target with 500 mm thickness (T6). Thinner targets can be selected for lower flux, if required. The nominal proton flux available for COMPASS is $1.2 \cdot 10^{13}$ protons during 4.8 s long spills, within a 16.8 s long SPS cycle. A section of six acceptance quadrupoles and a set of three dipoles selects a high pion flux within a momentum band of up to ±10% around a nominal momentum up to 225 GeV/c and within a geometrical acceptance of about $3\pi\,\mu$sr. At the production target the pion flux has a kaon contamination of about 3.6%. The pions are transported along a 600 m long channel, consisting of regularly spaced alternately focusing and defocusing (FODO) quadrupoles with a phase advance of 60° per cell. Along this channel a fraction of the pions decay into a muon and a neutrino. Both pions and a large fraction of the muons produced in the decays are transported until the muons are focused on and the hadrons are stopped in a hadron absorber made of 9 motorized modules of beryllium, 1.1 m long each.

The hadron absorber is located inside the aperture of a series of 3 dipole magnets, providing an upward deflection of 4.8 mrad each. These dipoles are followed by a fourth magnet, providing an additional deflection of 9.6 mrad, resulting in a total deflection of 24 mrad for a good momentum separation. The dipole section is followed by a series of acceptance quadrupoles for the muons. The accepted muon beam is subsequently cleaned and momentum selected by two horizontal and three vertical magnetic collimators. All the five collimators are toroids whose gap can be adjusted to match the profile of the useful beam. The muons are transported to the surface level by a second 250 m long FODO channel. Finally the muons are bent back onto a horizontal axis by three 5 meters long dipole magnets, surrounded by 4 hodoscopes and 2 scintillating fibres planes for momentum measurement, and focused onto the polarized target. The nominal momentum of the muon section of the beam is lower than the one of the hadron section, with a maximum of 190 GeV/c with a momentum spread usually between ±3% and ±5% RMS. Typically the muon momentum is chosen to be around 90%−94% of the central hadron momentum in order to provide the best compromise between muon flux and polarization. The final section of the beam comprises several additional bending and quadrupole magnets that fine-steer the beam on the target and, during transverse polarization data taking, compensate for the horizontal deflection induced by the 0.5 T transverse dipole field of the polarized target.

A high-intensity secondary hadron beam is obtained by moving the nine motorized hadron absorber modules out of the beam and loading settings cor-

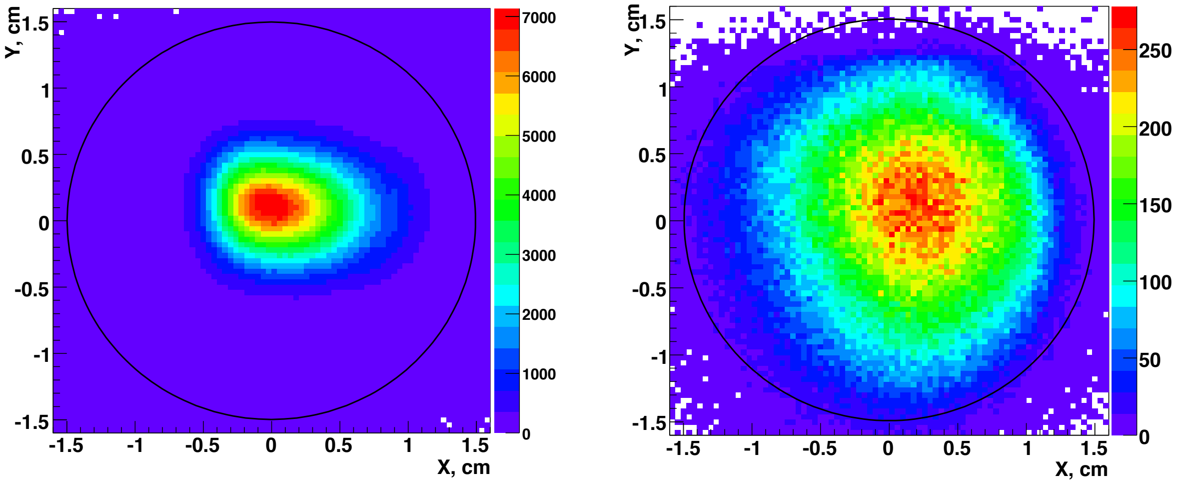

Figure 4.12: XY-profile of hadron (left) and muon (right) beams on the target. Target is shown by circle.

responding to a single momentum all along the beam line. Up to 225 GeV/c, the front end of the beam line is operated with the same optics as for the muon mode of the beam. At higher momenta a different optics is used in the acceptance quadrupoles, giving access to 280 GeV/c. The beam optics is optimised for momentum resolution. The beam is composed of a (momentum dependent) mixture of pions, protons and kaons. For the tagging of individual beam particles, a pair of differential Cherenkov counters [71] (CEDAR) is foreseen in the final section of the beam. The beam optics is optimized to provide a wide and parallel beam as required for the CEDAR counters, while delivering a relatively small beam spot at the COMPASS target in the experimental hall. The maximum allowed hadron flux is 10^8 particles per SPS cycle, limited by radiation safety rules assuming less than 20% interaction length material along the beam path.

On request a 40 GeV/c tertiary electron beam can be provided by selecting a 100 GeV/c negative secondary beam, which impinges on a 5 mm thick lead converter, located about 50 m upstream of the hadron absorbers, which are moved out of the beam for this purpose. The downstream part of the beam line is set to 40 GeV/c negative particles, so that only the electrons that have lost 60 GeV due to bremsstrahlung in the converter are transported to the experiment. The electron flux is typically small, of a few thousands per SPS cycle. In COMPASS the electron beam is used for an absolute calibration of the electromagnetic calorimeters.

Table 4.2: The parameters of the hadron and muon beams used during pilot hadron run 2004.

	P,GeV/c	ΔP/P,%	σ_x, mm	σ_y, mm	θ_{zx}, mrad	θ_{zy}, mrad
π^-	190	0.77	5	4	0.1	0.2
μ^-	190	4	6	7	0.4	0.6

Table 4.3: Composition of the 190 GeV hadron beam.

Particle	Fraction,%
π^-	93.5
K^-	3
μ^-	3
p^-	0.5
e^-	~0.1

For Primakoff reaction study 190 GeV/c pion and muon beams were used. Such parameters of the beams like beam momentum spread, beam size and beam divergency are presented in Tab. 4.2. Tab. 4.3 shows contamination of other particles in the pion beam. Fig. 4.12 illustrates XY-profiles of hadron and muon beam on he target. CEDAR during pilot hadron run was operated in testing mode so the identification of beam particles was absent.

4.4.9 Targets

The majority of the 2004 hadron data has been collected with a target optimized for Primakoff scattering study. Since this process is enhanced over the diffractive background when targets with large atomic numbers are used, lead was chosen as material. To study systematic effects, additional measurements of the Z^2-dependence of the Primakoff cross section using copper and carbon were performed (see Table 4.4). All targets consisted of simple discs with a diameter of 3 cm, corresponding to more than 3 RMS of the hadron beam width, while the thickness was determined by the required resolution to properly separate the electromagnetic scattering from the diffractive background.

Table 4.4: Atomic and nuclear properties of the targets used during the COMPASS hadron run 2004.

Target	A	Z	$\rho, \frac{g}{cm^3}$	h, mm	h, X_0	h, λ_I
Pb	207.2	82	11.35	2+1	0.54	0.018
Pb	207.2	82	11.35	1.6	0.29	0.009
Pb	207.2	82	11.35	3.0	0.54	0.018
Cu	63.5	29	8.96	3.55	0.25	0.024
C	12	6	2.2	23.5	0.12	0.060

In order to reject the hard scattering events in the offline analysis, the targets were inserted into a barrel-shaped veto system, called recoil veto, that measured the recoil energy of the target fragments produced in the reaction.

4.4.10 Primakoff trigger

During the 2004 hadron run two different trigger systems have been implemented, one designed to select Primakoff scattering events, and the second to select diffractive η-meson production. The two systems shared a common set of devices that select beam particles pointing to the target and reject events with particles emitted outside the apparatus acceptance. In addition, some specific trigger components were used to select the typical event topologies of Primakoff and diffractive scattering.

Beam particles were detected by the coincidence of two scintillator counters, with a diameter of about 5 cm, centered on the beam trajectory. The veto counter with a central hole of about 4 cm in diameter, placed upstream of the recoil veto, was used to reject beam particles not crossing the target material (see Fig. 4.13).

Two additional veto counters made of lead-scintillator sandwiches and located downstream of the recoil veto, were used to reject events with charged particles or photons emitted at large angles and falling outside the acceptance of the electromagnetic and hadronic calorimeters. This condition is needed to precisely define the exclusivity of the reaction in the offline analysis.

Non-interacting beam particles were rejected by means of a system of three small plastic scintillators (beam killers), with a diameter of 5 cm and a thickness of 5 mm, centered on the beam trajectory and placed between the SM2 magnet and the ECAL2 calorimeter. The signal of the beam counters was used in anti-coincidence with the sandwich vetos and the beam killer 3, to form the common part of the trigger logic (common trigger). This information is combined with that of the dedicated trigger devices for Primakoff and diffractive scattering to produce the first level trigger for the COMPASS DAQ.

In order to cover the energy range $0.25 < \omega < 0.9$ of the emitted photons two different Primakoff triggers have been implemented, called $Primakoff$ 1 and $Primakoff$ 2.

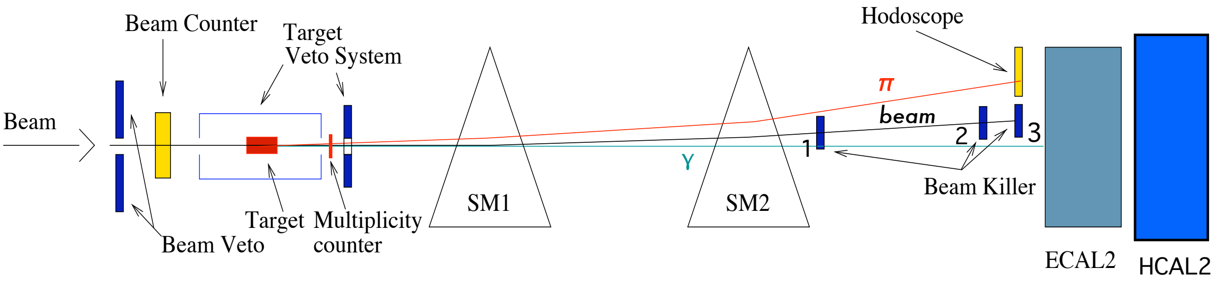

Figure 4.13: Schematic view of the Primakoff trigger.

In the $Primakoff$ 1 trigger the scattered pion is detected by means of a scintillator hodoscope located in front of the ECAL2 electromagnetic calorimeter. The hodoscope is composed of 20 slabs of $6 \times 90\,\text{cm}^2$ in size and is able to detect pions in the energy range $20 - 110$ GeV. Additionally, an energy deposit larger than $\sim$ 40 GeV in ECAL2 is required. The $Primakoff$ 1 signal is then made by the coincidence of the common trigger, the scattered pion hodoscope, the ECAL2 signal, and in addition an energy deposit above $\sim$ 18 GeV in HCAL2.

Events with very high photon energies were selected by the $Primakoff$ 2 trigger. In this second case, the scattered pion hodoscope is excluded from the logic and an higher energy threshold of 90 GeV is applied to the summed ECAL2 signal. The overall Primakoff trigger is then produced by the logical or of the $Primakoff$ 1 and $Primakoff$ 2 signals.

Typical trigger rates of about $5.8 \cdot 10^4$/spill for $Primakoff$ 1 and $3.8 \cdot$

10^4/spill for $Primakoff$ 2 have been obtained. Due to the overlap in the kinematical region covered by the two triggers, about 20% of the Primakoff events fulfilled both trigger conditions, leading to an overall Primakoff trigger rate of about $7 \cdot 10^4$/spill.

4.5 Event reconstruction and spectrometer performance

4.5.1 Monte Carlo simulation of the experimental apparatus

A general interface to Geant 3.21 [76], called COMGEANT, has been developed in order to simulate the performance of the COMPASS spectrometer. COMGEANT can be linked to any standard generator of lepton, photon or hadron interactions such as LEPTO [77], or Pythia [78] or to specialized generators for particular processes like POLARIS [87] for Primakoff reaction.

For the muon beam, the track parameters used to generate beam and halo particles are extracted from the real data events recorded with randomly generated triggers. In the case of beam particles, the parameters are taken from the tracks reconstructed in the BMS, SciFis and Silicon trackers. The parameters of the near halo component are extracted from halo tracks reconstructed along the spectrometer. For the far halo particles, falling outside of the spectrometer acceptance, the momentum is assigned using a parameterization taken from the Monte Carlo simulation of the beam line. A similar approach is used for the simulation of the hadron beams.

Interactions are generated randomly inside the target volume and secondary tracks propagated through the spectrometer. Special care was devoted to the realistic description of the regions of the spectrometer with high material densities, through the use of material maps that describe the type and amount of material of each of the spectrometer elements. The maps consist of three dimensional grids with variable cell size, depending on the homogeneity of the material being considered. The relevant properties (radiation length, density) are stored for every cell. Material maps are defined around the target, between the target and SM1, between SM1 and the RICH, for RICH itself and for both muon filter regions. These maps take into account all materials introduced into the spectrometer acceptance including detector frames, support structures and hadron absorbers.

For detector response simulation two basic quantities are used, efficiency and resolution. In case of specific types of detectors like GEMs, Calorimeters and RICH photon detectors, space and amplitude distributions of the signals are also simulated. All detector properties introduced in the simulation have been tuned using real data samples.

4.5.2 COMPASS data production and analysis software

The software used by COMPASS for the event reconstruction is the internally-developed CORAL (COmpass Reconstruction and AnaLysis) toolkit. CORAL is a fully object-oriented program with a modular architecture, written in C++. The schematic representation of the reconstruction process by CORAL is shown in Fig. 4.14 CORAL has two different modes: the first one is reconstruction of the events from raw data collected by the experiment (real data), the second one is reconstruction from Monte-Carlo simulated data, prepared by COMGEANT. In the case of real data the first phase for the event reconstruction is the **decoding** process when the information on the fired detector channel (either wire, pad, or cell, depending on the detector type) is extracted from the raw data. In the second phase, called **clustering**, detector channels that are fired by the same particle are grouped together. For some detectors weighted centre-of-gravity algorithms are applied to get a better determination of the particle parameters. During the clusterization phase, the information on the geometrical position of each detector in space is used to calculate the coordinate of the cluster in the main reference system of the apparatus. The geometrical position of each detector plane is retrieved from files that are generated either by the alignment procedure or by the Monte Carlo package. The clusters are then pre-selected on the basis of the time information.

When Monte Carlo data files are processed, the decoding phase is replaced by a **digitization** phase, in which the response of the detector is simulated and hits are produced on the basis of the particle trajectory and detector resolution.

After clusterization, charged and neutral particles are reconstructed and particle identification is performed. The information from tracking detectors is used to reconstruct the trajectories of the charged particles through the spectrometer and to determine their momenta. Hadron calorimeter clusters are used to separate muons and hadrons; electromagnetic calorimeter clusters measure the energy and impact coordinate of photons and electrons. Hadron identification is performed by the RICH.

A vertex finding procedure is applied to all reconstructed tracks, in order to identify the primary interaction point and subsequent decays of neutral particles.

The result of the reconstruction phase (track parameters, vertices, calorimeter clusters, PID probabilities, detector hit patterns, etc.) is stored into output ROOT [79] trees, called mini Data Summary Tapes (mDST), that are distributed to home computing centers and serve as input for all the physics data analyses. The data reduction factor between the input raw data and the output mDSTs is about 100. Large DST files, storing the detector digits and clusters in addition to the tracking, vertex, and PID information are also created and kept at CERN on tape.

For the data analysis purposes the PHAST (PHysics Analysis Software Tools) [80] internally-developed software is used. The program consists of various classes and ROOT-based routines using which user can:

1. access to reconstructed events information stored in mDSTs,
2. develop his own analysis code to apply cuts, fill and plot histograms.. etc.,
3. process new mDSTs containing filtered sub-samples of input mDSTs.

All analysis described in this work has been performed using PHAST.

4.5.3 Track and momentum reconstruction

The track reconstruction algorithm (TRAFFIC/TRAFDIC) is divided into three phases corresponding to pattern recognition (i.e. finding track segments in the various zones of the spectrometer), bridging (i.e. connecting track segments from several distinct zones to build full tracks), and fitting (i.e. computing the best estimators for the parameters of the reconstructed tracks).

The **pattern recognition** selects sets of clusters consistent with track segments. To that end, the spectrometer is divided into 5 zones along the beam, where track segments are expected to follow approximately straight lines. The five zones comprise the regions upstream of the target, from target to SM1, from SM1 to SM2, from SM2 to the second muon filter, and downstream of the second muon filter.

Reconstruction is first performed in **projections**. For this purpose the detector planes in each zone are divided into groups having the same orientation, thus measuring the same projection of a track. A pivot-plane algorithm is used to search for track segments in these projections. In this approach, each pair of detector planes is used successively as a pair of pivots. Each pair of clusters from the pivot planes is used to define a straight road, thus associating clusters from all other planes. At each successively encountered detector, the road width is adjusted to take into account the detector resolution. This projection search is performed for each projection. A pre-selection of candidate track projections is then performed, based on the number of clusters, and taking into account its variation as a function of the track angle.

In the next step, all projections are combined to produce **space track segments**. The search combines track segments taken from pairs of projections to open a road in space; clusters from all detectors in all projections are then collected within this road. For each detection plane, the position corresponding to the measured coordinate is assigned to the cluster, and a check whether the track impact point is within the sensitive area of the corresponding detector is performed. All track candidates are then compared to a dictionary of possible tracks through the COMPASS spectrometer. This dictionary is organized as a look-up table, thus increasing the speed of the fitting procedure.

The building of full tracks out of the track segments found in the preceding phase proceeds sequentially, first via straight line fit, and then via **bridging** (connecting track segments) of two adjacent zones. The successfully combined track segments are then ordered according to a quality function (QF) based on the χ^2 and the number of hits associated to the track. The combination with the best QF is retained, while combinations re-using one of the previously accepted segments are discarded. The process is iterated until the list is exhausted.

In the final phase of the tracking algorithm, magnetic fields and material maps are used to get the best estimates of the track parameters (x and y positions, $\mathrm{d}x/\mathrm{d}z$ and $\mathrm{d}y/\mathrm{d}z$ slopes, inverse momentum $1/p$) and their error matrix. For this purpose, the **Kalman fit** method is used [72, 73]. The fit starts from the first cluster of the found track. The track parameters are updated by this measurement and propagated to the next detector surface. This process is repeated for all clusters belonging to the track. The Kalman fit is performed twice, first in the downstream and then in the upstream direction, in order to provide the track parameters at the first and last measured point of the track.

Apart from spatial measurements (cluster coordinates), a number of COMPASS detectors also provide time information (**cluster time**) with respect to the time of the trigger signal. As those measurements are completely independent from coordinate measurements, the time component is not included in the track parameterization but a weighted mean time is calculated separately. This track time information is important for rejection of pile-up tracks, beam momentum determination, trigger system performance studies, etc.

4.5.4 Alignment procedure

The alignment procedure determines the detector positions in space by minimizing the χ^2 of all tracks simultaneously. Initially tracks are reconstructed using detector positions determined by a geometrical survey. The minimization of the χ^2 is based on the analytical inversion of a huge sparse matrix, using the Millipede program described in [74]. The optimized parameters are:

- the position of the detector centre,
- the rotation between the detector coordinate system and the global coordinate system,

- the effective detector pitch, i.e. the distance between adjoining wires or pads.

The procedure is iterated until the changes in the detector positions become negligible compared to their resolution.

The adjustment of detector parameters is first done using data samples, collected with the spectrometer magnets switched off, so that straight trajectories through the spectrometer can be assumed, and then refined using standard data. The alignment procedure is repeated after each long interruption of the data taking and each time some detector has been moved.

4.5.5 Vertex reconstruction

The last phase in the event reconstruction is the location in space of the primary interaction or of the two-body decays of neutral particles (so-called V^0 vertices). Here the aim is to get the best estimate of the three coordinates of the vertex position from which each track is assumed to originate, of the three components of the momentum vector of each track at this vertex, and the corresponding covariance matrices.

A first approximation of the primary vertex is obtained by computing the average Point Of Closest Approach (POCA) between one beam track and all possible outgoing tracks. All tracks having a POCA too far from the approximated vertex position are discarded; an exception is represented by the scattered muon, which, if present, cannot be removed from the vertex.

A vertex is called primary when it contains a beam track. Since more than one beam track can exist for one event, as many primary vertices as the number of existing beam tracks can be reconstructed in this phase; the selection of the best vertex is performed later at the level of physics data analysis.

The tracks surviving the initial selection are used to perform the fit of the vertex position by an inverse Kalman filter algorithm. During the first iteration, all tracks are used to estimate the parameters of the vertex, and the relative χ^2 contribution of each track to the fit is computed. If the largest χ^2 contribution exceeds a threshold value, the corresponding track is removed from the list and the procedure is iterated once more. However, neither the reconstructed beam track nor the scattered muon track can be removed from the vertex. The algorithm stops when all remaining tracks survive the χ^2 selection.

The procedure described above may fail if the initial list of tracks contains a large number of fake tracks. In such a case the initial vertex position may be estimated to be too far from the real one, resulting in a rejection of the good tracks. In order to avoid this difficulty, a recovery procedure is applied at the end of the vertex fit phase. The unassigned tracks are re-inserted in the list one by one, and the vertex fit is re-calculated each time. A track surviving the χ^2 selection is then finally re-assigned to the vertex. The recovery phase ends when all unassigned tracks have been checked.

The distribution of reconstructed primary vertices along the beam axis, for events with one outgoing particle in a primary vertex (see Fig. 4.15), shows clearly the structure of the 2+1 mm Pb target. Vertices with scattering angle θ between 2 and 4 mrad, reconstructed outside the target, correspond to the beam kaons decay. Resolution for z-vertex position strongly depends on the production angle of secondary particles. In the case of one outgoing particle it can be expressed as (see Fig. 4.16):

$$\sigma_z = (5 + 30/\theta)\ mm. \tag{4.5}$$

In the direction perpendicular to the beam axis, the primary vertex coordinates are determined by the Kalman filter with an accuracy of $\leq 0.5\,\mathrm{mm}$.

Secondary vertices are reconstructed in the target region so that nearly all K^0_S, Λ and $\overline{\Lambda}$ decays into charged particles are observable. The V^0 vertices are searched by combining all pairs of tracks with opposite charge, regardless of their association to the primary vertex. The most probable decay position, the track parameters at the vertex and the corresponding error matrices are calculated using the Kalman filter technique. For decays occurring downstream of the target, the mass resolution is found to be $7.6\,\mathrm{MeV}/c^2$ for the K^0_S and $2.5\,\mathrm{MeV}/c^2$ for the Λ and $\overline{\Lambda}$ (see Fig. 4.17).

4.5.6 Track reconstruction efficiency and accuracy

The reconstruction efficiency is defined as the fraction of Monte-Carlo generated tracks within the spectrometer acceptance which are reconstructed

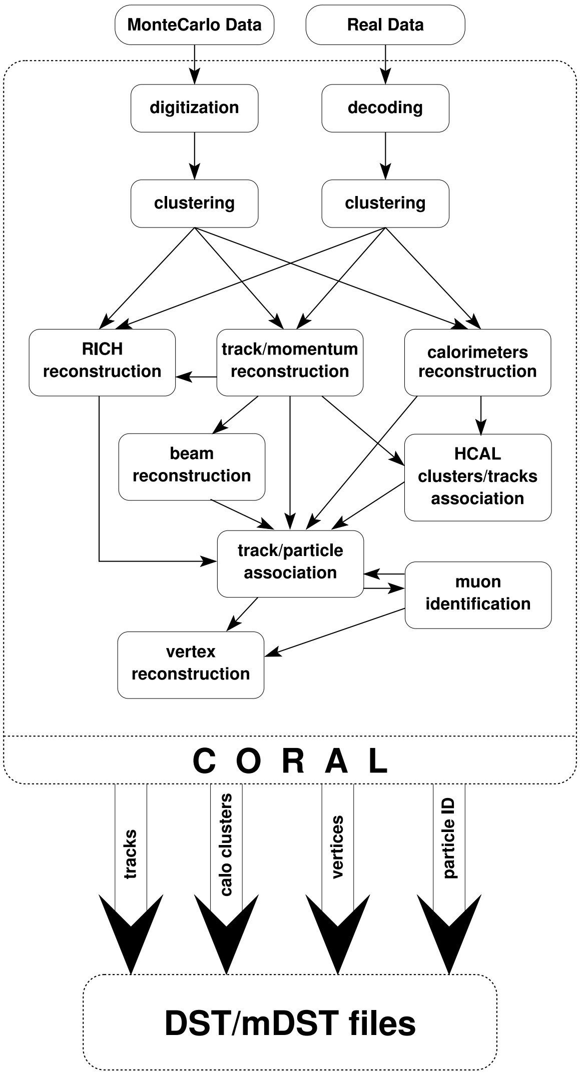

Figure 4.14: Schematic representation of the COMPASS reconstruction software.

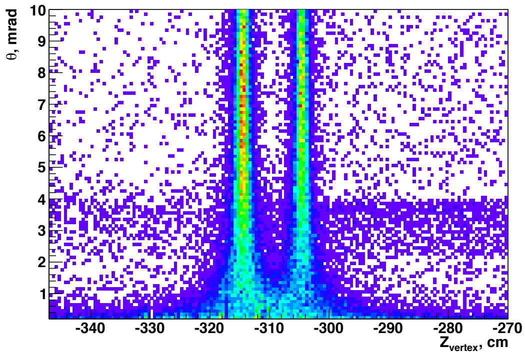

Figure 4.15: Distribution of the reconstructed vertex position z along the beam axis for vertexes with one outgoing track as a function of the angle between incoming and outgoing tracks.

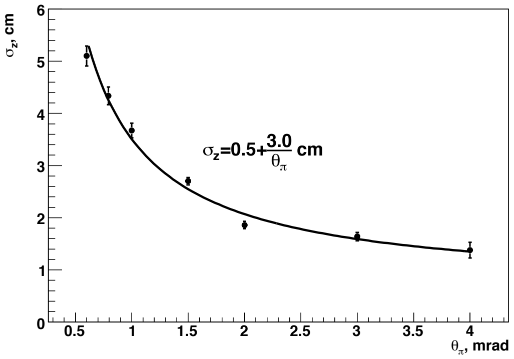

Figure 4.16: Resolution for z-vertex position for vertices with one outgoing track as a function of the angle between incoming and outgoing tracks.

by the tracking package. The reconstruction efficiency for tracks produced at a primary interaction point as a function of the particle momentum is shown in Fig 4.18. It is independent of the particle type, and found to be larger than 90% for $P > 5$ GeV/c but drops rapidly for lower momenta.

The accuracy of the tracking is evaluated by comparing the track parameters resulting from the Kalman fit on the reconstructed Monte Carlo tracks with the corresponding values from the generated tracks. For the tracks measured in silicon detectors the average errors on the track position in the transverse plane are of the order of $10\,\mu$m at the z-coordinate of the first

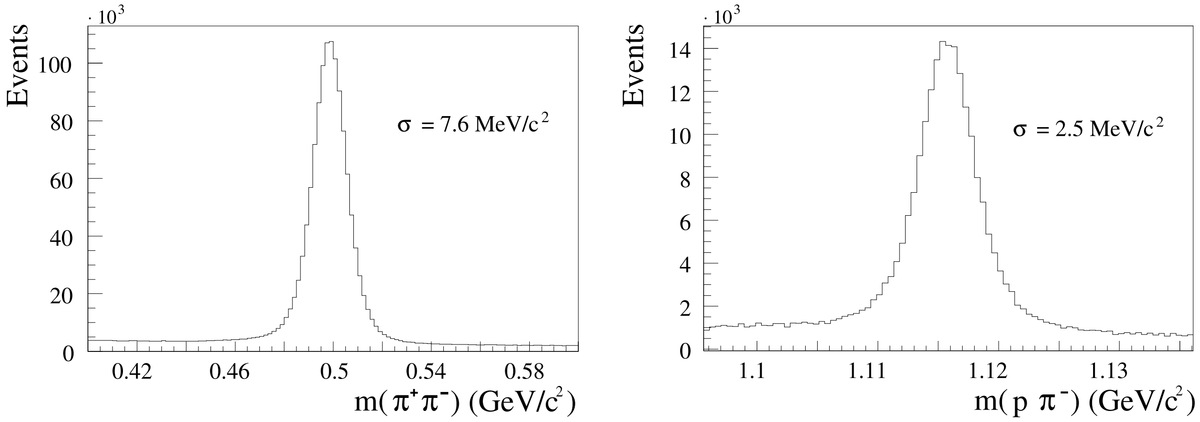

Figure 4.17: Reconstructed invariant mass of V^0 decays, in the hypothesis of $\pi^+\pi^-$ decay (top) or $p\pi^-$ decay (bottom), respectively.

detector, in agreement with the nominal resolution. The relative momentum resolution and the track reconstruction efficiency are shown in Figs. 4.18, 4.19 as a functions of the particle momentum. The relative error σ_P/P is about 0.5% for tracks reconstructed in both spectrometers ($p \geq 5\,\mathrm{GeV}/c$).

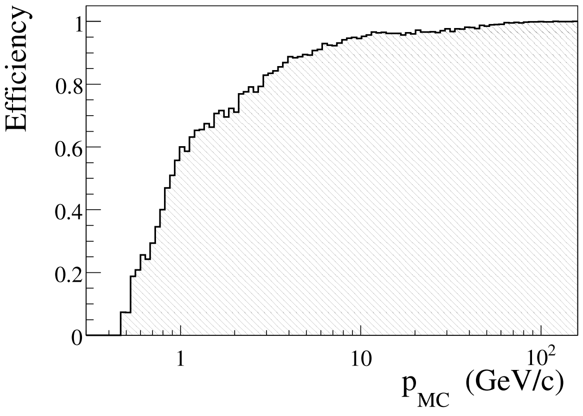

Figure 4.18: Reconstruction efficiency as a function of the particle momentum.

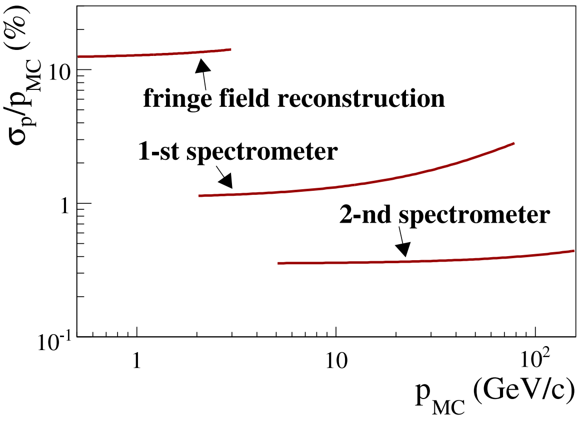

Figure 4.19: Track momentum resolution as a function of the particle momentum.

4.5.7 Energy reconstruction in the COMPASS calorimeters

In 2004 at COMPASS, the energies of charged and neutral particles are reconstructed by means of two hadron calorimeters HCAL1, HCAL2, and one electromagnetic calorimeter ECAL2. The energies and positions of the calorimeter showers are reconstructed by a dedicated software package, common to both types of calorimeters. The shower parameters are estimated from the energy deposited in clusters of neighbor cells, assuming a known parameterization of the shower profile.

During the first step of the shower reconstruction, the local maxima are approximately identified by selecting the cells with an energy deposit above a predefined threshold. At this stage, two showers are not separated if the local maxima are located at nearby cells.

The energy and position of the cell corresponding to the local maximum are used as initial parameters for the shower reconstruction. The remaining part of the shower is searched in a region of 3×3 or 5×5 cells surrounding the local maxima. The region size depends on the estimated shower energy; for higher energies a larger region is selected. Although a local maximum can be attributed to one shower only, the energy deposited in the surrounding cells can be shared between two or more showers. Therefore, the initial values of energy and position for the shower are used to estimate the amount of energy deposited in the cells surrounding the local maximum. This procedure is repeated for all local maxima; the relative contribution of each shower to the shared cells is thus computed.

Once the amount of energy deposited in each cell by the expected showers is computed, a fitting procedure is applied to calculate the exact parameters (energy and position). The energy is simply calculated from the sum of cell energies, corrected for the shower leaks outside the calorimeter and for the shower overlaps. For the determination of the coordinate parameters, the inverse one-dimensional cumulative shower profile function [75] is used. In this approach, the theoretical two-dimensional shower surface is projected onto two planes, perpendicular to the calorimeter surface, one directed horizontally and one vertically. The projection of the shower surface is symmetric with respect to the shower axis, and the two boundaries are parameterized with analytical functions, the actual parameters of which are optimized for the hadron and electromagnetic cases. The position of the shower axis which gives the best fit to the energy distribution in the cells attributed to the shower determines the X and Y coordinates, depending on the projection surface.

Spatial resolution of the ECAL2 can be tested using the COMPASS tracking system. Calorimeter clusters associated with tracks, for which the particle energy reconstructed by spectrometer, is approximately equals to the cluster energy, are treated as produced by electrons or positrons. For each electron and positron, identified by this way, the distance Δ between a reconstructed cluster position and an incidence point, calculated from track extrapolation to Z-plane of the calorimeter, can be calculated. The RMS of Δ-distribution is contributed by an uncertainty of track reconstruction σ_{tr} (known from the tracking procedure) and spatial resolution of ECAL2 $\sigma_{x,y}$. So, coordinate resolution can be estimated as:

$$\sigma_{x,y} = \sqrt{RMS^2_{\Delta x,y} - \sigma^2_{x,y\ tr}}. \tag{4.6}$$

Resolution of the ECAL2 for Y-coordinate as function of electron energy is shown in Fig. 4.20.

A good estimation of the overall ECAL2 performances is given by the mass resolution for reconstructed $\eta \to \gamma\gamma$ decays. To estimate the width of the η mass peak and minimize the combinatorial background, only events with exactly two clusters originating from neutral particles have been selected. The invariant mass is then calculated under the assumption that the two clusters were produced by two photons emitted from the reconstructed primary interaction vertex. The resulting mass distribution is shown in Fig. 4.21. The fit of the mass peak with a gaussian function and a polynomial background gives a relative resolution of 4.6%, quite close to the theoretical limit of about 4% given by the intrinsic energy resolution of the calorimeter elements.

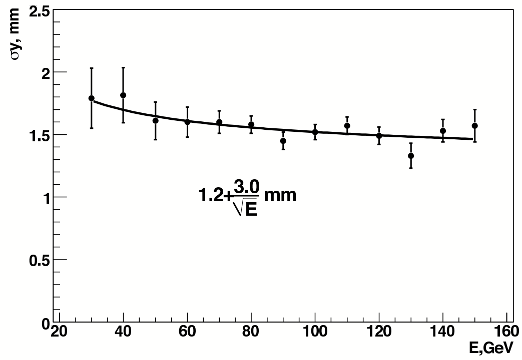

Figure 4.20: Resolution of the ECAL2 for Y-coordinate as function of the energy of electron.

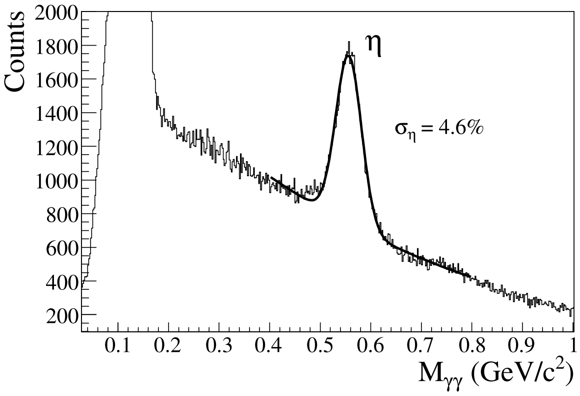

Figure 4.21: Invariant mass distribution in the hypothesis of 2γ neutral decays. The η mass is determined from the gamma energy reconstructed in the electromagnetic calorimeter ECAL2

Table 4.5: Comparison of SIGMA-AYAKS and COMPASS spectrometers.

	SIGMA-AYAKS	COMPASS 2004
Beam particles	π^-	π^-, μ^-
Beam momentum, GeV/c	40	190
Composition of the hadrom beam,%		
π^-	95	93.5
K^-	2.1	3
μ^-	2.5	3
p^-	0.3	0.5
e^-	0.1	~ 0.1
Beam intensity, s^{-1}	10^6	$10^6(\pi),\ 4 \times 10^6(\mu)$
Beam momentum spread, %	2.5	$0.7(\pi)$, $4(\mu)$
Main target, X/X_0	0.25(C)	0.5(Pb)
Other targets	Be, Al, Fe, Cu, Pb	C, Cu
Resolution for the vertex position, mm		
X,Y	-	0.5
Z	-	$5{+}30/\theta_\pi$
Resolution for scatt. pion momentum, %	1	0.3-0.4
Resolution for angle of incoming and scattering pion, mrad	0.12	0.01
Resolution for photon angle, mrad	0.12	0.06
Resolution for photon energy, %	3.5 for 26.6 GeV	5 for $> 100\ GeV$
Resolution for $Q,\ MeV/c$	12	18
Resolution for E_{tot}, %	5	3
Double photon resolution, mrad	-	1.5
Primakoff trigger rates, kHz	~ 0.01	10 (Primakoff 1) 7 (Primakoff 2)
Total beam flux	1.2×10^{11}	$10^{11}(\pi)$, $7 \times 10^{10}(\mu)$
Collected statistics $(0.5 < \omega < 0.9)$	6×10^3	3×10^4

Chapter 5

Primakoff reaction study during the pilot hadron run 2004

5.1 Data taking for Primakoff studies in 2004

The possibilities of the Primakoff reaction studies at COMPASS were estimated using the data collected with the 190 GeV/c π^- beam and Pb target of 3 mm, 2+1 mm ($0.5X_0$) and 1.6 mm ($0.3X_0$) thickness during the pilot hadron run [81]-[84]. Additional samples with Cu ($0.25X_0$), C ($0.12X_0$) and empty targets were used to study background processes and systematic errors. Sample with a 190 GeV/c μ^- beam and 2+1 mm Pb target was also collected for study of various systematic effects. The total beam flux collected with different targets with pion and muon beam is presented in Tab. 5.1. The period of data taking for Primakoff studies was about 2 weeks, but some time was spent to adjust the setup. Thus about 30% of statistics collected with Pb target in the beginning period of data taking was not suitable for further analysis. The period of stable data taking didn't exceed one week.

	Total flux
π^- on Pb target	1×10^{11}
π^- on Cu target	3×10^{9}
π^- on C target	4×10^{4}
π^- on empty target	3×10^{9}
μ^- on Pb target	7×10^{10}
μ^- on empty target	5×10^{9}

Table 5.1: Total beam flux used in 2004 for different targets.

5.2 Background processes study

There are few background reactions which have the same signature in COMPASS detector as the Primakoff reaction:

$$A^- \rightarrow B^- + ECAL2\ cluster(E > 7\ GeV), \tag{5.1}$$

where A^- is the beam particle, B^- is the scattered negatively charged particle and ECAL2 cluster is due to neutral particle.

Background processes can be classified into five groups:

1. Diffractive $\pi^- + Pb \rightarrow Pb + \pi^- + \gamma$ events. They typically have large Q^2 and can be effectively rejected by the Q^2 cut. One should also pay attention to the interference of the Primakoff and diffractive amplitudes.

2. Events with beam particles different from pion:

$$\begin{aligned} &\mu^- + Pb \rightarrow \mu^- + Pb + \gamma, \\ &e^- + Pb \rightarrow e^- + Pb + \gamma, \\ &p^- + Pb \rightarrow p^- + Pb + \gamma, \\ &K^- + Pb \rightarrow K^- + Pb + \gamma. \end{aligned}$$

   Because of the relatively big mass and small admixture in the hadron beam, the kaon and proton backgrounds are negligible. Beam muons and electrons are the most important sources of background.

3. Events with π^0, one soft decay photon of which was lost or two photons produced one cluster in ECAL2:

$$\begin{aligned} &\pi^- + Pb \rightarrow \pi^- + Pb + \pi^0 \rightarrow \pi^- + Pb + \gamma + \gamma\ (Primakoff), \\ &\pi^- + Pb \rightarrow \pi^- + Pb + \pi^0 \rightarrow \pi^- + Pb + \gamma + \gamma\ (diffractive), \\ &\pi^- + Pb \rightarrow \rho^- + Pb \rightarrow Pb + \pi^- + \pi^0 \rightarrow \pi^- + Pb + \gamma + \gamma, \\ &K^- \rightarrow \pi^- + \pi^0 \rightarrow \pi^- + \gamma + \gamma, \\ &K^- + Pb \rightarrow K^*(892) + Pb \rightarrow Pb + K^- + \pi^0 \rightarrow Pb + K^- + \gamma + \gamma. \end{aligned}$$

   These events can be rejected using the calorimeter information. Particularly, analyzing the cluster shape one can reject the events with two photons in one cluster. One can also recover the clusters of the lost soft photons analyzing the noise and pile-up clusters.

4. Double bremsstrahlung events $\pi^- \to \pi^- + \gamma + \gamma$ with double photon clusters or with one lost soft photon. Their contribution is taken into account in the radiative correction for Compton vertex.

5. Events with hard photon and soft lost π^0 in the final state:

$$\pi^- + Pb \to \rho^- + \gamma + Pb \to Pb + \pi^- + \pi^0 + \gamma.$$

   The cross section of such process is two orders of magnitude less than the cross section of ρ-meson production without photon emission.

Some background processes can be effectively suppressed by cuts on the kinematic variables, the contribution of other processes into the Primakoff sample can be estimated and subtracted. For another processes it is possible to estimate only the contribution to the systematic error of pion polarizabilities measurement (see Sec. 5.3).

5.3 Event selection

The main goal of this work was to study the possibility to estimate pion polarizabilities under assumption $\alpha_\pi + \beta_\pi = 0$ using the measured cross section $d\sigma/d\omega$. To achieve this goal one need to extract from the data the pure sample of Primakoff events in an ω-range where the cross section for point-like pion can be calculated using Monte Carlo simulation procedure. To do this the set of cuts was applied. Some cuts were applied to select event configuration corresponding to the configuration 5.1. Other cuts were applied against background processes mentioned above.

5.3.1 Trigger condition

Although Primakoff triggers cover a wide range of ω, only the events in the range $0.5 < \omega < 0.9$ with trigger $Primakoff$ 2 were used in the analysis. As the analysis has shown, the trigger $Primakoff$ 2 is simpler for understanding and for reproducing in the Monte Carlo simulation, efficient and covers the largest part of the kinematical region sensitive to polarizability effects. Trigger $Primakoff$ 1 was not so convenient for the analysis because it has a different structure for the muon and hadron beams and too complex for precise implementation in MC. Because of the strong overlap of the kinematical regions covered by the $Primakoff$ 1 and $Primakoff$ 2 triggers, the first was used only for study of the threshold shape of $Primakoff$ 2. The range $0.5 < \omega < 0.9$ was selected to be in the region of efficient identification of the scattered charged particles and to be far from the trigger threshold.

5.3.2 Tracks configuration

The candidate Primakoff events are selected with the following requirements:

1. existence of the beam track;
2. existence of only one primary vertex;
3. existence of only one track, reconstructed in both spectrometers, with measured momentum and negative charge, having 10 or more hits in the silicon detectors;
4. additional tracks are also allowed if they are shorter than 150 cm or have $\chi^2/NDF > 5$ or they are reconstructed downstream of the ECAL2. Such tracks are treated as mis-reconstructed.

5.3.3 Vertex

One assumes that interaction took place in the target if the vertex lies in the XY-plane inside a circle with $r = 1.4$ cm centered at the nominal target center. The coordinate Z_{vertex} must be in the range $\Delta Z = \pm 4\,\mathrm{cm}$, for pions scattered to large angles ($\theta_{scatt} > 1\,\mathrm{mrad}$), and $\Delta Z = \pm 30\,\mathrm{cm}$ for scattering angles $\theta_{scatt} < 1\,\mathrm{mrad}$, with respect to the nominal target Z position (-309.6 cm for a single target and -304.6 cm, -314.5 cm for segmented targets), see Fig. 5.1. Events with $Z_{vertex} = -250$ cm correspond to beam interactions in the trigger scintillator. The value $r < R_{target}$ was selected to avoid any effects related to possible target misalignments. The choice of the ΔZ value is based on the experimental resolution for the Z-vertex.

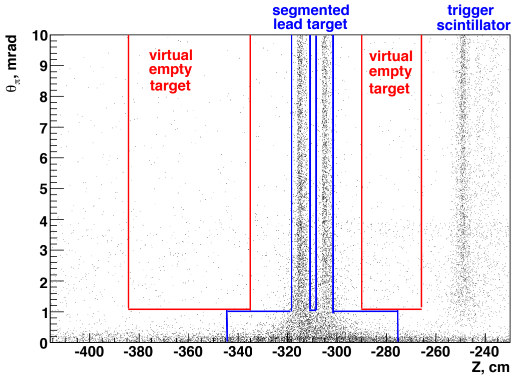

Figure 5.1: Z-distribution of the vertexes of $\pi\gamma$ events for segmented target. The borders of the Z-cut and virtual empty targets are shown.

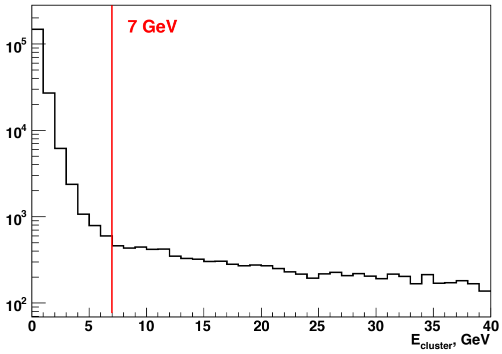

Figure 5.2: Cluster energy distribution for ECAL2.

5.3.4 Photon reconstruction

High energy photons produced in the Primakoff reaction are detected by the ECAL2. The noise was suppressed by the requirement of a minimum energy of 7 GeV (Fig. 5.2) for the ECAL2 clusters. The scattered pions traversing the ECAL2 calorimeter have some probability to produce electromagnetic and hadronic showers and thus generate an energy cluster above the noise threshold. Such clusters can be identified by extrapolating the pion track to the ECAL2 Z-position and looking for an energy cluster located within a radius of 5 cm from the pion impact point. (The standard track-cluster association provided by PHAST was not used because the clustering in the electromagnetic calorimeter is not optimized for the reconstruction of hadronic showers and sometimes the standard procedure of association of a pion track with a pion cluster fails. It was found that the 5 cm region around the pion impact point includes practically all clusters produced by a pion.) Events with more than one high energy cluster (excluding the eventual pion cluster), thus not matching the topology of the studied reaction, are rejected.

5.3.5 Muon background rejection

The pion beam contains about 3% of muons which produce background events. The fraction of muon events increases in the region of high ω as the relative Primakoff cross sections for muons and pions (see Fig. 5.3). In order to cut off muon background the standard PHAST algorithm was used, which takes into account the amount of material in terms radiation lengths traversed by the track. The muon identification power as function of muon momentum for particles with scattering angle below 10 mrad is shown on Fig. 5.4.

5.3.6 Multiple scattering in the target

Plane deflection of ultrarelativistic particle with momentum P, passed through the material with thickness x and radiation length X_0, can be described by the gaussian distribution with parameter θ_0

$$\theta_0 = \frac{14\ MeV}{Pc} \times \sqrt{\frac{x}{X_0}}. \tag{5.2}$$

Spatial θ_{space} deflection is $\sqrt{2}$ times larger. For a 3 mm lead target the scattering angle for 190 GeV/c pions θ_{space} is 0.07 $mrad$. If the scattering angle in Primakoff interaction for pions in lead is of the same order of magnitude, the real Primakoff events produced in the target cannot be distinguished from those when a pion suffers only multiple scattering in the target, while the Primakoff scattering occurs elsewhere (for example in the multiplicity counter or in the silicons). Moreover, for small scattering angles the resolution on the vertex Z position is highly degraded. The P_t resolution for the scattered particle due to multiple scattering in the target material is about 15 MeV/c. To suppress all the effects related to multiple scattering the events with $P_t < 45 MeV/c$ are rejected.

This cut is also effective against electron background, because for electron events typical Primakoff scattering angle for electron is about $m_e/E_{beam} \approx$ 0.003 $mrad$ that is much smaller than the angle of multiple scattering in the target material.

5.3.7 Exclusivity cuts

The exclusivity of Primakoff events is guaranteed by the cuts on the total energy and Q^2.

Assuming zero energy transfer for Primakoff scattering (in fact it is much less than energy resolution of the ECAL2), $E_{beam} = E_{\gamma\ cluster} + E_{\pi}$. The

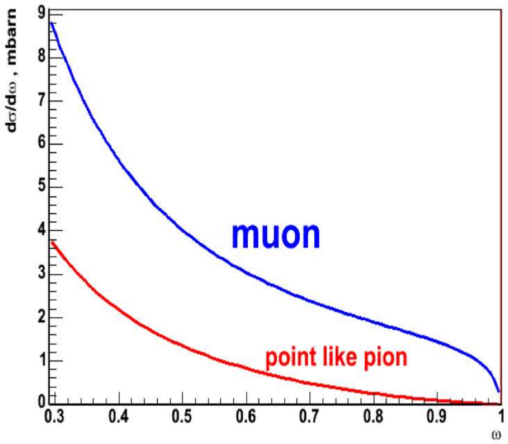

Figure 5.3: Primakoff differential cross sections $d\sigma/d\omega$ for muon and point-like pion.

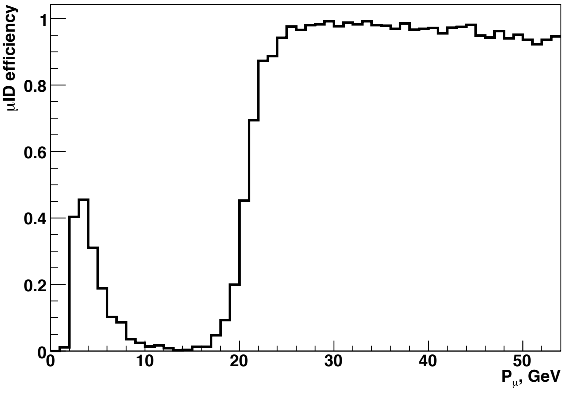

Figure 5.4: Efficiency of muon identification as a function of muon momentum.

width of the reconstructed beam energy peak is about 6 GeV and the main contribution to the peak width is due to the ECAL2 energy resolution. In analysis one accepts only events for which the reconstructed beam energy ($E_{\gamma\ cluster} + E_{\pi\ scatt.}$) is in the range 165 - 215 GeV (Fig. 5.5).

The diffractive scattering process produces some background in the region of large Q^2 while the peak at $Q^2 = 0$ corresponds to the Primakoff events. The contribution of the pion diffractive scattering can be deduced from the comparison of the Q^2-distributions for pion and muon events (see Fig. 5.6). The shape of the Primakoff peak can be described by exponential function

$$N(Q^2) = N(0)e^{-\frac{Q^2}{(dQ)^2}}, \tag{5.3}$$

where $dQ = 18\ MeV$ is the resolution of the setup for the transferred momentum.

To distinguish between Primakoff and diffractive scattering the cut $Q^2 < 2 \times 10^{-3}(GeV/c)^2$ was applied.

To take into account the contribution from diffractive events at low Q^2 diffractive background was fitted by an exponential function in the range $(2\times 10^{-2}{-}1\times10^{-1})(GeV/c)^2$ and the fitted curve was extrapolated to $Q^2 = 0$. To study the uncertainties related with diffractive and empty target background subtraction Q^2-cut changed in the range from 0.75×10^{-3} (GeV/c)^2 to $9.0 \times 10^{-3}(GeV/c)^2$.

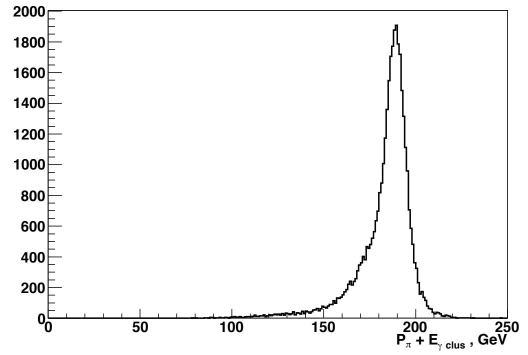

Figure 5.5: Distribution for $E_{\gamma\ clus} + E_\pi$.

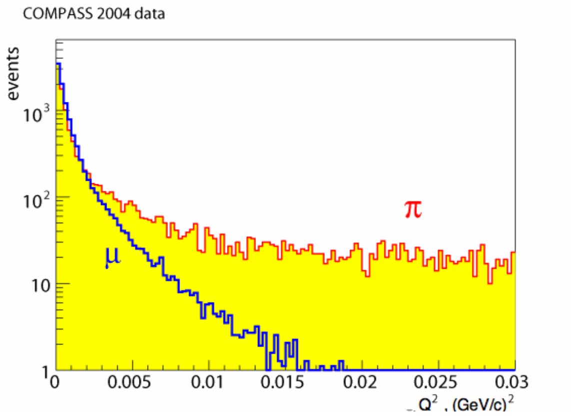

Figure 5.6: The Q^2-distributions for pion and muon events.

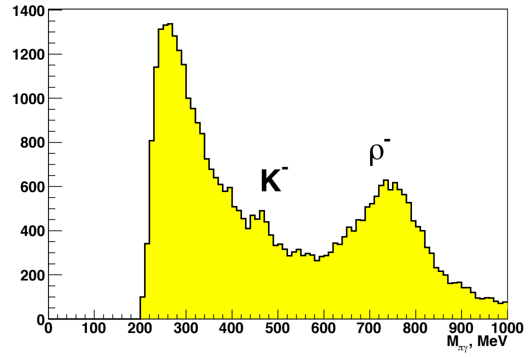

Figure 5.7: Distribution for the $\pi\gamma$ invariant mass $M_{\pi\gamma}$.

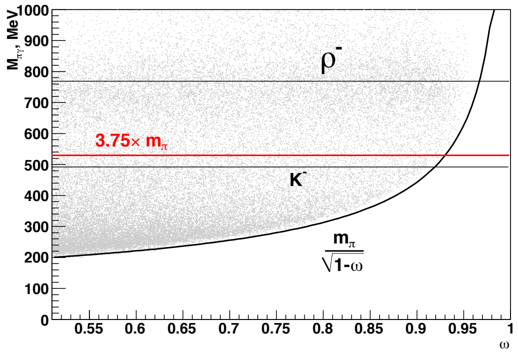

Figure 5.8: ω vs. $M_{\pi\gamma}$ distribution for Primakoff candidate events.

5.3.8 Final state invariant mass

The invariant mass spectrum of the reconstructed $\pi\gamma$ system after all the previous cuts shows two peaks at $\sim\ 500\ MeV$ and $\sim\ 770\ MeV$ (Fig. 5.7). These are the peaks of background events from K^- and ρ^- decays, the peaks are shifted and skewed due to the missing reconstruction of one of the photons from the $\pi^0 \to \gamma\gamma$ decay. To reject the most part of such background events the cut $M_{\pi\gamma} < 3.75 \times m_\pi$ was applied. To study systematic uncertainties related with residual ρ-meson background the M-cut was variated in the range from 3.3 to 4.0 m_π.

As for kaon background, it's not reasonable to reject it by applying M-cat on the level below kaon mass because due to such cut the significant part of the Primakoff events in the range $0.85 < \omega < 0.9$ will be lost (see Fig. 5.8).

5.3.9 π^0 background estimation and subtraction

The estimation of π^0 background contribution into the Primakoff sample is based on the using of calorimeter information. It includes two steps:

- analysis of the photon cluster shape to distinguish between single and double photon clusters;
- searching for clusters produced by second soft photon from π^0 decay.

Two weakly correlated parameters were used to characterize the shape of ECAL2 cluster: the cluster RMS, which is the root mean square of spatial distribution of energy deposition in cluster, and the parameter R_4, which is the energy deposition in four the most energetic cells normalized to the cluster energy. Fig. 5.9 shows combined distributions of RMS and R_4 values for events having configuration (5.1) and collected with pion and muon beam. The sample of muon events doesn't contain contamination of π^0 events and all clusters are the single photon clusters. The events with

$$R_4 < 0.65 + 0.06 \times RMS\ [cm] \tag{5.4}$$

can be treated as double photon clusters and rejected.

The recovering of the second soft photon was done in the range $1.5\ GeV < E < 7\ GeV$ of cluster energy. The great amount of lowenergetic noise clusters (noise of electronics, dominating for $E < 2\ GeV$, and pile up clusters) complicate the recovering procedure (see Fig. 5.10). An event was treated as π^0 event if at least for one of photons, associated with each lowenergetic cluster, the invariant mass of hard and soft photons is close to the nominal mass of π^0: $|m_{\gamma\gamma} - m_\pi| < 30\ MeV$ (see Fig. 5.11). π^0 peak in the mass spectrum is absent for events collected with muon beam (see Fig. 5.12).

The algorithm of π^0 identification, described above, can be characterized by two quantities. The efficiency A shows which fraction of π^0 events can be identified. The quantity B is the probability to misidentify an event with one photon as an event with π^0.

To calculate the efficiency A the events with primary vertex in free space up- and downstream of the Pb target were used (so called virtual empty targets). The borders of the space used as virtual empty targets are shown in Fig. 5.1. The Primakoff-like events with vertexes up- and downstream of the target are the events of $K^- \to \pi^- + \pi^0$ decay misidentified as $\pi^-\gamma$-events.

The value of B can be estimated using the data collected with muon beam where there is no π^0 background. The values of A and B for different ω are presented on Fig. 5.13. Knowledge of A and B allows to estimate the total number N_{π^0} of π^0 events in Primakoff sample before the calorimeter cuts:

$$N_{\pi^0} = \frac{N_{rej} - BN_0}{A}, \tag{5.5}$$

where N_{rej} - the number of events, rejected by calorimeter cuts and N_0 - the total number of events in Primakoff sample (see Fig 5.14). The number of remaining $\pi^-\pi^0$ events needs to be subtracted after calorimeter cuts is

$$N_{sub} = N_{\pi^0} - N_{rej} = \frac{N_{rej}(1-A) - BN_0}{A}. \tag{5.6}$$

5.3.10 Estimation of the collected statistics of Primakoff events.

The cuts described above reject the most part of background processes mentioned in Sec. 5.2. Background from diffractive $\pi\gamma$ events and from π^0 events, which cannot be rejected by cuts, was subtracted according the procedures described in Sec. 5.3.7 and Sec. 5.3.9 correspondently. The number of $\pi\gamma$ events before subtraction and the number of subtracted diffractive and π^0 events as function of ω for 3 mm Pb target is presented in Fig. 5.15. The samples of $\pi\gamma$ events passed through the cuts and background subtraction procedures can be treated as pure samples of Primakoff events. The number of Primakoff events collected with pion beam in the range $0.5 < \omega < 0.9$ is about 1.4×10^4 for Pb targets (2+1 mm, 3 mm and 1.6 mm), about 800 events for Cu and 350 events C target. The corresponding statistics for muon events and Pb target is 6×10^4. ω-distributions for pion and muon Primakoff events collected with lead targets are shown in Fig 5.16.

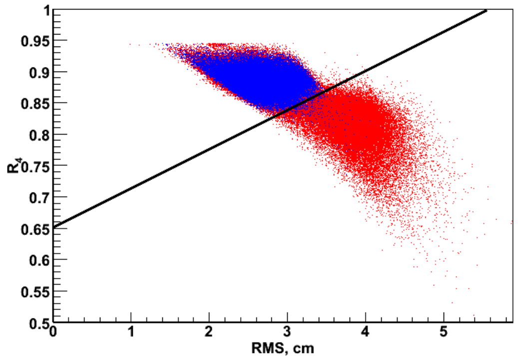

Figure 5.9: Distribution of the RMS and the R_4 for clusters produced with pion (red) and muon (blue) beam.

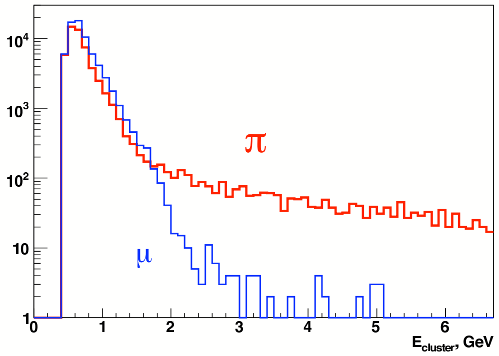

Figure 5.10: Lowenergetic noise in ECAL2 for muon and pion beam.

5.4 Monte Carlo simulation of Primakoff scattering events in the COMPASS setup

The first Monte Carlo studies of the Primakoff reaction at the COMPASS setup were performed before the data taking [85],[86] with an schematic, approximate description of the detector. After the data taking the real setup was simulated.

In order to simulate the passage of scattered pion and photon produced in Primakoff scattering through the COMPASS setup the standard tool chain was used (see Sec. 4.5.1). MC samples were produced for Pb, C and Cu targets. The number of MC events was at least one order larger than the number of Primakoff events collected in 2004 so a statistical error introduced by MC can be neglected.

To generate the Primakoff events the POLARIS generator [87] was used. The events were generated according to the Primakoff cross section calculated under the Weizsäcker-Williams approximation for the point-like pion. The input parameters for the generation were:

- Beam pion momentum: 190 GeV
- Emitted photon energy in the lab. frame: 40-190 GeV
- s $< 200\ m_\pi^2$
- $Q^2 < 1 \times 10^{-2} (GeV/c)^2$

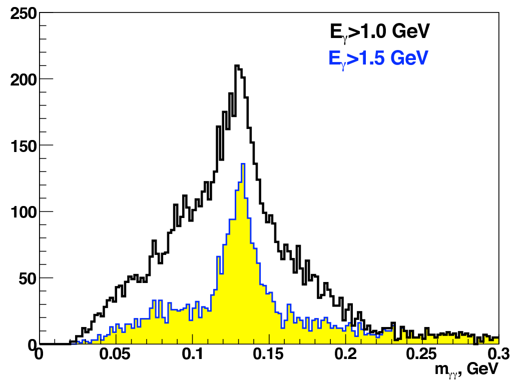

Figure 5.11: Distribution for the invariant mass $m_{\gamma\gamma}$ of hard photon and soft photons, associated with low-energetic clusters in ECAL2 for two values of minimal cluster energy.

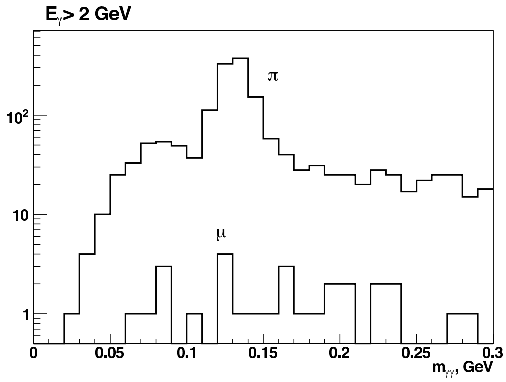

Figure 5.12: Distribution for the invariant mass $m_{\gamma\gamma}$ of hard photon and soft photons, associated with low-energetic clusters in ECAL2 for pion and muon events.

To generate muon events the POLARIS generator was modified: the expression for the Compton cross section for scalar particle was replaced by corresponding expression for a particle with spin 1/2.

It was shown in [85] that pile up effects do not change the shapes of the kinematical distributions for the Primakoff events. But pile up was also taken into account in Monte Carlo simulation. To simulate pile-up effects 300 ns time gate was used.

In order to take into account the cell-by-cell energy mis-calibration of ECAL2 the energy resolution

$$\Delta E/E = 8\%/\sqrt{E} + 5.5\% \tag{5.7}$$

was applied, that worse than the nominal resolution of the central part of ECAL2 (see 4.4.6).

The efficiency of the $Primakoff2$ trigger as a function of the energy deposition in ECAL2 was described by expression

$$e_{P2}(E) = \frac{A}{1 + e^{(E^0_{P2} - E)/\Delta E_{P2}}}, \tag{5.8}$$

where A=1, $E^0_{P2} = 85.9\,GeV$, $\Delta E_{P2} = 6.4\,GeV$ are parameters of the trigger threshold.

The Fig. 5.17, showing $E_{\gamma\ cluster} + E_\pi$ distribution for $\mu\gamma$ events for real

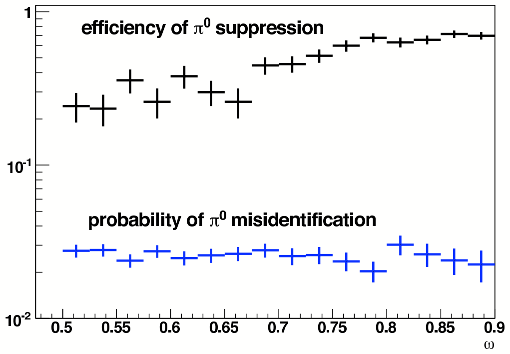

Figure 5.13: A and B as functions of ω

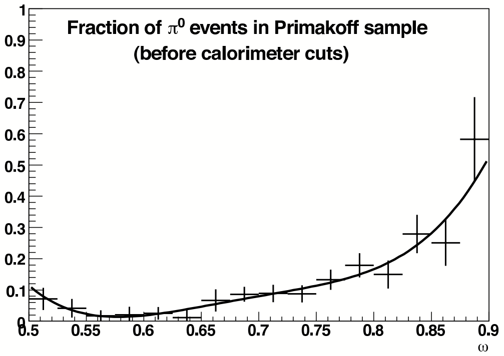

Figure 5.14: Fraction of $\pi^-\pi^0$-events in Primakoff sample as function of ω (before rejection)

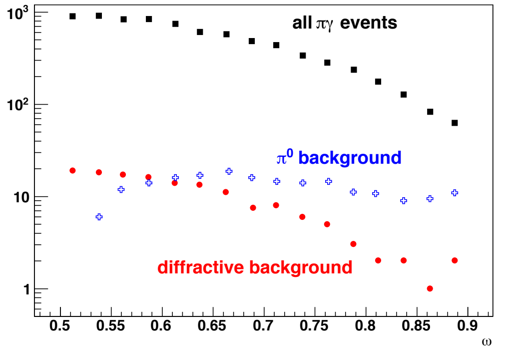

Figure 5.15: ω-distributions of all $\pi\gamma$-events (boxes), subtracted diffractive background events (points) and subtracted π^0 background events (crosses) (3 mm Pb target).

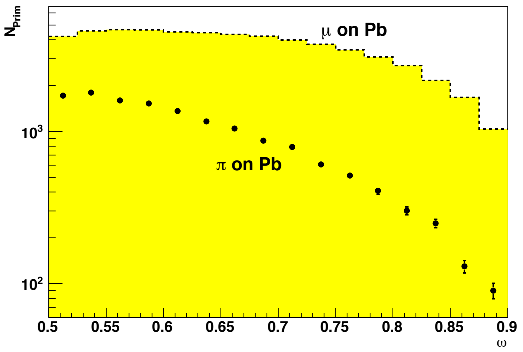

Figure 5.16: ω-distribution for Primakoff events collected with muon and pion beams (Pb targets).

data and for Monte Carlo events, illustrates the good quality of MC simulation.

The calculated acceptance function $a(\omega)$ for the 2+1 mm lead target is presented in Fig 5.18. It has a smooth shape in the selected ω-range. That means that the COMPASS geometry and the selection criteria are convenient to study the Primakoff reaction. Mean values of acceptance $\bar{a}$ for other targets are presented in Tab. 5.5. The main factors that reduce the acceptance are:

- photon conversion into e^+ e^- pair in the material of the target and setup elements (the effective thickness of the COMPASS setup excluding target is about $0.25X_0$ or about $0.07\lambda_I$);

- secondary interaction of scattered pion;
- inefficiency of tracking and vertex reconstruction algorithms;
- presence of pile up tracks and clusters.

5.5 Primakoff scattering on different nuclear targets

The comparison of data samples collected with different targets provides the possibility to see the Q^2-behavior of the Primakoff signal and diffractive scattering background for different materials and to check the Z^2 dependence for the Primakoff cross section. In Fig. 5.19 one can see that Primakoff signal at $Q^2 = 0$ increases with increasing Z. The Primakoff cross sections for different materials normalized to the cross section for lead are shown in Fig. 5.20. The dotted line corresponds to Z^2 -dependence. One can see that the measured values satisfy the Z^2 dependence rule for a wide range of Z. This proves that selection criteria effectively select Primakoff events and reject background events.

Table 5.2: Acceptance a averaged over the range $0.5 < \omega < 0.9$ for lead, carbon and copper targets.

Target	Beam	Acceptance, $\bar{a}$
Pb 1.6 mm	π	0.21
Pb 1+2 mm	π	0.18
Pb 1+2 mm	μ	0.12
C	π	0.20
Cu	π	0.22

5.6 Estimation of the Primakoff cross section

The theoretical prediction of the Primakoff cross section for the COMPASS conditions (E_0=190 GeV, Pb target, $0.5 < \omega < 0.9$) under the Born approximation for the point-like pion is 0.24 mbn. Radiative corrections

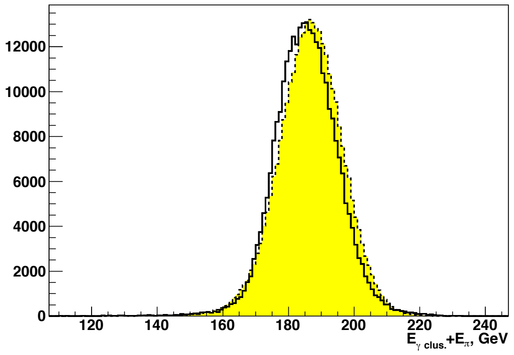

Figure 5.17: Distribution for $E_{\gamma\ cluster}+E_{\pi}$ for $\mu\gamma$ events for real data (solid line) and MC simulation (dotted line).

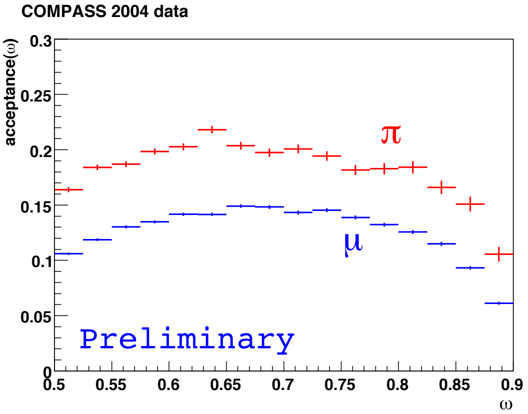

Figure 5.18: Acceptance a for 2+1 mm Pb target as function of ω.

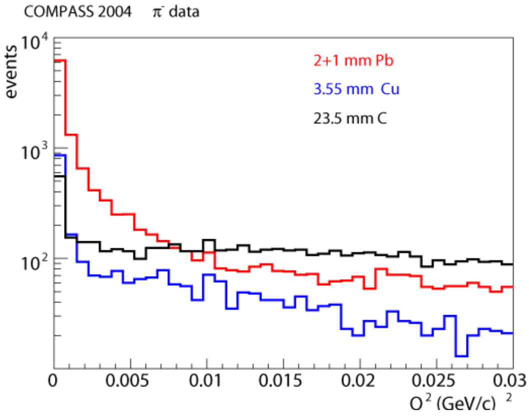

Figure 5.19: The Q^2 distributions for led, copper and carbon targets.

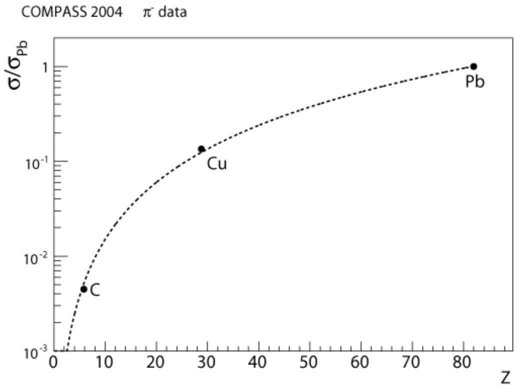

Figure 5.20: The Z^2-dependence of Primakoff cross section.

(see [52]-[56]) reduce it to 0.21 mbn. Primakoff cross section for pion with ($\alpha_\pi = -\beta_\pi = 6.9 \times 10^{-4}\ fm^3$ is about 0.20 mbn.

The measurement of the absolute values of cross sections is not a purpose of the COMPASS experiment and the COMPASS setup is not optimized to do it. The measurement of the Primakoff cross section cannot be performed with accuracy better than 20% due to uncertainty in the estimation of the integral beam flux. The experimentally estimated cross section is

$$\sigma_{Primakoff}(Pb) = 0.15 \pm 0.03\ mbn, \tag{5.9}$$

that is in satisfactory agreement with the theoretical prediction.

5.7 Estimation of the statistical and systematic uncertainties

As it was shown in Sec. 3.2, the pion polarizability α_π can be extracted under assumption $\alpha_\pi + \beta_\pi = 0$ from the ratio $R(\omega)$ of the measured differential Primakoff cross section to the theoretically predicted for a point-like pion. $R(\omega)$ can be expressed as:

$$R(\omega) = \frac{d\sigma_{measured}/d\omega}{d\sigma_{p.l.}/d\omega} = \frac{N_{Prim}(\omega)}{a(\omega) d\sigma_{point-like\ \pi}/d\omega}, \tag{5.10}$$

where $N_{Prim}(\omega)$ is the measured ω distribution of Primakof events presented in Fig. 5.16, $a(\omega)$ is the acceptance function calculated using MC and presented in Fig. 5.18 and $d\sigma_{point-like\ \pi}/d\omega$ is theoretically predicted differential cross section (Born term + radiative corrections). The statistical precision of acceptance calculation is limited only by the MC statistics and can be as good as one wants. Theoretical calculation of the cross section can also be done very precisely. Thus the precision of $N_{Prim}(\omega)$ measurement defines the statistical error of the pion polarizabilities measurement under assumption $\alpha_\pi + \beta_\pi = 0$. The statistics collected in 2004 with Pb target and suitable for analysis corresponds to the statistical error

$$\sigma_{stat} = 1.2 \times 10^{-4}\ fm^3. \tag{5.11}$$

The main sources of contribution to the systematic uncertainties are:

- uncertainty related with description of setup performance in the Monte Carlo simulation. It can be estimated using data collected with muon beam. The minimal possible contribution is limited by the statistics collected with muon beam. Muon statistics collected in 2004 corresponds to $\sigma_{syst.\ MC} > \pm 0.5 \times 10^{-4}\ fm^3$,
- uncertainty related with subtraction of diffractive background. It was estimated by variating the parameter of Q^2 cut and the Q^2 range of diffractive background fitting and is $\sigma_{syst.\ diff} = \pm 0.2 \times 10^{-4}\ fm^3$,
- uncertainty related with π^0 background subtraction. The accuracy of subtraction procedure depends on the statistics and corresponding con-

Table 5.3: The estimation of the possible statistical and systematic uncertainties of α_π measurement under assumption $\alpha_\pi + \beta_\pi = 0$ (Pb target).

	Error, $10^{-4} fm^3$
STATISTICAL ERROR	$\pm 1.2 \times 10^{-4}$
SYSTEMATIC ERROR	$\sim \ \pm 2 \times 10^{-4}$
Setup description in MC	± 0.5
Subtraction of diffractive background	± 0.2
Subtraction of π^0 background	± 0.3
Background from $\mu^- + A \to \mu^- + A + \gamma$	$+0.2$
Background from $e^- + A \to e^- + A + \gamma$	$<+0.1$
Setup performance	$\sim \pm 1.5 \times 10^{-4}$

tribution to the systematic uncertainty was estimated to be $\sigma_{syst.\ \pi^0} = \pm 0.3 \times 10^{-4}\ fm^3$,

- uncertainty related to contamination of muon events in Primakoff sample. The estimation is based on the study of the muon identification efficiency. Contribution was estimated to be $\sigma_{syst.\ \mu} = +0.2 \times 10^{-4}\ fm^3$,
- uncertainty related to contamination of electron events in Primakoff sample. The upper limit of this contribution was estimated using the data collected with the electron converter installed. $\sigma_{syst.\ e} < +0.1 \times 10^{-4}\ fm^3$.

Unfortunately the bigger part of the statistics was collected under unstable conditions of the detector operation that introduced additional systematic uncertainty about $\pm 1.5 \times 10^{-4}\ fm^3$. The estimated contributions into the systematic error from the different background processes are presented in Table 5.3. So the possible total error of pion polarizability measurement under assumption $\alpha_\pi + \beta_\pi = 0$ in 2004 is about $2 \times 10^{-4}\ fm^3$.

It's important to emphasize that the systematic uncertainties related to subtraction of the diffractive background and the background of the events with π^0 have the statistical nature and decrease with increasing of the statistics. That is true also for the lower limit of the contribution to systematics of the setup performance and the quality of the Monte Carlo description. So they can be decreased in future data taking by collecting more events.

The precision of pion polarizabilities measurement, based on the data collected in pilot hadron run 2004, could not be better than in the most precise previous experiments. Significant result may be obtained only with a new data taking at COMPASS.

Chapter 6

Possibility of future measurements at COMPASS

The pilot hadron run 2004 has shown, that the COMPASS setup provides good opportunity to measure pion polarizabilities precisely. New data taking for Primakoff studies is scheduled to October - November of 2009. Taking into account the experience obtained during the pilot run 2004 some changes in the setup and in strategy of data taking are proposed [88], [89].

6.1 Proposed changes in the COMPASS hadron setup.

6.1.1 Primakoff trigger

As Primakoff analysis has shown, the trigger $Primakoff$ 2 is simple for understanding and Monte-Carlo simulation, effective and covers the most important part of the kinematic region. In 2009 one proposes to use modified $Primakoff$ 2 trigger as the main trigger for pion polarizabilities measurement. Due to small scattering angles $\sim m_\pi/E_{beam}$ hard Primakoff photon clusters are localized in a few central cells of ECAL2. To keep selective power of the Primakoff trigger and reduce significantly its threshold, it is reasonable to include into the trigger only the central part of ECAL2. An experience of data taking in 2004 shows that it is enough to include into the trigger just 12 × 12 central cells with common threshold about 60-70 GeV/c. It is also useful to exclude from the trigger cells around the beam hole which are hit by scattered beam pions. Configuration of the Primakoff trigger, proposed for run 2009 is shown in Fig. 6.1.

Otherwise trigger $Primiakoff$ 1 is not so convenient for analysis: it has different structure for muon and hadron beams (in the case of the muon beam HCAL2 was removed from trigger) and its structure complicates trigger precise implementation in MC. It will not be used in Primakoff run 2009.

In addition to $Primakoff$ 2 trigger is reasonable to use other prescaled trigger involving the same ECAL2 region as $Primakoff$ 2 but with lower threshold - the $Primakoff$ 3 trigger. It can be used for study and control of $Primakoff$ 2 behavior and for triggering of processes with lower energy deposition in the central region of ECAL2.

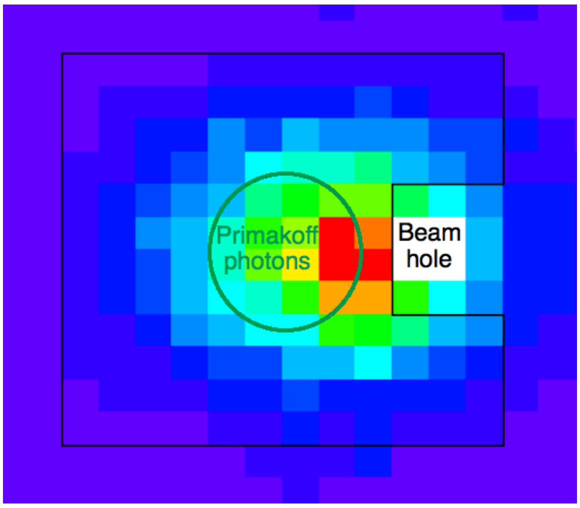

Figure 6.1: Central region of ECAL2. Region involved into the trigger is shown. Color background shows relative energy deposition in the calorimeter.

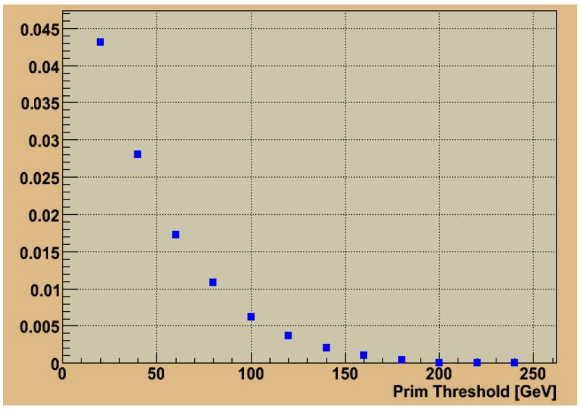

Figure 6.2: $Primakoff$ 2 trigger rate as a function of the trigger threshold normalized to the rate of the beam trigger ($16x16$ cells) (2009, preliminary).

In order to preparation to new data taking different geometrical configurations of the trigger have been also tested. Fig. 6.2 presents a result of threshold scan for a configuration with 16×16 cells included into the trigger. The relative efficiency of $Primakoff$ 2 trigger is measured using the trigger $Primakoff$ 3, which is prescaled by the factor of 2 and has threshold about 40 GeV (Fig. 6.3). The shape of the threshold can be fitted by the function (5.8) with parameters A=0.99, E_0=67 GeV, ΔE=1.6 GeV. The trigger threshold in 2009 is much sharper then in 2004 (see Sec. 5.4) and the efficiency becomes a constant already above $\sim 75\ GeV$. So the ω-range above 0.4 potentially can be used for analysis.

6.1.2 Beam and beam line

COMPASS DAQ system was upgraded since 2004 and to obtain high statistics in short time the intensity of pion and muon beams can be increased to $(2-4)\times 10^7$ (DAQ limitation, it depends on the trigger threshold) and $\sim 5\times 10^7$ (beam line limitation) particles per 10 s spill correspondently.

Cherenkov differential counter (CEDAR) operates since 2008 and can be used for π/K separation. Fig. 6.4 shows the result of pressure scan. The count rates of the majorities by the 8 and 6 photomultipliers normalized to beam counters in the beam line are plotted over the applied pressure. One can see how the separation between kaons and pions is increased by applying higher majorities. But with growing majorities the efficiency is reduced. The efficiency times the geometrical acceptance of the detector is around 35% for 6-fold events.

Tests with an electron converter in 2004 have shown that installation of 0.5 X_0 lead electron converter in the beam line just downstream of the primary target keep small the divergency of the pion beam (Fig. 6.5) which is important for CEDAR performance. Such converter reduce the contamination of electrons by the factor of ~ 100. In 2009 the electron converter should be installed permanently.

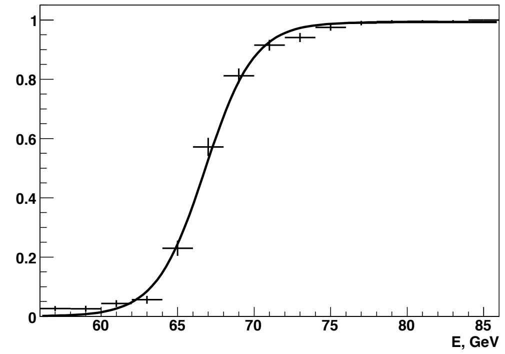

Figure 6.3: The efficiency of $Primakoff$ 2 trigger, measured in respect to $Primakoff$ 3 trigger (2009, preliminary).

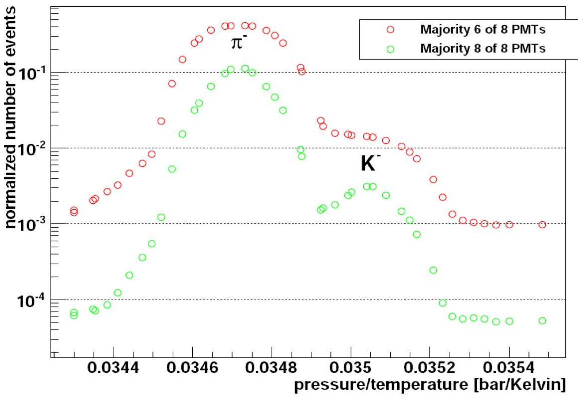

Figure 6.4: The result of a pressure scan performed with CEDAR [90].

6.1.3 Target.

As it was shown in [52]-[56], the radiative corrections to the Primakoff Born cross section for Pb become big, especially, the correction related to the nuclear form factor ($0.6 \times 10^{-4} fm^3$). To decrease dependence of the result on the corrections calculation it's reasonable to choose target material with smaller Z. Z should not be too small to avoid problems with significant diffractive background and from this point of view materials with Z around 30 are promising. Ni (Z=28) is proposed to be used as the main material. Spin-0 of $^{58}_{28}$Ni nucleus simplifies the estimation of corrections.

The optimal thickness of a Ni target coming from the compromise between the number of Primakoff events which can be collected in limited time, and quality of Primakoff signal and diffractive background separation. The expected statistical error, expressed in arbitrary units, as a function of Ni target thickness is shown in Fig. 6.6. So 0.3 X_0 is the optimal target thickness for future measurement.

To decrease the background coming from beam kaons decay it's recommended to use single target instead of segmented one.

The requirement to the target region is to have enough free space up- and downstream of the target to use them as virtual empty targets and collect statistics of $K^- \rightarrow \pi^- + \pi^0$ events which are needed for π^0 background study and elimination.

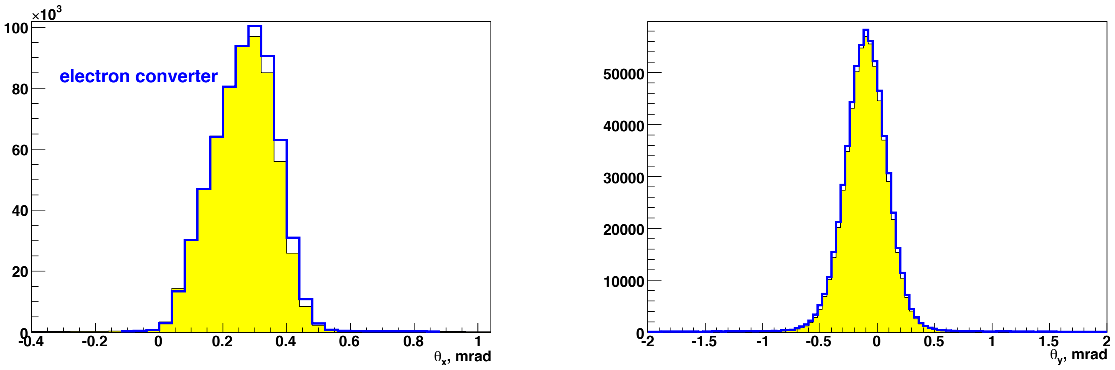

Figure 6.5: Angular divergency of pion beam with and without electron converter (2004).

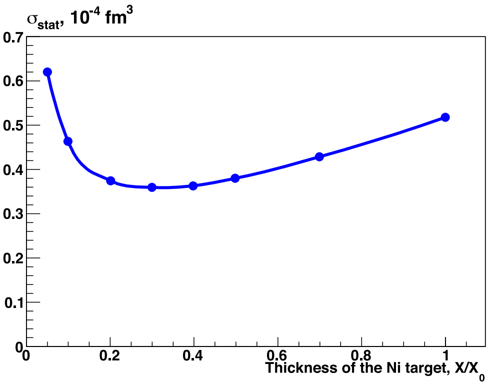

Figure 6.6: Dependence of the statistical error σ_{stat} on the Ni target thickness (15 days of data taking).

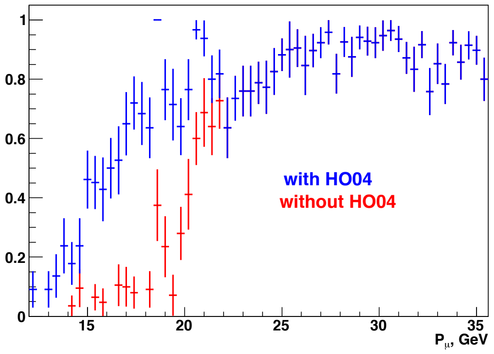

Figure 6.7: Muon identification efficiency with and without hodoscope HO04 (2009, preliminary).

6.1.4 Scattered particle identification

To extend the region of scattered muon identification below P=20 GeV/c additional hodoscope downstream the MW2 will be involved. The hodoscope HO04, previously used as trigger hodoscope in muon program, provides muon identification in the range above P=15 GeV/c (ω<0.92). Muon identification efficiency with and without hodoscope HO04 is shown in Fig. 6.7.

An outer part of hadron calorimeter HCAL2 can also be used for identification of particles with low momenta. Particle with energy deposition in HCAL2 corresponding to minimum ionizing particle is treated as muon. This option was not accessible in 2004 because an outer part of HCAL2 was shielded by lead blocks.

6.1.5 Time information of ECAL2 clusters

New SADC electronics of ECAL2 provides possibility to measure cluster time in respect to trigger time. The cluster time is evaluated using so-called "constant fraction" method, where the time is defined when the half of the front amplitude signal from SADC is reached. Resolution for cluster time depends on cluster energy and is about 1 ns. Time information is useful for identification of pile up clusters. It should significantly improve the quality of π^0 background rejection because the ECAL2 is polluted by lowenergetic pile up clusters which complicate the procedure of searching for second photon

Table 6.1: Proposed total beam flux for pions and muons in 2009 and expected statistical, systematic and total errors ($10^{-4} fm^3$).

Weeks	π beam, days	μ beam, days	Total flux $\pi, 10^{11}$	Total flux $\mu, 10^{11}$	σ_{stat}	σ_{syst} min.	σ_{tot} min
4	14	14	8.3	8.3	0.35	0.2	0.4

from π^0 decay (see Sec.5.3.9). Fig. 6.8 illustrates separation between clusters from particles came in time and pile up clusters for events with pion and muon beam. Peak at zero corresponds to clusters from triggered event, flat background which is different for pion and muon events, corresponds to pile up clusters.

6.2 Estimation of possible precision of polarizabilities measurement in 2009.

The estimation of possible statistical and systematic errors is performed for 4 weeks of stable data taking. The beam time sharing between pion and muon beam is based on the fact, that to keep the minimal possible value of systematic uncertainty two times lower than statistical error, one needs to collect approximately equal integral beam fluxes with pion and muon beams. The calculations are done for $0.3X/X_0$ Ni target, ω interval $0.4 < \omega < 0.925$, pion beam intensity 4×10^7 particles per spill and muon beam intensity 4×10^7 particles per spill. The acceptance for Primakoff events and the efficiency of the selecting cuts are supposed to be the same as in 2004. It is also assumes that COMPASS is able to collect 2000 spills per day and this possibility will be realized with an efficiency 75%. Table 6.1 shows the expected integral beam fluxes for pion and muon beam, statistical error and minimal possible systematic and total errors. A time needed for detector commissioning is not included into the table. Small data samples with empty target, which can help to study the systematic effects, are also not included into this table (their collection should take just a few hours). Expected number of Primakoff events produced by the pion beam in ω-range, mentioned above, is about 3×10^5.

The comparison of the accuracies of pion polarizabilities measurement for the most precise previous experiments, the COMPASS data taking in 2004 and the expected data taking in 2009 is presented in Tab. 6.2.

Table 6.2: Comparison of statistical and systematic errors for COMPASS and the most precise previous measurements.

Experiment	$\sigma_{stat}, 10^{-4} fm^3$	$\sigma_{sys}, 10^{-4} fm^3$	$\sigma_{tot}, 10^{-4} fm^3$
Protvino [38]	1.4	1.2	1.8
MAMI A2 [40]			1.7
MARK II [35]			1.6
COMPASS 2004	1.2	~ 1.5	~ 2
COMPASS 2009 (4 weeks of data taking)	0.35	≥ 0.2	≥ 0.4

The large statistics will provide also possibilities for

- the independent measurement of α_π and β_π with at statistical error of about $0.5 \times 10^{-4}\ fm^3$;
- the measurement of the pion polarizability not only averaged in $M_{\pi\gamma}$-range below some limit, as it was done before, but also for the measurement of the dynamic polarizability $\alpha_\pi(M_{\pi\gamma})$ in the range of $M_{\pi\gamma}$ up to $\sim 0.55\ GeV$ [43];
- the tests of the α_π dependence on ω, predicted by some theoretical models [15].

6.3 Possibility of kaon polarizabilities measurement at COMPASS.

In addition to a precise determination of the pion polarizabilities, COMPASS has a chance to perform the first measurement of Primakoff scattering off charged kaons and to estimate the kaon polarizability [91], [60]. Taking into account that contamination of kaon in hadron beam is about 3%, CEDAR efficiency of kaon identification is not less than 35% and that the

Primakoff cross section depends on the particle mass as:

$$\sigma_{Prim} \sim \frac{1}{m^2}, \tag{6.1}$$

the number of Primakoff kaon events can be estimated. It is about 100 per 10^5 pion events.

The χPT prediction for α_K is [91]:

$$\alpha_K + \beta_K = 0, \quad \alpha_K = \alpha_\pi \times \frac{m_\pi F_\pi^2}{m_K F_K^2} \approx \frac{\alpha_\pi}{5}, \tag{6.2}$$

where F_π, F_K decay constants for pion and kaon. According to Eq. 3.22 the contribution of the polarization term into the cross section is proportional to $m_{\pi,K}^3 \times \alpha_{\pi,K}$, that amplifiers the polarization effects for kaon in respect to pion by the factor of 9. Ratio of the Primakoff differential cross section for kaon with polarizabilities $\alpha_K = -\beta_K = 0.6 \times 10^{-4}\ fm^3$ to corresponding differential cross section for point-like kaon is presented in Fig. 6.9.

After 4 weeks of data taking at COMPASS the value of α_K under assumption $\alpha_K + \beta_K = 0$ can be estimated with statistical accuracy about $0.25 \times 10^{-4}\ fm^3$.

Main contribution into systematic error will come from K/π misidentification by CEDAR, from kaon decay

$$K^- \to \pi^- + \pi^0 \to \pi^- + \gamma + \gamma \tag{6.3}$$

and from $K^*(892)$ production and decay

$$K^- + Pb \to K^*(892) + Pb \to Pb + K^- + \pi^0 \to Pb + K^- + \gamma + \gamma. \tag{6.4}$$

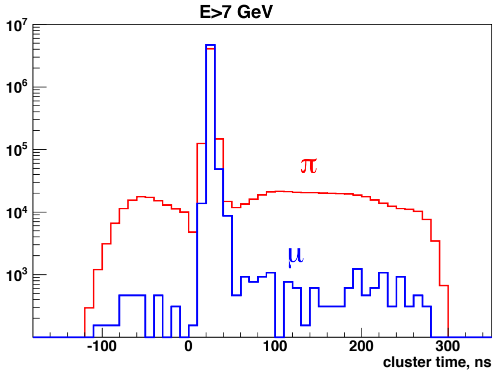

Figure 6.8: Cluster time in respect to trigger time for events with pion and muon beam. Energy of clusters is above 7 GeV (2009, preliminary).

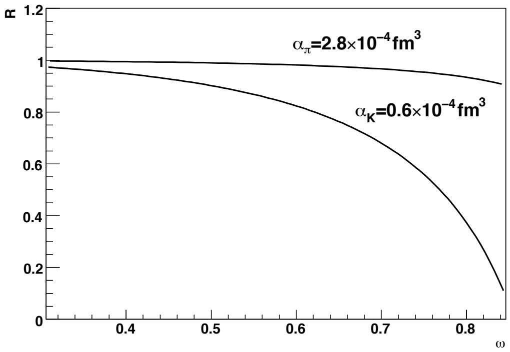

Figure 6.9: $R(\omega)$ for pion ($\alpha_\pi = 2.8 \times 10^{-4}\ fm^3$) and for kaon ($\alpha_K = 0.6 \times 10^{-4}\ fm^3$).

Chapter 7

Conclusion

In the performed work the perspectives of pion poalrizabilities measurement at the COMPASS experiment are analyzed.

- Criteria of Primakoff events selection, taking into account the specifics of the COMPASS setup, are proposed and tested using the data collected during pilot hadron run 2004 with pion and muon beams and lead, copper and carbon targets. It is shown that good setup resolution for such kinematic variables like $E_{\gamma\ cluster} + E_{\pi\ scatt.}$, Q^2, $M_{\pi\gamma}$ and P_t allows effectively choose events with $\pi\gamma$ in the final state. So the COMPASS detector is powerful instrument for Primakoff reaction study.
- The background processes having the same signature as the Primakoff reaction are determined and classified. It's found that some of them can be effectively rejected by simple cuts, others can be suppressed according to special subtraction procedures. It is also shown that such background channels, like beam kaon decay and ρ-meson production, limits the kinematical region which can be used for polarizabilities measurement. Possible contribution of background processes into the systematic uncertainty of polarizabilities measurement was estimated.
- Monte Carlo simulation of Primakoff events in the COMPASS setup was done to estimate the efficiency of applied cuts and study the acceptance of the detector. It was found that the acceptance function for pion and muon events has similar smooth shape in wide ω-range for both muons and pions. It proves the choice of muons as reference for study of systematic effects.

- It is checked that the measured Primakoff cross section for different nuclear targets satisfy Z^2 dependence. The measured value of the Primakoff cross section $\sigma_{Pb} = 0.15 \pm 0.03\ mbn$ is in agreement with the theoretical predictions.

- Estimation of statistical and systematic uncertainties of polarizabilities measurement under assumption $\alpha_\pi + \beta_\pi = 0$ is done basing on 2004 data and extrapolated to the amount of data expected in new data taking. It is shown that four weeks of new data taking at COMPASS allow to measure α_π with a statistical error $0.35 \times 10^{-4} fm^3$. Systematic error may be reduced to $0.2 \times 10^{-4} fm^3$. The Primakoff statistics in the range $0.4 < \omega < 0.925$ may reach 3×10^5 events. Possible total error $0.4 \times 10^{-4} fm^3$ is 4 times better than in the most precise previous measurement (MARK II).

- Basing on the experience of data taking in 2004 a number of changes in the setup configuration is proposed to be done for future data taking. It is shown that 0.3 X_0 Ni target is preferably than 0.5 X_0 Pb target used in 2004. It is proposed to involve only the central part of electromagnetic calorimeter into the Primakoff trigger. The role of an electron converter tested in 2004 is studied and it is recommended to use it permanently during new data taking. Some improvements concerning scattering particles identification are also proposed.

Special attention is paid to the first observation of kaon Primakoff scattering and kaon polarizabilities measurement. It is pointed out that new data taking allows to measure kaon polarizabilities with statistical error $0.25 \times 10^{-4} fm^3$ under assumption $\alpha_K + \beta_K = 0$.

Acknowledgments

First of all I wish to thank the COMPASS collaboration for provided possibility to perform this work and for constructive discussion of each step of it.

I would like to express gratitude to my scientific supervisors Ferruccio Balestra (Turin, INFN) and Alexander Olshevskiy (Dubna, JINR). A. Olshevski gave me his unique experience of pion polarizabilities measurement in SIGMA-AYAKS experiment at Serpukhov. As for F. Balestra, this work could be simply impossible without his efforts.

I am very much obliged to Guido Piragino (Turin, INFN) for his great help in organizational questions.

I'm grateful to M.-L. Colantoni (Turin, INFN), and A.-M Dinkelbach (Munich, TU), who closely collaborate with me on the Primakoff analysis. A long way from the first Primakoff signal to the nice final plots and numbers has been passed together.

I'm grateful to Dubna, Munich and Turin groups deeply involved into the Primakoff business, especially to R. Bertini (Turin, INFN), O. Denisov (Turin, INFN), A. Ferrero (Turin, INFN), J. M. Friedrich (Munich, TU), Z. Kroumshtein (Dubna, JINR), A. Maggiora (Turin, INFN), A. Nagaitsev (Dubna, JINR), T. Nagel (Munich, TU), D. Panzieri (Turin, INFN), S. Paul (Munich, TU), I. Savin (Dubna, JINR), and L. Schmitt (Munich, TU). Their contribution into the present work is inestimable.

My special thanks are to Protvino group, especially to S. Donskov, G. Khaustov and V. Polyakov, who support functioning of the electromagnetic calorimeter - the main detector for Primakoff physics.

I want also to thank V. Alexakhin (DUBNA, JINR), Y. Bedfer (Saclay, CEA), S. Gerassimov (Munich, TU), V. Kolosov (Protvino, IHEP), A. Korzenev (Dubna, JINR) and A. Lednev (Protvino, IHEP), who have spent a lot of time improving the quality of the Monte Carlo simulation and event reconstruction.

I'm grateful to A. Arbuzov (Dubna, JINR), D. Bardin (Dubna, JINR) and M. Moinester (Tel-Aviv university) for the quality theoretical support of this work.

I want to thank all people involved in preparation of new data taking within the Primakoff program. I wish to mention inestimable contribution done by M. Alexeev (Turin, INFN), V. Anosov (JINR, Dubna), A. Austrigesilo (CERN), J. Bernhard (Mainz univ.), M. Chiosso (Turin, INFN), O. Denisov (Turin, INFN), J. M. Friedrich (Munich, TU), R. Geyer (Munich, LMU), P. Jasinski (Mainz univ.), B. Ketzer (Munich, TU), I. Konorov (Munich, TU), M. Krämer (Munich, TU) ,Z. Kroumshtein (Dubna, JINR), A. Magnon (Saclay, CEA), G. Mallot (CERN), T. Nagel (Munich, TU), D. Neyret (Saclay, CEA), R. Panknin (Bonn univ.) and A. Zvyagin (Munich, LMU).

I'm thankful to all members of COMPASS publications committee and especially to E.-M. Kabuss for careful reading and editing of my papers, proceedings and conference talks.

I'm also grateful to G. Chelkov (Dubna, JINR), F. Dydak (CERN), S. Dubnička (Bratislava, Inst. of Physics), G. Fäldt (Uppsala univ.), A. Kotzinian (Turin, INFN), V. Pervushin (Dubna, JINR) and L. Tkachov (Dubna, JINR) who has shown a sincere interest to my work.

Bibliography

[1] A. Klein, Phys. Rev., **99**, 998 (1955)

[2] A. M. Baldin, Nucl. Phys., **18**, 310 (1960)

[3] V. A. Petrun'kin, JETP, **13**, 804 (1961)

[4] V. A. Petrun'kin, PEPAN, **12** 3 (1981) (in Russian)

[5] J. Gasser, Chiral perturbation theory at COMPASS, International Workshop on Hadron Structure and Spectroscopy, Turin (2008)

[6] J. Portoles, M. R. Pennington, *The second Da*Φ*ne* Physics Handbook v.2, 579 (1999), hep-ph/9407295

[7] C. A. Wilmot, R. H. Lemmer, Phy. Rev., **C65**, 035206 (2002)

[8] M.A. Moinester and V. Steiner, Preprint TAUP-2469-97 (Workshop on Chiral Dynamics: Theory and Experiment) (1998)

[9] A.M. Bernstein, D. Drechsel, and T. Walcher (eds.), Lecture notes in physics (Vol. 513), Springer (1998)

[10] U. Bürgi, Phys. Lett., **B377**, 147 (1996)

[11] J. Gasser, M. A. Ivanov, M.E.Sainio, NP, **B745**, 84 (2006)

[12] M. V. Terent'ev, Sov. J. Nucl. Phys., **16**, 87 (1973)

[13] J. F. Donoghue and B. R. Holstein, Phys. Rev., **D40**, 2378(1989)

[14] B. R. Holstein, Comm. Nucl. Part. Phys., **19**, 221 (1990)

[15] Yu. M. Bystritskiy, A.V. Guskov, V.N. Pervushin, M.K. Volkov, Phys. Rev. **D80**, 114001 (2009)

[16] M. K. Volkov, Sov. J. Part. and Nuclei, **17**, 186 (1986)

[17] M. K. Volkov, A. A. Osipov, Sov. J. of Nucl. Phys., **41**, 650 (1985)

[18] H. A. Abarbanel and M. L. Goldberger, Phys. Rev., **165**, 1594 (1968)

[19] L. V. Fil'kov, V. L. Kashevarov, Phys.Rev., **C73**, 035210 (2006)

[20] L. V. Fil'kov, V. L. Kashevarov, Phys. Rev., **C72**, 035211 (2005)

[21] M. V. Terent'ev, Sov. J. Nucl. Phys., **16**, 87 (1973)

[22] J. F. Donoghue, B. R. Holstein, Phys. Rev., **D40**, 1378 (1989)

[23] M. J. Lavelle, N. F. Nasrallah, K. Schilcher, Phys. Lett., **B355**, 211 (1994)

[24] T. Das, V. Mathur, S. Okubo, Phys. Rev. Lett., **19**, 859 (1967)

[25] S. R. Amendolia et al., Nucl. Phys. **B277**, 128 (1986)

[26] M. A. Ivanov, T. Mizutani, Phys. Rev., **D45**, 1580 (1992)

[27] G. V. Efimov, M. A. Ivanov, The quark confinement model of hadrons., Inst. of Phys. Pub., Bristol (1993)

[28] V. N. Pervushin, M. K. Volkov, Phys Lett., **B55**, 406 (1975)

[29] A. E. Radzhabov and M. K. Volkov, Phys. Part. Nucl. Lett., **2**, 1 (2005) [Pisma Fiz. Elem. Chast. Atom. Yadra, **2**, 7 (2005)] [arXiv:hep-ph/0403131]

[30] T. Walcher, Physik J5, **N12** ,45, 2006.

[31] T. A. Aibergenov et al., Cezch J. Phys., **B36**, 948 (1986)

[32] C. Berger et al., Z. Phys. **C26**, 199 (1984)

[33] A. Courau et al., Nucl. Phys., **B271**, 1 (1986)

[34] Z. Ajaltoni et al.,*VII Int. workshop on photon-photon collision* Paris (1986)

[35] J. Boyer et al., Phys. Rev., **D42**, 1350 (1990)

[36] D. Babusci et al., Phys Lett., **B277**,158 (1992)

[37] Yu. M. Antipov et al., JETP Lett., **35**, 7 (1982)

[38] Yu. M. Antipov et al., Phys. Lett., **B121**, 445 (1983)

[39] Yu. M. Antipov et al., Z. Phys., **C26**, 495 (1985)

[40] J. Ahrens et al., Eur. Phys. J., **A23**, 113 (2005)

[41] A. E. Kaloshin and V. V. Serebryakov, Z. Phys., **C64**, 689 (1994)

[42] M. Buenerd, Nucl. Phys., **A361**, 111 (1995)

[43] N. Kaiser, J Friedrich, Eur. Phys. J., **A36**, 181-188 (2008)

[44] R. Baldini, S. Bellucci, Lecture Notes in Physics, 452 (1995)

[45] L. V. Fil'kov, V. L. Kashevarov, arXiv:hep-ph/0610102v2

[46] A. S. Galperin, G. Mitselmakher, A. G. Olszewski and V. N. Pervushin, Yad. Fiz. , **32**, 1053 (1980)

[47] Yu. M. Antipov et al., Phys. Lett., **121B**, 445 (1983)

[48] Antipov Yu. M. et al., Investigation of Compton-effect on π-meson and carged pion polarizability., JINR preprint P1-86-710 (in Russian)

[49] A. Olshevskiy, Измерение электрической и магнитной поляризуемости заряженного пиона в реакции радиационного рассеяния на ядрах при малых передачах (PhD thesis) JINR, 1986

[50] L. D. Landau and I. J. Pomeranchuk, Dokl. Akad. Nauk. SSSR 92, 535 (1953); 92, 735 (1953)

[51] S. Klein, Rev. Mod. Phys., **71**, 1501 (1999)

[52] A. B. Arbuzov, JHEP, **0801**, 031 (2008) arXiv:0710.3639 [hep-ph]

[53] A. A. Akhundov et al., Z. Phys. **C66** (1995)

[54] A. A. Akhundov et al., About the electromagnetic corrections to the polarizabilities of a charged pion., JINR preprint P1-84-815 (in Russian)

[55] A. A. Akhundov et al., Electromagnetic corrections to Compton effect on π-meson., JINR preprint P1-86-710 (in Russian)

[56] N. Kaiser and J. M. Friedrich, Eur. Phys. J. A, **39**, 71 (2009) [arXiv:0811.1434 [hep-ph]]

[57] F. Bradamante, S. Paul et al., CERN Proposal COMPASS, http://wwwcompass.cern.ch , CERN/SPSLC 96-14, SPSC/P297, CERN/SPSLC 96-30, SPSC/P297, Addendum 1

[58] M. Faessler, Nucl. Phys., **A655**, 1-2, 121-126 (1999)

[59] P. Abbon , E. Albrecht et al., NIM, **A577**, 455-518 (2007)

[60] M. A. Moinester et al., Czech. J. Phys. 53, B169-B187 (2003) hep-ex/0301024

[61] M. A. Moinester, Pion polarizabilities and Hybrid meson structure at COMPASS, Tel Aviv University Preprint TAUP 2661-2000, hep-ex/0012063

[62] A. Olchevski, M. Faessler, Experimental requirements for COMPASS Initial Primakoff Physics program, COMPASS coll. Meeting (2001)

[63] M. J. French et al., Nucl. Instr. and Meth., **A466**, 359 (2001)

[64] H. Angerer et al., Nucl. Instr. and Meth., **A512**, 229 (2003)

[65] V. Palmieri et al., Nucl. Instr. and Meth., **A413**, 475 (1998)

[66] D. Alde et al., Nucl. Phys., **B269**, 485 (1986)

[67] F. Binon et al., Nucl. Instr. and Meth., **A248**, 86 (1986)

[68] M. Kobayashi, et al., Nucl. Instr. and Meth., **A345**, 210 (1994)

[69] F. Binon et al., Nucl. Instr. and Meth., **A214**, 269 (1983)

[70] F. Binon et al., CERN preprint CERN-EP/81-27 (1981)

[71] C. Bovet et al., The CEDAR counters for particle identification in the SPS secondary beams, CERN Yellow Report, CERN 82-13 (1982)

[72] R. Frühwirth, Nucl. Instr. and Meth., **A262**, 444 (1987)

[73] E. J. Wolin et al., Nucl. Instr. and Meth., **A329**, 493 (1993)

[74] V. Blobel et al., A new method for the high-precision alignment of track detectors, in: Proc. PHYSTAT2002, 2002, hep-ex/0208021

[75] A. A. Lednev, Nucl. Instr. and Meth., **A366**, 292, (1995)

[76] GEANT - detector description and simulation tool, CERN Program Library Long Writeup W5013, http://wwwasdoc.web.cern.ch/wwwasdoc /geant html3/geantall.html

[77] G. Ingelman et al., Comput. Phys. Commun, **101**, 108 (1997)

[78] T. Sjöstrand et al., Comput. Phys. Commun, **135**, 238 (2001)

[79] R. Brun et al., Nucl. Instr. and Meth., **A389**, 87 (1997) http://root.cern.ch

[80] http://ges.home.cern.ch/ges/phast/index.html

[81] A. Guskov [COMPASS Collaboration], Fizika, **B17**, 313 (2008)

[82] A. Guskov, J. Phys. Conf. Ser. **110**, 022016 (2008)

[83] A. Guskov [COMPASS Collaboration] *In *Moscow 2006, ICHEP* 655-658*

[84] M. L. Colantoni, Proceedings of MENU 2007 11th International Conference on Meson-Nucleon Physics and the Structure of the Nucleon (2007)

[85] R. Kuhn, Simulations for the measurement of the polarizabilities of the pion at COMPASS, Munich, TU (master thesis), 2009

[86] M.-L. Colantoni, Czech. J. Phys. **55** (2005)

[87] M. Buenérd, NIM, **A361**, 111 (1995)

[88] A. Guskov [COMPASS Collaboration], accepted for publication in Nucl. Phys. B. (2009)

[89] A. Guskov, Phys. Part. Nucl. Lett., **3** 59 (2010)

[90] P. K. Jasinski [COMPASS Collaboration], Spin-Praha 2009

[91] F. Guerrero, J. Prades, Phys. Lett. **B405**, 341 (1997)

[92] M. A. Moinester and V. Steiner, arXiv:hep-ex/9801011